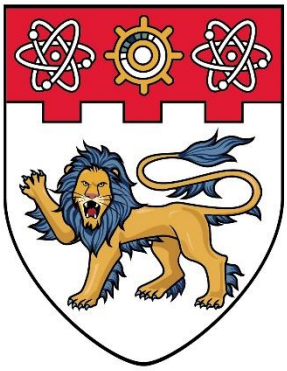

NANYANG TECHNOLOGICAL UNIVERSITY
SINGAPORE

DESIGN OF NOVEL F-ATP SYNTHASE INHIBITORS OF *MYCOBACTERIUM TUBERCULOSIS*

ADAM HOTRA
Interdisciplinary Graduate School
Healthy Society

2018

DESIGN OF NOVEL F-ATP SYNTHASE INHIBITORS OF *MYCOBACTERIUM TUBERCULOSIS*

ADAM HOTRA

Interdisciplinary Graduate School
Healthy Society

A thesis submitted to the Nanyang Technological University in partial fulfilment of the requirement for the degree of
Doctor of Philosophy

2018

Acknowledgements

I would like to express my sincerest gratitude to my supervisor Associate Professor Roderick W. Bates, my co-supervisor Professor Gerhard Grüber as well as my former supervisor Hajime Hirao for their endless guidance and support throughout my PhD program.

I am thankful to all the lab members and collaborators, namely Dr. Priya Ragunathan and Dr. Goran Biuković for their help in preparation of the membrane vesicles and guidance in biochemistry experiments, Dr. Amaravadhi Harikishore for his guidance on pharmacophore modelling and screening, Dr. Nitin Kalia for his help and support with respiratory chain experiments.

I am also immensely grateful to Dr. Subhashri Kundu and Mr. Jickky Palmae Sarathy for teaching me basic microbiology and their support during the microbiology experiments. I would also like to express my sincere gratitude to Dr. Viktor Barát and Mr. Dániel Csókás for their help with chemistry. I would also like to thank the other lab members who have helped me and created a stimulating environment.

I would like to thank my family and all my friends who provided me great support through difficulties of my PhD journey: Svetlana, Meshal, Viktor, Ali, Militsa, Simin, Blaz, Yorick, Ania and Chui Fann. I would like to especially thank my team American Dragons Singapore for making my stay in Singapore unforgettable.

I would like to acknowledge the financial support from the Interdisciplinary Graduate School, School of Physical and Mathematical Sciences, School of Biological Sciences, and Nanyang Technological University.

Table of content

List of figures

List of tables

Abbreviations

Ac	acetyl
ACMA	9-amino-6-chloro-2-methoxyacridine
ADP	adenosine diphosphate
anh	anhydrous
aq	aqueous
ATP	adenosine triphosphate
BCG	bacillus Calmette-Guérin
BDQ	bedaquiline
d	doublet
DCCD	dicyclohexylcarbodiimide
DCM	dichloromethane
DMAP	4-(dimethylamino)pyridine
DMF	dimethylformamide
DMSO	dimethyl sulfoxide
EDTA	ethylenediaminetetraacetic acid
EMB	ethambutol
Et	ethyl
h	hour(s)
HIV	Human Immunodeficiency Virus
IC_{50}	half maximal inhibitory concentration
INH	isoniazid
iPr	isopropyl
IR	infra-red spectroscopy
J	coupling constant
LTBI	Latent tuberculosis infection
m	multiplet
MALDI-TOF	matrix-assisted laser desorption/ionization time of flight
MDR	multidrug-resistant
Me	methyl
MIC_{50}	minimum inhibitory concentration inhibiting 50% of the bacterial growth
MS	mass spectrometry

Mtb	*Mycobacterium tuberculosis*
NADH	nicotinamide adenine dinucleotide
NBD-Cl	chloro-7-nitrobenzofurazan
NMR	nuclear magnetic resonance spectroscopy
NOESY	Nuclear Overhauser effect spectroscopy (NMR)
PAS	para-aminosalicylic acid
POA	pyrazinoic acid
PZA	pyrazinamide
q	quartet
ROS	reactive oxygen species
rt	room temperature
s	singlet
SAR	structure–activity relationship
SM	starting material
STS	skin tuberculin test
t	triplet
TB	tuberculosis
TFA	trifluoroacetic acid
VdW	van der Waals
WHO	World Health Organization
XDR	extensively drug-resistant

Abstract

Abstract

F_1F_O ATP synthase of *Mycobacterium tuberculosis* is an attractive and intensively-studied drug target. Adenosine triphosphate (ATP) is necessary for cell growth and is vital for cell survival, especially in the case of dormant *Mycobacterium*. In 2012, an inhibitor of F_1F_O ATP synthase, Bedaquiline (BDQ) was approved for the treatment of tuberculosis (TB). Despite promising efficacy, BDQ was found to have several adverse effects and therefore is used solely for the treatment of multiple drug-resistant tuberculosis (MDR-TB). This suggests the need for a more viable drug targeting the respiratory chain.

A new drug target in F_1F_O ATP synthase was proposed; a 13 amino acid-long loop γ165–178 at the interface of the *c*-ring and subunit γ. This loop is unique to *Mycobacterium* and enables specific compound binding without affecting the human F_1F_O ATP synthase.

To date, no high-definition structure of the *Mycobacterium* F_1F_O ATP synthase is present in literature, and hence to study it, a homology model was built. With this model, 1.5 million compounds were docked using Maestro suite (Schrödinger). The 81 best scoring compounds were tested for growth inhibition and one compound (compound 6) inhibited non-pathogenic *M. smegmatis* with an IC_{50} 11 μM and *M. bovis* BCG with an IC_{50} of 40 μM. Furthermore, compound 6 blocked ATP synthesis and hydrolysis in the inverted membrane vesicles assay. Hence, it was confirmed that compound 6 binds to the F_1F_O ATP synthase as predicted. Additionally, the hydrolysis rate, and amount of ATP synthetized between wild-type vesicles and $\Delta\gamma_{166\text{-}179}$ mutant vesicles was compared. Vesicles with the deletion of the $\gamma_{166\text{-}179}$ loop increased the ATP hydrolysis rate. Interestingly ATP synthesis dropped by 50%. These results suggest that $\gamma_{166\text{-}179}$ loop plays an important role in the coupling between the *c*-ring and the central stalk.

Moving forward, compound 6 and a series of analogs were synthesized for lead optimization based on the model of the docked compound to the F_1F_O ATP synthase.

Introduction

1. Introduction

Although Tuberculosis (TB), caused by *Mycobacterium tuberculosis (Mtb),* is a treatable and curable disease, it still presents a very serious threat to human health. To date, TB has killed more people than any other pathogens. Despite an increased usage of anti-TB drugs, a TB infection still claims the life of a human every 10 seconds. In 2016, 10.4 million people contracted TB, and 1.7 million of them died from this disease. Although the incidence of TB is slowly declining, it is still present especially in the developing countries (Figure 1-1) [1]. Why is it so difficult to control TB? Firstly, the biggest problem in current TB treatment strategies is the presence of evolving drug resistance. Drugs used in common practice are over 40 years old, slow-acting and usually require long-term therapy. Patients often are in low compliance to such treatments, thereby resulting in incomplete treatment regimes. As a result of low compliance, strains of *Mtb* are increasingly resistant to at least one of the first-line antibiotics and are becoming more resistant to two or more drugs [1]. Secondly, standard treatment lasts from six to nine months, and consists of several bulky pills administered every day. Most TB cases can be cured when medicines are provided and administered adequately. However, patients usually feel better after a few weeks which results in the tendency to quit therapy without the eliminating of *Mtb* infection. To counter this, WHO currently utilizes the Directly Observed Treatment, in which a trained health worker would personally supervise treatments [2]. This is, however, labor-intensive and expensive. As such, alternatives should be addressed to facilitate the complete elimination of TB infection. Thirdly, an HIV-positive individual is 20 times more likely to develop tuberculosis than an uninfected individual. In addition, the retroviral drugs commonly used in AIDS/HIV treatment are usually not compatible with current TB treatment, particularly due to the CYP3A induction by rifampin [3]. Therefore, there is a strong need for the novel drugs in TB treatment that act against resistant strains, with a shorter treatment time and minimal side effects.

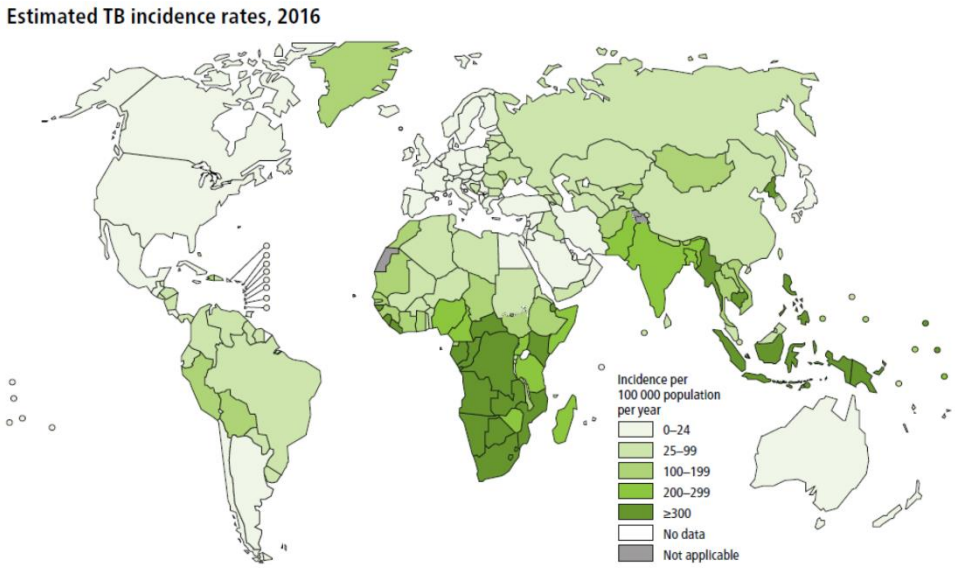

Figure 1-1: Estimated TB incidence rates in 2016. South-East Asia is emerging as an region of high importance with the incidence 45% of the global TB [1].

1.1 Pathophysiology of TB

The causative agent of TB is *Mtb*. Other pathological strains causing TB include *M. bovis, M. africanum, M. microti and M. canetti [4]*. Although more than 20 species are pathogenic, the most important pathogen is *Mtb*. Mycobacteria are slow-growing, aerobic-to-microaerophilic, rod-shaped bacilli which typically measure 0.5 μm by 3 μm. Mycobacteria possess a unique cell wall structure, that is rich in fatty- and mycolic acids, crosslinked to the peptidoglycan-bound arabinogalactan. This structure provides an extraordinary lipid barrier, that enhances the physiological advantage to mycobacteria by raising its protection against antibiotics and the host immune response, which is thereby crucial for their survival. Due to its high mycolic acid content, mycobacteria can be identified by a distinctive acid-fast staining. The cell wall can be stained with arylmethane dyes, most commonly Ziehl–Neelsen stain, which is not de-stained in the presence of acidic alcohol or weak acids. However, the Ziehl-Neelsen stain is not exclusive to only mycobacteria, but are also usable to other weakly acid-fast staining bacteria such as *Nocardia* spp [5].

Infection is initiated when inhaled bacilli are phagocytosed by various host immune cells, such as the dendritic cells and alveolar macrophages. Here, *Mtb* is able to arrest the maturation of the phagosome in the stage of early endosome by interfering with the host cell signalling system [6]. In addition, *Mtb* also exudes a defence mechanism which protects itself, should the

maturation of the phagosome still occur. This is an active pathogen-mediated defence wherein *Mtb* inhibits the fusion of the matured phagosome to the lysosome [7]. This defence mechanism inhibits the acidification of the phagosome and also protects *Mtb* against reactive oxygen species (ROS) [8].

Recent studies also suggest the translocation of mycobacteria to the cytosol, which is observed only with pathogenic mycobacteria [9]. This translocation is mediated by the secretion of the cell filtrate protein 10 (CFP-10) and the early secretory target *Mtb* (ESAT-6) [10] which in turns, also enhances the virulence of *Mtb*. Although *Mycobacteria* survive inside macrophages, alveolar macrophage and pneumocytes produce chemokines and cytokines, mainly tumor necrosis factor alpha (TNF) and interleukin 12 (IL-12) [11, 12]. These immunogenic factors attract inflammatory cells, i.e., neutrophils, monocyte derived macrophages, natural killer cells, fibroblasts, and γδ-T cells. Subsequently, the infected tissue quickly transforms into a granuloma which represents the pathological hallmark of TB. A granuloma is a chronic inflammatory lesion, infiltrated by mononuclear cells. These tuberculous nodules, or tubercles, gave the disease its name. The remodelling is initiated by both bacterial and host factors. On one hand, granuloma delimits the growth and spread of bacteria, and thus controls the infection. On the other hand, it creates a protected niche, where *Mtb* can persist under dormant condition and eventually could disseminate. Therefore, in the healthy individual, it is decided at the level of a granuloma whether the immune system response would contain the infection or it would progress from latent TB into active TB.

A typical granuloma found in TB is a caseous, recognised by its cheese-like appearance. The size of caseous granuloma can vary from 1 mm to >2 cm. Granulomas undergo necrosis in the centre, and hence, contain dead cells and cell debris. One of the first innate immune cells recruited to the infection side are the macrophages, which later differentiate into specialized cell types, including multinucleated giant cells and epithelioid macrophages. On the periphery of the granuloma, the subset of the macrophages transforms into epithelioid cells (histiocytes) with tight cellular junctions between the neighbouring cells. Alongside, T-cells and B-cells creates a lymphohistiocytic cuff which contains the infection within granuloma. At the latter stage, the

fibroblasts start producing a fibrous capsule on the outer layer of macrophages, excluding the lymphocytes from the centre of the granuloma [13]. This type of granuloma is largely associated with latent TB infection, where the strong host immune system response contains the infected macrophages inside the fibrous cuff. If the infection cannot be controlled, often influenced by factors such as HIV coinfection, malnutrition and immunosuppressive drugs therapy, the caseum might accumulate and necrosis will increase. This provides favourable conditions for readily proliferating bacteria [14]. Liquefied caseum might rupture into the airways of the host pulmonary lungs and cause dissemination of TB. Although this process is not fully understood, liquefaction was thought to be one of the main mechanism for the transmission of TB and is also responsible for the progression from latent TB into active TB [15].

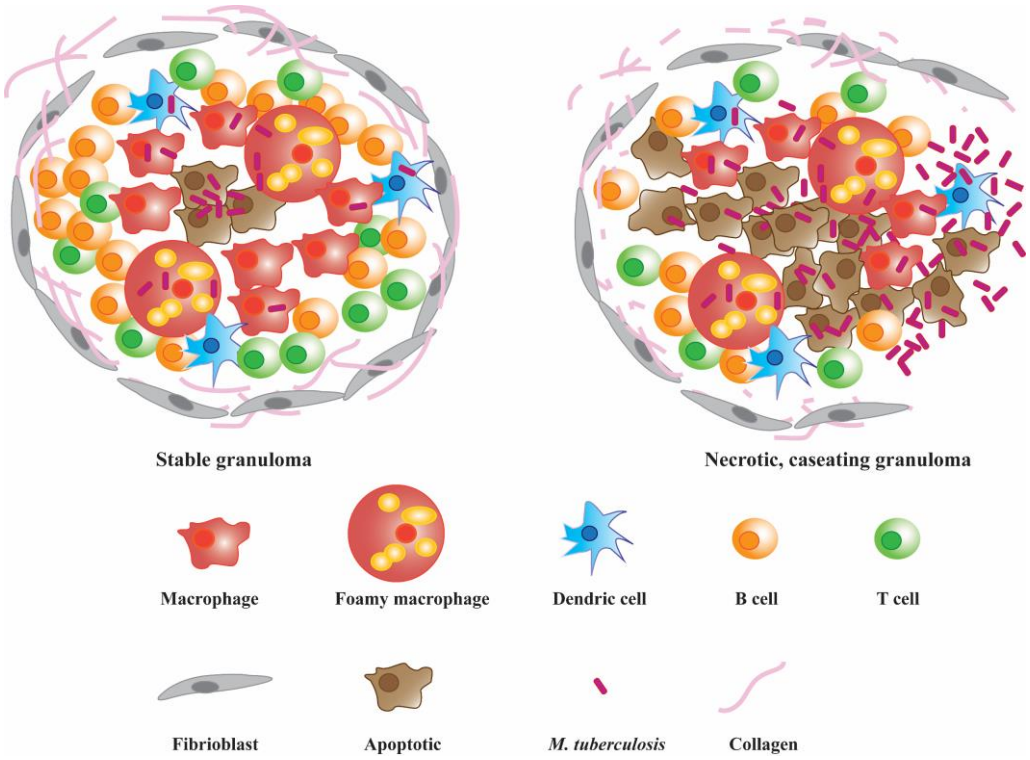

Figure 1-2: Stable granuloma and necrotic granuloma. Caseous centre containing apoptotic cells and cell debris is surrounded by infected and foamy macrophages, followed by T cells and B cells (left). Fibrioblast and collagen on the outer layer create a fibrous cuff. Stable granuloma might undergoing liguefaction resulting in to dissemination of the *Mtb* into the neighbouring tissue (right). Adapted from [16, 17].

A granuloma was originally thought to be a well-defined static structure, but recently it was observed, that it is a highly dynamic structure, with immune cells migrating in and out.

In most cases, active TB is not caused by primary *Mtb* infection, but by the reactivation of the already present infection. This occurres in 3%–10% of immunocompetent individuals [18]. Tuberculosis is manifested not only by its pulmonary lesions, but also by its systematic symptom, such as anorexia and wasting [19]. Interestingly, this is the origin of the old TB name "consumption". This seems to be caused mainly by host factors including proinflammatory TNF [20].

1.1.1 Latent tuberculosis infection

As discussed above, the primary infection by *Mtb*, depending on the host immune system response, can be either contained and lead to latency, or might develop into the active disease. Latent TB infection (LTBI) is not contagious and does not demonstrate any clinical nor physical symptoms. LTBI is defined by the presence of an antigen-specific T cell response in the absence of clinical symptoms, therefore it is usually diagnosed by a standard intradermal tuberculin test which utilizes blood interferon gamma release assays (IGRAs) that detects the immunological response of the host to *Mtb*.

Apart from IGRAs, another test to detect TB infection is the tuberculin skin test (TST). Tuberculin, an extract from the dead culture of *Mtb* (therefore also called purified protein derivative or PPD), is injected into the patient's skin. If the person was exposed to *Mtb*, tuberculin would trigger the immune response which is manifested by redness and swelling at the injection site [21]. Tuberculin test was used by two methods, the so-called Mantoux test [22] and Heaf test [23]. Although the Heaf test had several advantages over the Mantoux test, the Heaf test was discontinued and hence the Mantoux test became the standard. The main disadvantage of the tuberculin test is is the presence of a high rate of false positives, mostly caused by a prior BCG vaccination and exposure to non-tuberculous mycobacteria [24]. The interferon gamma assay is based on the strong Th_1 immune system response triggered by *Mtb* infection. This ELISA based test quantifies the amount of IFN-γ produced *in vitro* when blood sample is exposed to *Mtb* antigens. Although IGRA is not affected by previous BCG vaccination, IGRA cannot differentiate between the latent and active TB. Furthermore, it was reported that one quarter of TB patients have negative IGRA

test results [25]. Although new and more reliable tests are being developed, these TST and IGRA remain as a gold standard for diagnosis.

LTBI is treated only in the specific groups of people, such as immunocompromised patient *e.g.* patients with HIV or patients receiving immunosuppressive drugs, or high-risk groups *e.g.* prisoners, homeless, drug addicts, healthcare workers in contact with TB. Treatment recommendation also depends on the region and country, because in the high TB burden and resource limited countries the treatment of active TB is of a higher priority than LTBI treatment [26]. In addition, treatment of the multi drug resistant (MDR-TB) LTBI seems to be a good tool to control MDR-LTBI outbreaks, as the treatment is well tolerated and feasible in resource limited settings [27].

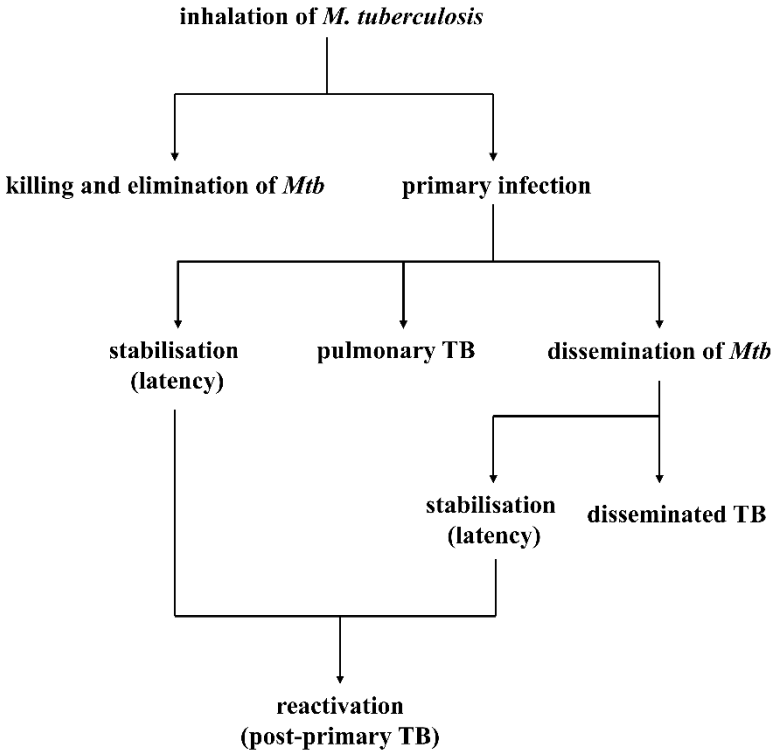

Figure 1-3: Possible development after inhalation of the *Mtb*. After inhalation, *Mtb* can be immediately killed in which case no infection occurs. Otherwise, the primary infection follows, which can be either contained by the immune system leading to latency or proceed to active TB. Dissemination of *Mtb* can lead to a disseminated TB of to the latent infection. The latter can be reactivated under various condition *e.g.* compromised immunity and develop into active TB [28].

1.1.2 Pulmonary TB

In healthy individuals, 5-10% of the infections by *Mtb* lead to active pulmonary TB [29]. Typical physical symptoms of pulmonary TB include cough, sputum production, weight loss, fever and night sweats, which together with

chest x-rays are good indications of TB infection [30]. As the majority of the TB cases are observed in low to middle income countries, the most frequently used method for diagnosis is the identification of the acid-fast bacteria in the sputum using the light microscopy [31]. Although this is an inexpensive method, it is labour extensive and requires skilled and trained professionals. It has reasonable sensitivity but the selectivity is highly variable [32, 33]. In high-income countries, fluorescence microscopy is used for its higher sensitivity, however specificity remains similar to the light microscopy [34]. Another standard for pulmonary TB diagnosis is the radiometric or fluorescence liquid culture, BACTEC [35]. Recently, the new diagnostic assay - GeneXpert MTB/RIF has been introduced and received endorsement from WHO. This molecular-based assay process sputum by real-time PCR and simultaneously detect *Mtb* and rifampicin resistance [36]. Although GeneXpert MTB/RIF is relatively costly, it offers advantages such as high sensitivity and specificity, low requirements for personnel training and biosafety facilities and thus can be used at the point of treatment [37].

Although *Mtb* can cause primary disease, most notably in neonates, the most common manifestation of TB in adults is the reactivation of a pre-existing, chronic infection.

1.1.3 Extrapulmonary and disseminated tuberculosis

The incidence of disseminated and extrapulmonary tuberculosis is rising. Almost every fifth to fourth tuberculosis counts for extrapulmonary case (Figure 1-4A), where infection spread from lungs to other organs, occurs most frequently in lymph nodes, hematogenous tissue and in the osteoarticular system [38]. The symptoms of extrapulmonary TB are broad and vague, resulting in difficult diagnosis. Serious symptoms onset occurs usually late in the acute phase of the infection. Diagnosis has to be made via advanced imagining or biochemical tools [39]. Furthermore, extrapulmonary TB is more prevalent in patients co-infected with HIV [40]. Most common types of extrapulmonary TB are tuberculous lymphadenitis, pleural TB, central nervous system TB, tuberculous peritonitis, tuberculous pericarditis and skeletal TB (Figure 1-4B).

Miliary TB is a deadly form of TB, occurring when TB infection has disseminated from the ruptured local focus into the lymphatic system and

hematogenous tissue, thereby infecting various host organs such as the lungs, liver and spleen. The resulting patter on RTG resembles pearl mille from which this type of TB got its name. Miliary TB was predominantly found to infect infants and children, however the implementation of the BCG vaccine lead to protection in infants and children. As such, recent years of diagnosed military TB was found in adults instead. This could largely be attributed to the rise in HIV infection since 1980, wherein HIV positive patients are more prone to TB co-infections [41, 42]. Severe physical symptoms of untreated military TB include septic shock and acute respiratory distress syndrome.

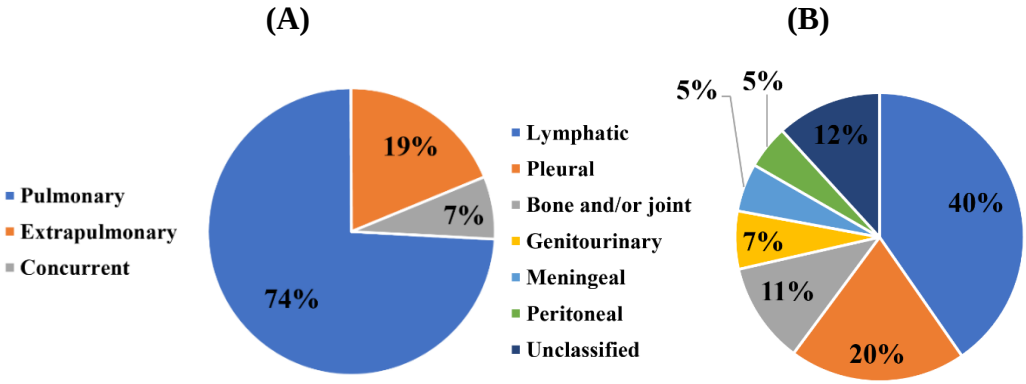

Figure 1-4: Epidemiology of TB. incidence of pulmonary (74%), extrapulmonary (19%) and concurrent (7%) (*e.g.* miliar) TB (A) Extrapulnonary TB types cases were lymphatic (40%), pleural (10%), bone and/or joint (11%), genitourinary (7%), meningeal (5%), peritoneal (5%), and unclassified (11.8%) (United States, 1993–2006) [43].

1.1.4 Infection by nontuberculous mycobacteria

The nontuberculous mycobacteria (NTM) represent a diverse group of mycobacterial species. Most infections involve *Mycobacterium avium* complex or (MAC): *M. avium*, *M. intracellulare*, and *M. chimaera*. Other NMT strains include *e.g. M. kansasii. M. chelonae*, and rapidly growing mycobacteria *M. abscessus*, *M. fortuitum*. The source of the majority of NTM infection comes from the water or soil environments. [44]. Water from home in Europe and America contain NTM in 10-95% of the samples, with even higher rates for hospitals [45, 46]. In recent years, the incidence of increasing prevalence of NTM disease is on the rise [47]. Particularly, nosocomial outbreaks are frequently caused by NTM. Hospital waters have been found to lead to NTM nosocomial outbreaks and this is due to the nature of NTM bacteria whereby they are resilient and able to thrive in distilled water, high temperatures as well

as commonly used disinfectants [48]. As NTM are opportunistic infections, they are mainly affecting patients with lung damage or are immunocompromised such as HIV, AIDS and elderlies. Interestingly, it was found that females are more prone to NTM infection as well. [49]. Patients with NTM can be wrongly diagnosed with TB and as such they may have received wrong or unnecessary treatment [50]. Until recently, infections from animal-to-human and human-to-human have not been observed. However, in the population of the patients diagnosed with cystic fibrosis and co-infected with *M. abscessus*, the whole-genome sequencing of the clinical isolated showed that most of the infections occurred thought human to human transmission [51].

Not every infection of NTM needs treatment, and often it can remit spontaneously. Many factors including age, comorbidity and strain of NTM have to be taken into the account prior to treatment. Treatment for pulmonary NTM disease is lengthy, lasting 12-24 months, and complex, which it requires a combination of antibiotics. Recommendations and guidelines differ on the treatment regimens but usually consist of the combination of two to four drugs including clarithromycin, azithromycin, ethambutol, isoniazid, rifampicin. Infection by fast growing mycobacteria might be treated by amikacin, cefoxitin or imipenem. In some cases, a surgical resection is an alternative to a curative treatment [52].

1.2 Challenges in TB treatment

Developing new anti-TB drugs, as well the antibiotics in general, is not considered as profitable by the pharmaceutical industry. Thus, the need for the TB drugs has not been addressed to the extent that it deserves, well-illustrated by the almost 50-year gap between the introduction of the rifampicin in 1966 and the recent approved bedaquiline (BDQ), the next new anti-TB drug. However, the lack of new drugs is not the only challenge of the TB treatment. As active TB patients typically infect approximately 10 to 15 contacts per year, many problems such as patients' adherence, are matters of public health and can be solved by implementation of the new policies, standards and guidelines.

1.2.1 Patient adherence

The high frequency and dosage, long duration of TB regime alongside frequency of adverse effects makes patients' adherence to the treatment

challenging. For instance, the presence of red urine and side effects may be interpreted by patients to be unhealthy, thus leading to abstinence in some patients [53].

Generally, the most frequent reason to discontinue TB treatment is due to the patients lack of knowledge in the amelioration of TB symptoms after initial treatment [54]. Despite so, this loss of adherence to drug regimens could be avoided by educating patients about the onset, progress and elimination of TB as well as the impact of premature ending of regime on their health [55].

Furthermore, medical consultation, X-ray, TST as well as long-term treatments may not be affordable to patients in certain countries. This could be largely due to the social and cultural aspects in TB diagnosis and treatment where some patients may feel stigmatised from having contracted TB and are ashamed to visit health centres or proceed with treatments. In addition, alcohol and drug abuse also contribute to the low adherence wherein patients do not take their medication just to avoid health centres. Illiterate, divorced/widowed, lack of health insurance and/or migrants are also more likely to be non-adherent to TB regimens. In addition, some patients may not be able to afford the related cost of medical consultation, X-ray and smear tests. Furthermore, social and cultural pressure might influence the adherence of treatments by patients, both in the positive or negative way. In some countries TB patients may be stigmatised and feel ashamed visit to health centres or to buy medicine.

On the other hand, family support or child dependence on patients usually create positive pressure to adhere to TB regimens [56]. Also, emotional support from spouse can create such positive environment where patients are more likely to comply to TB regimens. Nonetheless, such emotional support may influence the dynamics of families or the marriage itself, where it may lead to more negativity than positivity [53].

To tackle these challenges, directly observed therapy (DOTS) was introduced by WHO. Through DOTS, patient receives and takes the medicine while being observed by healthcare worker or appointed person [57]. Except improving the patients' adherence, DOTS also aims to standardise treatment, recording and detection of TB [58]. DOTS was thought to solve most of the clinical treatment problems, however, to no avail.

DOTS may have improved the patients' adherence to TB regimens, however, it has several constraints. In terms of manpower, the highly skilled and motivated healthcare workers needed are often not available in low income countries particularly, TB endemic countries. Hospitals that practice DOTS may be too far to reach or too costly for even for economically active patients. Some patients also experience the lack of means to reach such hospitals [59]. Some meta-analysis studies performed in low, medium or high income countries also found no significant improvement in the implementation of DOTS [60].

1.2.2 HIV co-infection

TB co-infection of HIV positive patients are also a threat to the elimination of the TB endemic. In some countries, it was observed that despite having similar TB infection rates in HIV positive or negative patients, a TB co-infection with HIV patients tend to develop into aggressive active TB disease [61]. In such cases, the synergy of TB with HIV puts such patients with LTBI at a much greater risk of progressing to active TB. Statistics have also shown that patients co-infected with XDR-TB and HIV had a median survival rate of only 16 days from the point of diagnosis.

1.2.3 Drug resistance

The discovery of streptomycin was thought to end TB. Selman Waksman, the Nobel Prize laureate in 1952 for the discovery of streptomycin, claimed that "the complete eradication of this disease is in sight." [62]. Regrettably, shortly after its discovery in 1943, he was proved wrong, when resistance first emerged. Before the treatment, the bacteria were uniformly susceptible to the drug. However, during the therapy, *Mtb* developed certain level of resistance which is in general, not acquired from other patients but rather, was intrinsically developed by the bacteria [63].

In the same year, para-aminosalicylic acid (PAS) was discovered, and was added to the treatment regime [64]. The combination of these drugs lowers generation rate of resistant mutants. This lowered rate, compared to the number of bacterial load during infection, should statically assure that there would not be any resistant mutant generated. As expected, in the initial stages of complementary drug therapy where patients were treated in hospitals, the compliance to the TB regime was high. However, in the 60's patients receiving

chemotherapy were not considered infectious and were shifted to outpatient treatment. This considerably lowered the patients' compliance towards TB regimens and partially contributed to the hike in the evolution of drug resistant TB. During 1985-1992, the United States faced major outbreak in MDR-TB, especially in patients with HIV [65]. Since then, MDR-TB incidence is rising and became a global problem, especially critical in the case of local threat when the outbreak occurs (Figure 1-5) [66]. MDR-TB is TB resistant to at least two first line-drugs: rifampicin and isoniazid. MDR can be successfully treated by second-line drugs however, it is often accompanied by severe adverse effects, mainly attributed to cycloserine, ethionamide and p-aminosalicylic acid [67]. MDR-TB is usually generated by patients failing to complete their treatment regime, thus curing the patients with MDR-TB is extremely important because MDR-TB is easier to prevent as compared to the prevention of transmission and emergence of the outbreak [68]. Extensively drug-resistant TB (XDR-TB) tuberculosis is defined as disease caused by *Mtb* with resistance to at least isoniazid and rifampicin, any fluoroquinolone, and to at least one of three injectable second-line drugs (amikacin, capreomycin, or kanamycin). In case of the rise of XDR-TB, the resistance is not acquired but most probably transmitted, as the same strains *Mtb* are usually found during these outbreaks [69].

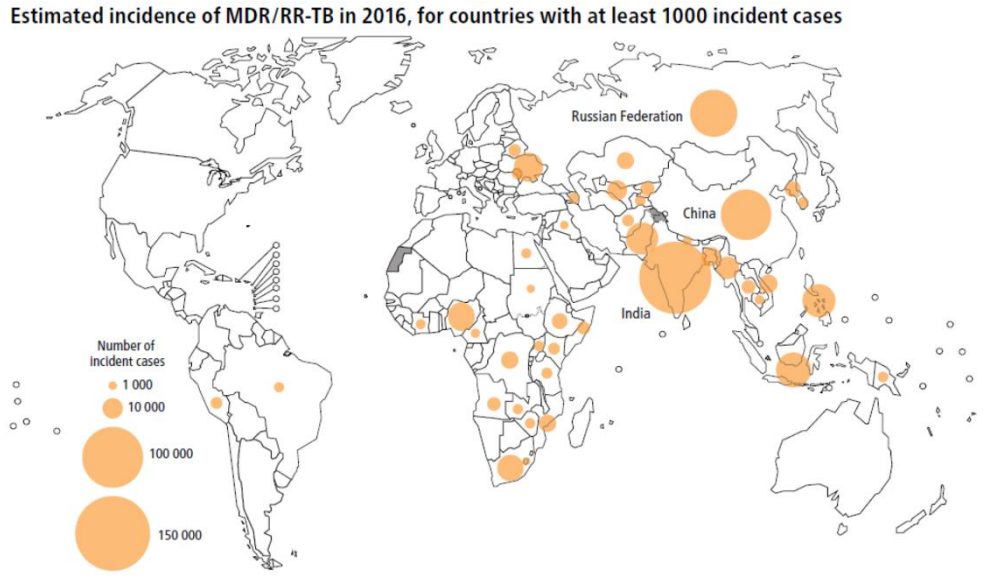

Figure 1-5: The estimated incidence of MDR in 2016. The countries with the largest numbers of multidrug-resistant TB or rifampicin-resistant (but isoniazid-susceptible) TB (MDR/RR-TB) cases (47% of the global total) were China, India and the Russian Federation, followed by Indonesia, Ukraine, Philippines and Indonesia [1].

Treatment of XDR-TB is at least 18–24 months, therefore there is an urgent need for new anti-TB drugs with novel mechanisms of action as a result of the rising cases of MDR-TB and XDR-TB.

1.3 Vaccination

The only approved vaccination against TB is the live *M. bovis* BCG (Bacillus Calmette-Guerin) vaccine. Starting from the virulent bovine strain, after 11 years and 230 subcultures every three weeks, Albert Calmette and Camille Guérin obtained a nonvirulent strain, which did not progress into pulmonary TB during experimental animal test. BCG was first introduced in 1921 as an oral vaccine [70]. The effectivity of BCG vaccination against pulmonary tuberculosis is highly variable and its risk-benefit and cost effectiveness is questionable [71]. Meta-study of the reported trials estimates at most a 50% reduction of the risk of TB infection [72]. Protection of the BCG vaccination often disappears during adolescent age, especially in high TB risk countries. Consequently, some counties with low incidence of TB stopped their vaccination program [73, 74]. Nevertheless, the BCG vaccination unarguably confers high protection against disseminated and miliary TB in infants and young children [75]. It is largely recommended for children in countries with high burden of TB and for the health workers in contact with TB patients. However, contraindicated for the groups with decreased immunity such as HIV positive children [76] and patients taking immunosuppressive drugs, which are the groups most likely to contract TB infection.

Being the only vaccination in use after almost hundred years underlines the lack of progress and negligence in the efforts to control TB and highlights a need for a new TB vaccine. Fortunately, after WHO declared a global emergency on TB [77] the efforts intensified and currently 15 new vaccines are in clinical trials [78]. New vaccine development is generally divided into three approaches. First, the need to improve the existing BCG vaccine or develop attenuated *Mtb* vaccine. Second, to use vectors such as viruses or protein adjuvants used as a booster dose. Third, development of the therapeutic vaccines which could shorten TB treatment [79]. From another point of view, vaccines could be divided into infection-blocking vaccines and disease-progression-blocking vaccines. The main challenge in the development of a new TB vaccine is the

activation of the host cellular immune response, as opposed to most of the vaccines, which activate humoral immunity, sufficient for treatment or eradication of the pathogen [80].

Table 1-1: Novel vaccines in clinical trials [78, 79]

Type of the vaccine	**Name**	**Usage**
Protein or adjuvant	M71	boost
	H1+IC31	prime, boost
	H4+IC31	boost
	H56+IC31	prime, boost
	ID93+GLA-SE	boost/ therapy
	M7a+AS01E	
Whole cell or extract	*M. vaccae*	therapy
	RUTI	boost/ therapy
	DAR-901	boost
Viral vector	MVA85A	boost/ therapy
	Ad5 Ag85A	prime, boost
	TB/FLU-04L	boost
	Crucell Ad35	boost
Recombinant	VPM 1002	prime, boost
Live attenuated	MTBVAC	prime, boost

Knowledge of the mechanism of protection by BCG vaccine is still limited. However, it was established, that immunisation against TB is conferred via T_H1-type cellular immune response, inducing an antimycobacterial response in macrophages mainly through the production of interferon-γ (IFN-γ). Boosting of immunisation by the same vaccine is not effective in this case wherein a second BCG vaccination can boost the protection against leprosy, however without additional protection against TB [81]. To improve incomplete protection of the BCG vaccine, the Modified Vaccinia Ankara (MVA) virus expressing antigen 85A (MVA85A) was developed. MVA is a strain of vaccinia virus, which after more than 500 passages, lost a whole range on genes, now hence, unable to replicate in mammalian cells. Therefore, it is regarded as highly safe [82]. Antigen 85A is a well conserved antigen in BCG strains and was shown to

provide immunisation [83]. This vaccine is using the recombinant virus vector, which is especially effective in boosting the already primed $CD4^+$ and $CD8^+$ T-cells [84]. Unfortunately, after hopeful initial findings, it seems that in recent trails MVA85A did not prove any enhancement in the protection against TB [85, 86]. Several other vaccine candidates are using virus vectors, such as recombinant replication-deficient human adenovirus Ad5 expressing antigen 85A (Ad5Ag85A) [87], recombinant adenovirus type 35 (CrucellAd35) [88] and modified influenza TB/FLU-04L [89].

In addition, a new class of vaccines uses protein with immune-modulating adjuvant. The advantages of utilizing this type of vaccines due to its composition composition: molecularly well-defined proteins. This assures for excellent safety, possibility of the slow-release formulation and makes them suitable for boosting [78]. The most commonly used adjuvant is a two-component IC31, combining an 11-mer antibacterial peptide and a synthetic, Toll-like receptor agonist, an oligodeoxynucleotide [90]. An example of such vaccines, H56:IC31, is composed of fused Ag85B, ESAT-6 and Rv2660c antigens and IC31 adjuvant. These different antigens were chosen to cover different stages of *Mtb* infection to trigger a broader immune response [91].

Whole cell or live attenuated vaccines, having the wide spectrum of antigens, including proteins, lipids and carbohydrates, are naturally superior to the protein-adjuvant vaccines. The main disadvantage of the protein-adjuvant vaccines are the safety concerns, wherein there are much more parameters to meet [92]. In live vaccines, the right balance between achieving attenuation, safety, survival ability, reproduction ability as well as assurance of strong and long-term protection is necessary [93]. Recombinant BCG vaccines (rBCG) are developed to enhance efficacy and reduce risk of the existing BCG vaccine. In BCG *ΔureC::hly* (VPM1002) vaccine, a gene coding for the urease C (*ureC*), has been replaced by a listeriolysin O encoding gene (*hly*) form *Listeria monocytogenes*, listerialysin, in order to enhance immunogenicity and antigen cross-presentation. The role of Urease C is to neutralise the phagosome. When deleted, the phagosome becomes acidic. At this acidic pH, listeriolysin disrupts the phagosomal membrane, leading to apoptosis, autophagy and ultimately, the release of the BCG antigens into the cytosol [94]. In the human trial, the vaccine achieved acceptable immunisation and safety profile [95]. VPM100 is currently

in phase IIb clinical trials in HIV positive children in Africa and a phase II/III is starting in India for the recurring TB. Another new type of TB vaccine, MTBVAC, is a live attenuated *Mtb* strain with chromosomal deletion of the virulence genes *phoP* and *fadD26* [96]. It was developed from the clinical Lineage 4 (Euro-American), isolate *M. tuberculosis* Mt103, one of the widest spread TB lineages [97]. During the first trials in humans, MTBVAC demonstrated acceptable safety, immunogenicity comparable to BCG [98]. This vaccine could potentially confer a longer-lasting protection, not only for miliary and disseminated TB infection in children, but also for TB infection in adults [92]. The above mentioned whole-cell vaccines use live bacteria. Another type of vaccination, such as therapeutic vaccine RUTI, is made of the detoxified fragmented *Mtb* cells. This vaccines aim is to prevent the progression of the LTBI into the active form [99]. Another example of the therapeutic dead whole-cell vaccine is the preparation of the heat-inactivated and lysed *M. vaccae*, fast-growing non-pathogenic saprophytic NTM [100, 101]. Both these vaccines are currently in clinical trials.

Although the new vaccine candidates seem promising, they still have to prove to be safer or more effective than BCG, which has been well established and utilized for more than four billion administrations. Until then, the control of the dissemination of TB infection has to rely on the usage of anti-TB drugs.

1.4 Currently used drugs in the treatment of tuberculosis

Currently used drugs in the treatment of TB target various cell mechanisms. The medications are usually taken in combinations to minimalize the risk of drug resistance as well as to increase the effectiveness of TB treatment. First-line drugs include isoniazid which functions by inhibiting mycolic acid synthesis, rifampicin inhibiting RNA polymerase β-subunit, ethambutol inhibiting arabinogalactan synthesis and pyrazinamide probably inhibiting *panD*. Drugs, which are in the clinical pipeline mostly target protein synthesis, the bacterial cell wall, DNA gyrase and respiratory chain complexes[102].

1.4.1 Isoniazid

Isonicotinic acid hydrazide - isoniazid (INH) (Figure 1-6) was discovered in 1952 as part of the efforts to synthesise analogs of the vitamin nicotinamide, which showed antitubercular activity. Surprisingly, INH was not part of the

synthetized analogs, but only an intermediate. Isoniazid is highly specific for the slow growing mycobacteria, with an MIC of 0.05 μg/ml for *Mtb* [103]. Isoniazid plays an important role in the initial days of treatment, when it is responsible for the majority of the bacterial killing [104]. The target of isoniazid still remains a mystery, despite being one of the most effective and widely used drugs against TB. It was suggested already in 1970 that INH inhibits synthesis of mycolic acid [105], however only 20 years later, the study of the mutant strains of *M. smegmatis* and *M. bovis* resistant to isoniazid revealed a missense mutation located *inhA* gene. *InhA* encodes for the NADH-dependent enoyl-acyl carrier protein reductase, thus confirming that INH does inhibit the elongation of the α-alkyl β-hydroxy fatty acids which are essential constituents of the mycobacterial cell wall [106]. This mechanism of action is well in line with the observation of INH induced morphological changes of the bacterial wall and INH bactericidal activity. Interestingly, *inhA* gene mutant strains were cross-resistant to ethambutol [107]. Other mechanisms of resistance to isoniazid includes mutation in *KatG* gene which is involved in the oxidative activation of the isoniazid prodrug into its active form [108]. The reactive species is formed by the mycobacterial enzyme KatG and forms adducts with NAD^+ and $NADP^+$ which subsequently tightly bind and inhibit InhA [109].

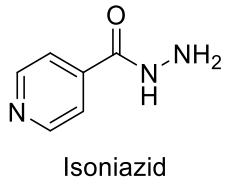

Isoniazid

Figure 1-6: Structure of isoniazid.

INH is metabolised by acetylation. A fraction of the population has a recessive trait of slow acetylation, which results in higher plasma levels of the drug. Alcoholic patients with liver damage or the consumption of PAS (second-line TB drug) may also influence the metabolism of INH. Both INH drug and metabolite are excreted by the kidneys, in which it passes out as urine. [110]. In other conditions where INH is not excreted adequately, adverse effects such as peripheral neuropathy - paraesthesia *e.g.* tingling of the feet, nausea, weakness and muscle atrophy. These adverse effects are usually reversible after withdrawal of the therapy. In rare cases, INH can induce lupus erythematosus and allergic reactions. INH was also reported to cause hepatotoxicity, however

sometimes it is attributed to the pathogen induced tissue damage. Most of the adverse effects are not serious or life threatening, even though they significantly lower the patients' adherence [111].

1.4.2 Ethambutol

Ethambutol (EMB) (Figure 1-7), was derived from a compound discovered in the random screen of compounds in a mouse infected by *Mtb*. A simple structure and a low molecular weight of EMB might suggest that its mode of action is non-specific, however only one of the stereoisomers (*S,S*) is active, which indicate that EMB it has a defined cellular target [112]. The biochemical studies showed that exposure to EMB leads to accumulation of β-D-arabinofuranosyl-1-monophosphodecaprenol, an intermediate in arabinogalactan synthesis. This evidence was suggesting that the mechanism of action involves the inhibition of the biosynthesis of cell wall [113]. As in the previous case, the mechanism of action was confirmed by generating *in vitro* resistant mutants. The mutations in *emb* gene were identified and overexpressed by a plasmid vector, which conferred EMB resistance to susceptible wild type (WT) *M. smegmatis*. This study suggested the defined cellular target of EMB, however the exact molecular target is still unknown.

Ethambutol is relatively safe, with retrobulbar neuritis as the only serious adverse effect. At the usual dose, the ocular toxicity is rare, however it is not always reversible, even after rapid drug withdrawal [114, 115].

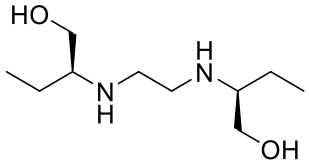

Ethambutol

Figure 1-7: Structure of ethambutol.

1.4.3 Rifampicin

Rifampicin (Figure 1-8) was synthetically derived from ansamycins after tedious structure activity relationships study and extensive medicinal chemistry efforts. Ansamycins are part of the natural product family, with aliphatic handle (Latin: ansa = handle) linking opposite sides of the aromatic moiety. They were isolated from the soil bacterium *Nocardia mediterranei*, with the subclass of rifamycins, particularly active against mycobacterium [116]. Rifampicin is,

together with pyrazinamide, the main sterilising drug in the TB regime. Rifampicin specifically inhibits DNA-dependent RNA synthesis by binding inside the DNA/RNA channel in the β subunit of prokaryotic RNA polymerase [117]. This mode of action was confirmed through x-ray crystallography and sequencing of the resistant mutants. The vast majority of the resistant strains had mutations in *rpoB* gene, which encodes for RNA polymerase subunit β. All these mutations were mapped to a close cluster of 13 amino acids [118].

Adverse effects of rifampicin include dose-dependent hepatotoxicity and allergic reactions. Immuno-allergic reactions can be mild, such as flu-like or gastrointestinal symptoms, but may also be severe, such as haemolytic anaemia and shock [119].

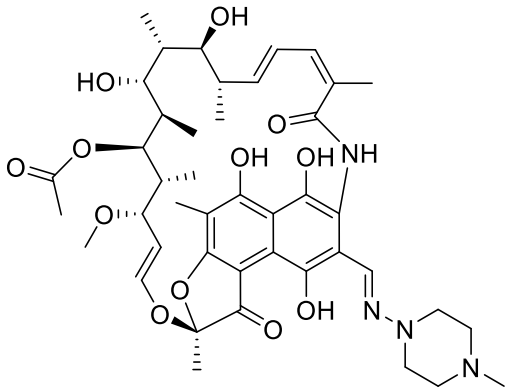

Rifampicin

Figure 1-8: Structure of rifampicin.

1.4.4 Pyrazinamide

Pyrazinamide (PZA) was discovered under the same effort of finding an active nicotinamide derivative which led to discovery of INH. PZA had only weak activity *in vitro,* but demonstrated potent anti-TB activity in mice [120]. The active compounds responsible for the anti-TB activity is pyrazinoic acid (POA). POA is the metabolite of prodrug PZA, converted by nicotinamidase/pyrazinamidase which is encoded by the *pncA* gene. Mutations in this gene are usually the major mechanism of resistance of *Mtb* to PZA [121]. Several different mechanisms of PZA were proposed, *e.g.* ionophore, fatty acid synthetase I, trans-translation - I 30S ribosomal S1 protein [120, 122, 123]. Recently, the generation of spontaneous-resistant mutants revealed a missense mutation in the aspartate decarboxylase, *PanD*. Inhibition of *PanD* results in the depletion of coenzyme A and it is suggested that this could be a main mechanism

of action of PZA [124]. The involvement of *PanD* in the mechanism of action of PZA is supported by isothermal calorimetry experiments proving that POA binds to the *PanD*, while inactive prodrug PZA does not bind [125]. Other missense mutations were found in the unfoldase ClpC1 associated with the caseinolytic protease complex, which might target proteins for degradation [126].

The most common adverse effect are: hepatotoxicity arthralgia, exanthema and nausea [127]. When PZA was used with rifampicin to treat LTBI, several fatal hepatitis incidents were reported. PZA seems to be most hepatotoxic of all first line drugs [128].

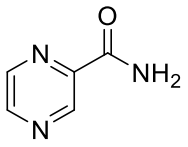

Pyrazinamide

Figure 1-9: Structure of pyrazinamide.

1.5 Recently approved drugs and drug candidates in the development

1.5.1 Delamanid

Delamanid, (brand name Deltyba, previous code name OPC-67683), dihydro-nitroimidazooxazole derivative is utilized as an oral treatment for MDR-TB. Its development was based on the class of nitroimidazofuran anticancer drugs known to have antibacterial activity. Compound CGI-17341 was found to have *in vitro* activity against *Mbt*, however, it also demonstrated strong mutagenicity, that were characteristic for this class of compounds. The introduction of the heteroatom in the 2-position decreased the mutagenicity and OPC-67683 showed potent activity against *Mtb* [129]. The mechanism of action of delamanid involves the interference of cell wall biosynthesis, in particular, they synthesis of methoxy mycolic acid and ketomycolic acid. The active compound seems to be the metabolite of delamanid, catalysed by the enzyme deazaflavin dependent nitroreductase (Rv3547). Thus, delamanid is a prodrug, which needs to be activated in the cell. During early trials, the MIC of delamanid was found to be in the excellent range between 0.006-0.024 μg/ml, which correlated with observed low *in vivo* doses. It is not metabolised and neither does it affect cytochrome P450 enzymes, which is especially important in patients co-

infected with HIV and were taking anti-retrovirals. Another advantage of delamanid is the post antibiotic effect on bacteria, which was comparable with that of rifampicin. There was no cross-resistance nor antagonist effect observed with first-line anti-TB drugs. Furthermore, delamanid's addition to the first-line regime enhanced the sputum conversion in MDR-TB after two months of treatment [130].

During clinical trials, the QT prolongation effect (lengthened interval between start of the Q wave and the end of the T wave in heart cycle observed on electrocardiogram) of delamanid was observed, however, this did not translate into any symptoms such as syncope or arrhythmia [130].

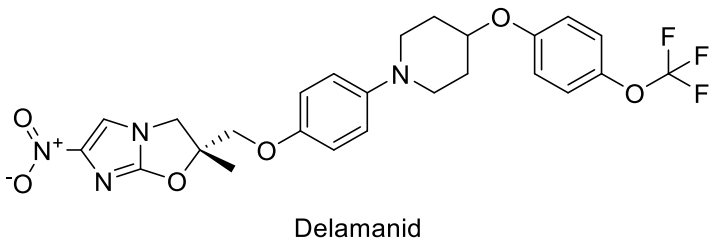

Delamanid

Figure 1-10: Structure of delamanid.

1.5.2 Pretomanid (PA-824)

A class of nitroimidazofuran anticancer drugs was found to have *in vitro* activity against *Mtb* and it was further investigated by the expansion into a series of 328 analogs. The mutagenicity was successfully eliminated and the activity was improved. PA-824, selected as the most effective in the murine model of infection, displayed activity against various mycobacterial strains in range of 0.015 to 0.25 μg/ml without cross resistance with other antituberculotic drugs [131]. The compound was active against both growing and dormant bacteria, suggesting a new mechanism of action. Later, the microarray analysis indicated that PA-824 is a prodrug, with two distinct mechanism of actions. The replicating bacteria seem to be inhibited with interfering mycolic acid biosynthesis [132], having the same mode of action as delamanid. The non-replicating bacteria appear to be killed via cyanide like respiratory chain poisoning, resulting in the drop of ATP levels, presumably due to the release of nitric oxide. Evidence for this mechanism of action was supported by investigation of the drug metabolism, in which des-nitroimidazole was found to be a major metabolite, Furthermore, NO scavengers conferred resistance to the drug [133]. Pretomanid, which was developed by the TB Alliance, had no

significant cytochrome P450 interactions nor activity against a broad range of gram-positive or gram-negative bacteria.

During a four months treatment on mice experiment, the combination of pretomanid, BDQ and moxifloxacin cured half of the mice, as opposed to the current four combination regimen, which did not cure any mice [134]. This finding suggests, that a new combination regimen with pretomanid, BDQ and another antibiotic could be as effective as a first-line regime [135] and could lead to shortening of TB treatment. In the Phase 2a (Dose-Ranging Trial), the dose of 100 mg or 200 mg pretomanid was found to be optimal for the safety and efficacy of this drug [136]. Afterward, pretomanid successfully passed phase 2b clinical trials, where it was used with the combination of moxifloxacin and pyrazinamide. During the 8-week study, the bactericidal activity was superior to the currently used regimen. In addition, the incidence of adverse effects was comparable to the other clinically used combinations of the drugs and this combination was considered as well tolerated [137]. Pretomanid is currently in phase 3 clinical trials in combination with BDQ and linezolid for drug resistant tuberculosis, with the aim to shorten and simplify the treatment.

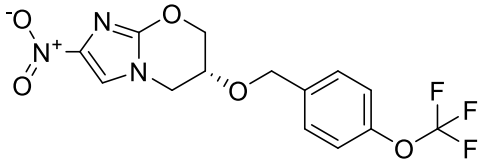

Figure 1-11: Structure of pretomanid.

1.6 Respiratory chain as a drug target

As shown above, most of the first-line and second-line antituberculotics target cell wall biosynthesis or protein synthesis. Recent discoveries identified a new hot target for the treatment of tuberculosis: the respiratory chain. The respiratory chain in *Mtb* is currently emerging as a new drug target because of the specific energetic requirements needed for survival of *Mtb* in the low oxygen and nutrient conditions inside TB lesions [138]. *Mtb* has several mechanisms to control its energetic homeostasis including upregulation of genes, whereby most of them are controlled by the DosR–DosS/DosT (Dormancy survival Regulator) [139]. DosR can activate the non-proton-pumping cytochrome *bd* oxidase and deactivate the less energy-efficient cytochrome *c* oxidase [140] (Figure 1-13)

while entering dormant stage. One of the key complexes of the respiratory chain is the NADH:ubiquinone oxidoreductase also called the complex I [141]. This enzyme is essential for the formation of the ion-electrochemical gradient. The type-II NADH:ubiquinone oxidoreductase, expressed during growth in presence of oxygen in *Mycobacterium,* is absent in human mitochondrial electron transfer chain [142]. This gives an excellent opportunity to design selective and effective anti-TB drugs, for instance the class of phenothiazine analogs [143]. Dormant bacteria are also very sensitive to change in the already low ATP level. Thus, interference with ATP synthesis of hydrolysis is a very attractive drug target [138].

1.6.1 Q230

During the extensive phenotypic high-content screening of 121,156 compounds, 106 active compounds were identified. This screening was performed in infected macrophages, which closely mimics physiological condition and directly reflects the penetration of compounds into the cells as well as the possibly efflux of these compounds. Two imidazopyridine amide derivatives, IPA01 and IPA02, were further developed, resulting in 477 derivatives [144]. IPA Q203 was evaluated as the best lead with MIC_{50} for *Mtb* H37Rv of 2.7 nM in culture broth medium and at a MIC_{50} of 0.28 nM inside macrophages. The putative binding site was elucidated via whole genome sequencing, where all of the six spontaneously-generated resistant mutants to IPA derivatives had a single amino acid mutation in the cytochrome *b* subunit. This hypothesis was supported by the drop of cellular ATP production in the presence of Q203 [145].

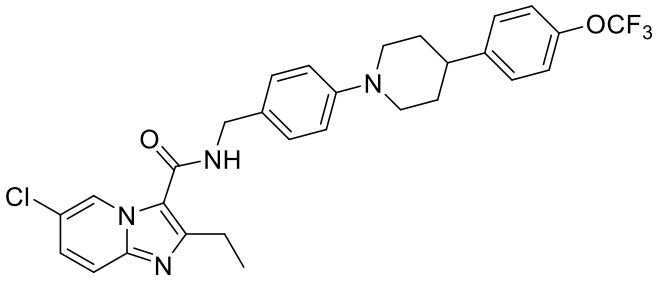

Figure 1-12: Structure of Q203.

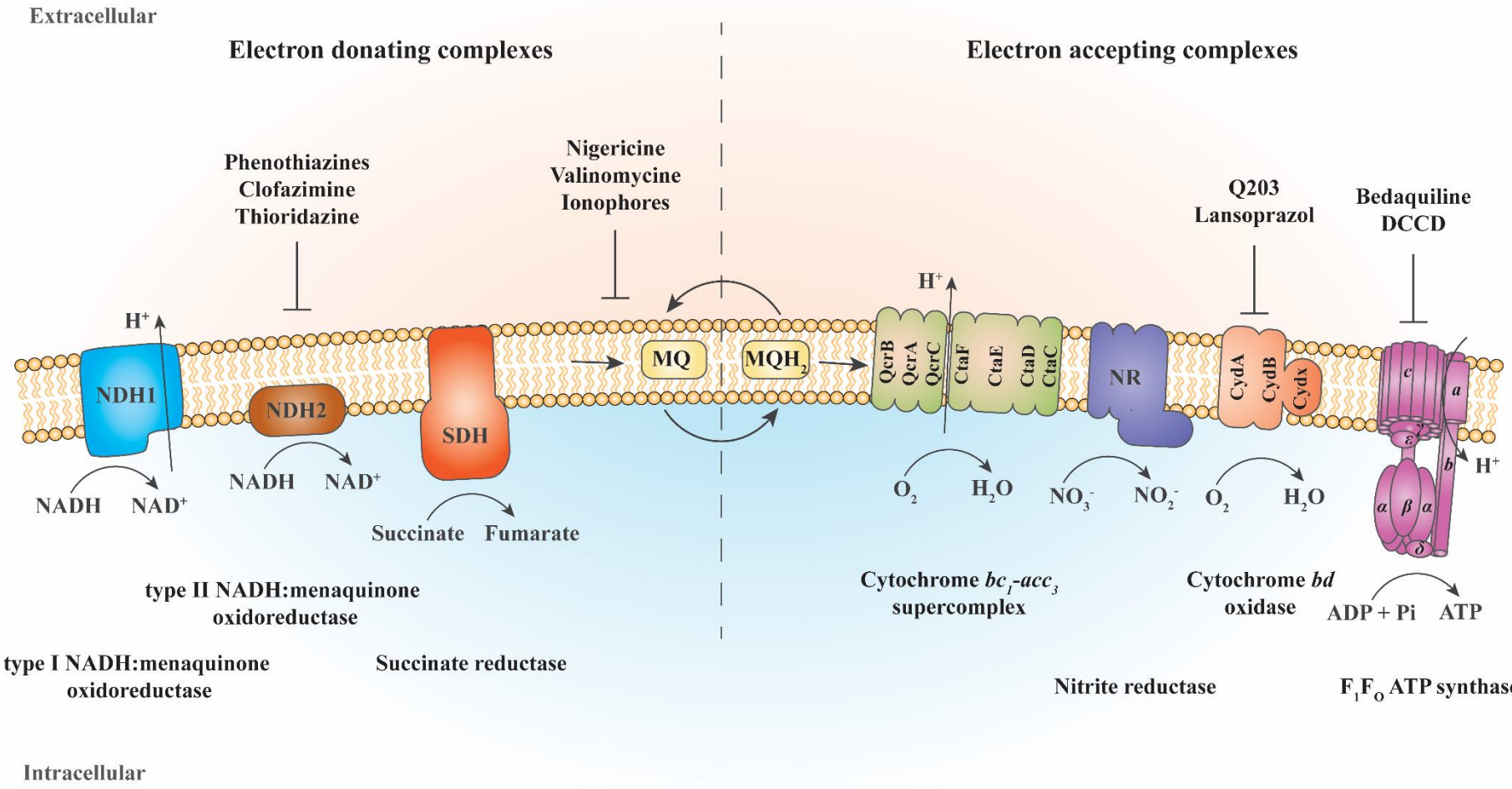

Figure 1-13: Respiratory chain of *Mtb* [138]. Cytochrome *c* (green) is downregulated under hypoxic conditions and is replaced by cytochrome *bd* (orange), which has a higher oxygen affinity. DCCD - dicyclohexylcarbodiimide; NDH - NADH dehydrogenase; NR – nitrite reductase; SDH - succinate dehydrogenase.

1.6.2 F_1F_O ATP synthase, the catalyst for ATP-formation

One of the proteins in the respiratory chain, F_1F_O ATP synthase, is recently getting increased attention as a drug target. The F-ATP synthases are membrane located enzymes, which convert a transmembrane electrochemical ion gradient into ATP or in the opposite way, creating the ion-gradient by the hydrolysis of ATP. F-ATP synthases are vital for most biological processes, especially in the case of *Mtb*, subjected to the stringent conditions inside macrophages as well as oxygen and nutrient depleted environment of the granulomas [146].

Although the structure of F_1F_O ATP synthases varies among different domains of life, their basic composition remains unchanged: the simplest prokaryotic F-ATP synthase is composed of a soluble F_1 part containing α, β, γ, δ, ε subunits (α_3:β_3:γ:δ:ε) and the membrane-embedded F_O part consisting of *a*, *b* and *c* subunits (*a*, b_2, c_n). The $\alpha_3\beta_3$ subunits form a hexamer, which is responsible for synthesis or hydrolysis of ATP. The central stalk, composed of ε and γ subunits, is connected to the rotating transmembrane *c*-ring subunit. The central stalk drives conformational changes inside the α-β interface for the synthesis of ATP. The single peripheral stalk consists of two *b* subunits and one δ subunit, which serves as a stator and links subunit *a* and the rotating *c*-ring of the F_O part with the catalytic $\alpha_3\beta_3$ hexamer. The *Mtb* F_1F_O ATP synthase has several unique features (Figure 1-14), such as a shorter C-terminal α-helix of subunit ε and a unique C-terminal helix of subunit α [147]. Moreover, the stator stalk has one subunit *b* genetically fused with subunit δ and another shorter subunit *b*' missing the C-terminal, as opposed to two identical subunits *b* and separate subunit δ in most F_1F_O ATP synthases [148]. Finally, subunit γ has a 13 amino acid loop insertion, which is found only in *Mtb* F-ATP synthases [149]. All these differences make the *Mtb* ATP synthase a wonderful drug epitope, which allow us to specifically target only *Mycobacterium* without influencing human F-ATP synthases. One aim will be to understand whether these insertions or deletions in the α, ε, γ or *b* subunits cause functional and regulatory changes in the *Mtb* F-ATP synthase. If so, the uniqueness of these structural functions, which exist only in mycobacterial species, would form a platform to specifically target the *Mtb* F-ATP synthase.

1.6.2.1 Novel antituberculotic drug Sirturo (bedaquiline, BDQ)

The first TB drug approved by U.S. Food and Drug Administration after more than forty years is bedaquiline (trade name Sirturo, code names TMC207, Figure 1-14) [150]. This drug was discovered by phenotypic screening and was shown to inhibit ATP synthesis activity by inhibiting ion-translocation inside the *c*-ring [151]. With this drug, it seemed that the problem of tuberculosis would be solved, since the compound was active even against MDR-TB strains. However, serious adverse effects such as nausea, headache and chest pain emerged [152]. Moreover, the later clinical trial studies suggested that a group taking BDQ had higher mortality than the control group, possibly caused by QT interval (depolarization and repolarization of the ventricles) prolongation that can lead to arrhythmia. Therefore, Sirturo will be now used only for the treatment of MDR-TB. As such, there is still the need of a novel anti-TB drug. Experiments have shown that BDQ interferes with the *c*-ring [153], however it has been revealed that BDQ can also modify the coupling of the *c*-ring and the central stalk subunit ε and block the transfer of energy [147].

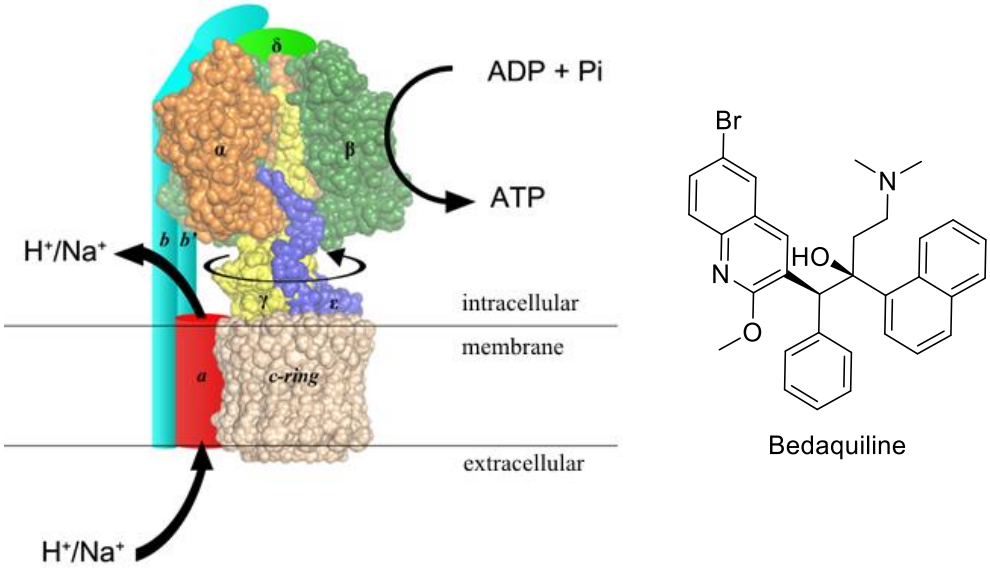

Figure 1-14: Model of the F_1F_O ATP synthase (left) and structure of the drug Sirturo (right). The *Mtb* F-ATP synthase model is based on the PDB ID: 3OAA (F_1, *E. coli*) and 1C17 (*c*-ring, *E. coli*). Orange α and dark green β subunits form the static hexameric catalytic part. One α and β subunit were removed to reveal the γ (yellow) subunit acting as the central stalk rotor. The regulatory ε subunit in blue is in the extended form, reaching in to the catalytic subunit. The structurally unknown *a, b, b'* and δ are shown as cartoon in red, light blue and light green, respectively.

1.6.2.2 Subunit γ of the *Mtb* F-ATP synthase as a drug target

In my work, I will be focusing on the γ-subunit of the F-ATP synthase. As proposed by Priya *et al.* [149] subunit γ is a new potential drug target offering a highly specific binding site. Sequence alignment of subunit γ and corresponding subunits from other organisms has revealed a unique sequence in *Mycobacterium*. The extra loop (Figure 1-15) is 13 amino acids long ($\gamma_{165–178}$) and is located in the proximity of the *c*-ring proposed to be involved in coupling ion-transport with ATP synthesis [149]. The existence of this unique $\gamma_{165–178}$ loop only in the *Mycobacterium* F-ATP synthases (Figure 1-16) makes this epitope specific and would thus minimize adverse effects.

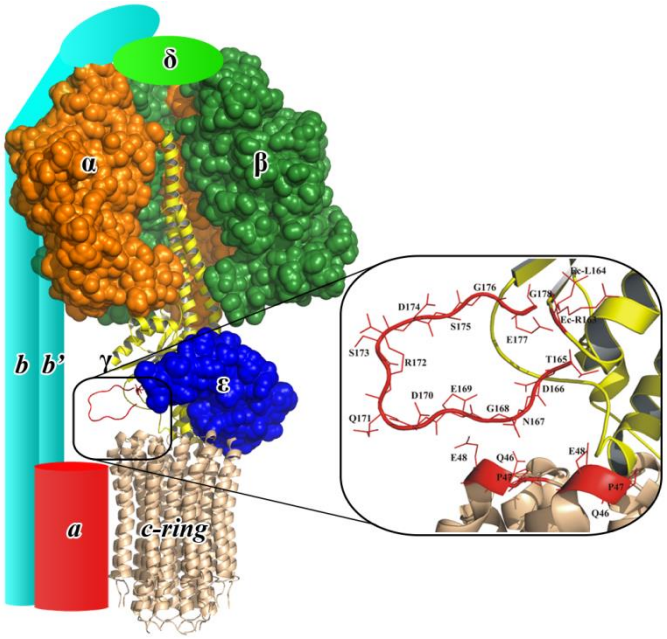

Figure 1-15: Structural model of the mycobacterial F-ATP synthase. Subunits α (*orange*) and β (*green*) form the static hexameric catalytic part. One α and β subunit were removed to reveal subunit γ (*yellow*) subunit acting as the central stalk rotor. The regulatory ε subunit in blue is in the extended form reaching in to the catalytic subunit. The unique mycobacterial γ-loop is shown in red in the vicinity to the *c*-ring loop residues Q46 to E48 of *M. phlei* (*wheat*; [8]). The subunits *a*, *b*, *b'* and δ are shown as cartoon in the red, light blue and light green, respectively.

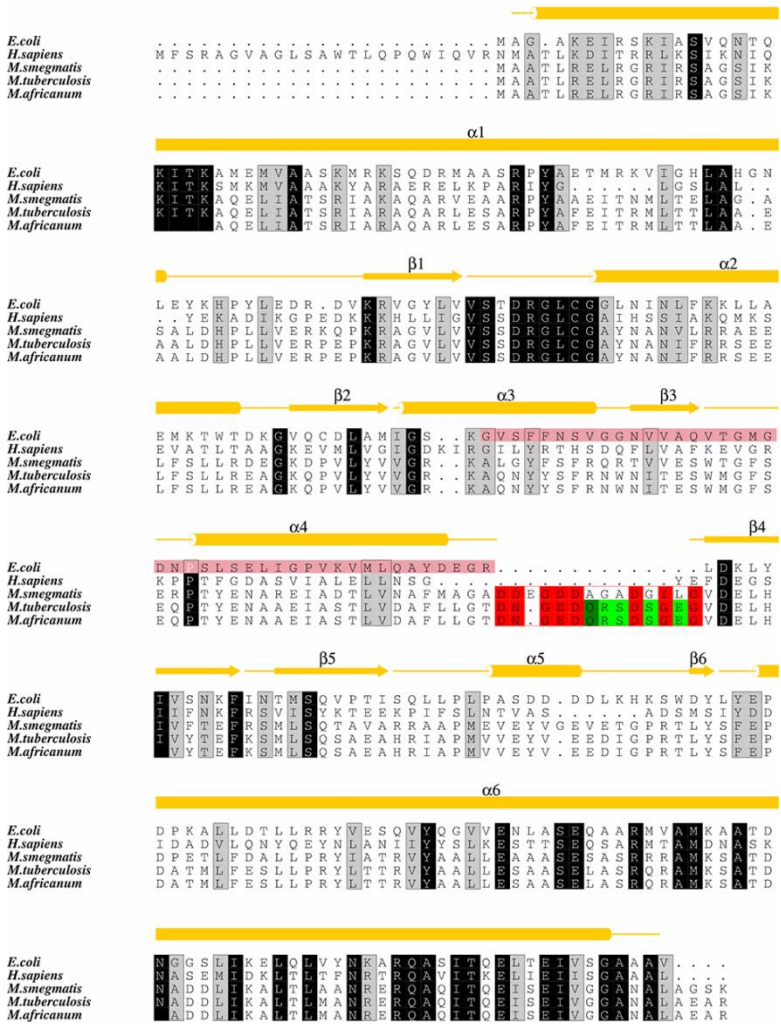

Figure 1-16: Amino acid sequence alignment of γ subunits. Amino acid sequence alignment of subunit γ of the *E. coli*, human mitochondrial, of the non-pathogenic *M. smegmatis* and the pathogenic *M. tuberculosis* HR37v as well *M.* africanum F_1F_O ATP synthase. The secondary structure of *E. coli* γ is based on the crystal structure PDB ID 3OAA[3][21]. The residues of the unique γ-loop are highlighted in red frame, whereby identical amino acids are marked in red and identical residues only in the two pathogenic forms are marked in green. The Q-residue is proposed to interact with the loop of subunit *c* [13]. Helix α3, β3 and α4 (*salmon*) are described to form a structural path to interact with the C-terminal domain of the catalytic β subunit.

1.7 Aims of the dissertation

The respiratory chain of *Mtb,* especially the F_1F_O ATP synthase, is an attractive and validated drug target. In the γ subunit of the F_1F_O ATP synthase unique $\gamma_{165–178}$ loop has been identified as a potential drug target, and its regulatory role has been hypothesised. However, until now, its role has not been experimentally characterised. This study aims to experimentally characterise the $\gamma_{165–178}$ loop on the IMVs of the *M. smegmatis* in the ATP synthesis and hydrolysis assay. The ATP synthesis assay was previously successfully employed in the characterisation of BDQ, however ATP hydrolysis in *M. smegmatis* has not been observed. A modified, more direct ATP hydrolysis assay is proposed. Establishing these assays would as well provide a platform for the testing of the compounds designed to target the F_1F_O ATP synthase.

Unfortunately, no high-resolution structure of *Mtb* γ subunit of F_1F_O ATP synthase is available, however the NMR structure of the γ loop was determined by Dr. Priya Ragunathan [149]. Therefore, to study and target the $\gamma_{165–178}$ loop, a homology model of the *Mtb* γ subunit of F_1F_O ATP synthase will be built. This model would serve as a starting point for the modelling and docking studies, leading to the identification of the novel compounds targeting ATP synthesis and hydrolysis in *Mtb*.

Subsequently, the identified compound will be screened for the growth inhibition of *M. smegmatis*. To validate the intended mechanism of action of the hit compounds, it will be tested in the ATP synthesis and hydrolysis assay. To fully characterise the hit compound, whole cell ATP synthesis assay as well as the grow inhibition different *Mycobacterium* strains is proposed. Furthermore, to investigate the drug-like properties, the hit compound will undergo basic pharmacokinetic and pharmacodynamic characterisation.

To obtain the hit compound in the sufficient quantities, a viable synthesis has to be proposed. Following this synthetic route, the analogs of the hit compound, will be synthetized and tested. Collected data will be analysed to establish a structure-activity relationship model. Based on this model, next series of modifications will be proposed to further improve the activity of the hit compound.

Modelling and docking studies of the *Mtb* F_1Fo ATP synthase

2. Modelling and docking studies of the *Mtb* F_1Fo ATP synthase

2.1 Homology modelling

To carry out the modelling and docking studies, an up to date model for the *Mtb* F_1F_O ATP synthase had to be built. Unfortunately, the high resolution crystallographic structure of this enzyme has not been resolved for *M. tuberculosis*. Therefore, a homology model based on the existing structures from other organisms was generated. Structure PDB ID: 2WPD (resolution 3.43 Å, by Dautant *et al.* 2010 [154]) from yeast was used as a template. There were available higher resolution structures of the individual subunits, however, the subunits from separate homology models of the *c*-ring and F_1 part didn't fit together well after protein-protein docking. 2WPD had both *c*-ring and F_1 parts solved together. This feature is essential for the modelling of the interface of γ subunit and *c*-ring, as most of the structures of the F_1 part and *c*-ring are obtained separately, and therefore lacking the information about respective distance and orientation in space. Thus, creating a homology model presented a very crucial step, since all the further work will be based on these modelling studies. A homology model including the mycobacterial $\gamma_{166\text{-}179}$ loop was created using Discovery Studio 3.5.0.12158 (Accelrys). Sequences of *Mtb* strain H37Rv subunit γ (P9WPU9) and subunit *c* (P9WPS1) were obtained from UniProt. Sequence identity of 2PWD and *Mtb* is relatively good with 29.39% for γ subunit and 34.21% for subunit *c*. The sequence alignment for the homology model was done with the secondary structure taken under into consideration (Figure 2-1).

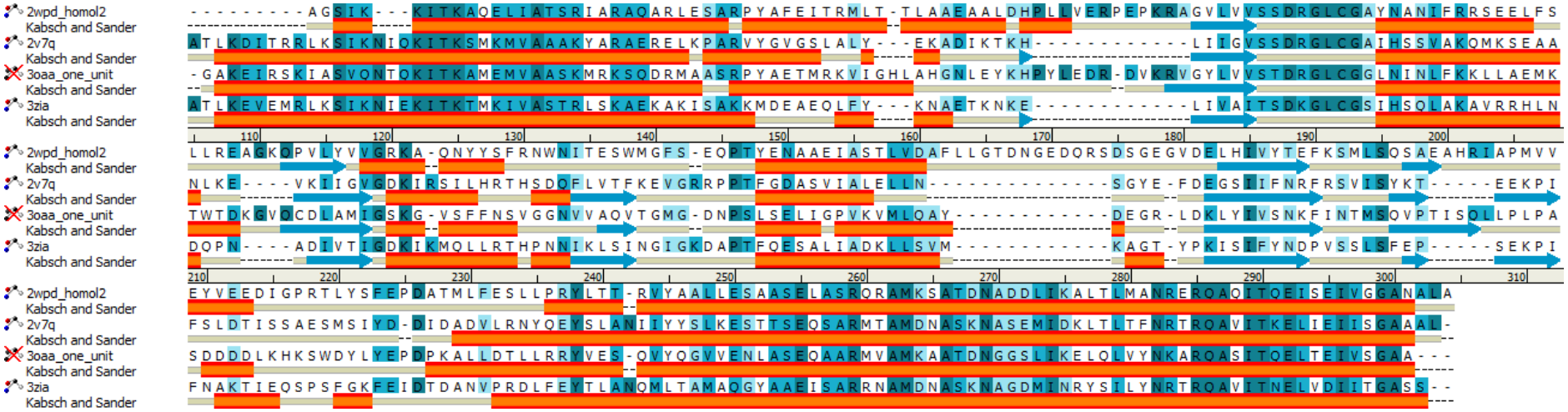

Figure 2-1: Sequence alignment for the homology model template, considering the secondary structure. **2WPD** homology model of *M. tuberculosis*; **3ZIA:** *S. cerevisiae* inhibited by IF1. 2.5Å [155]; **2V7Q:** bovine, inhibited by monomeric form IF1, 2.1Å [156]; **3OAA**: *E. coli* inhibited by epsilon, 3.26Å [157].

The model was generated by substituting yeast amino acid residues in the model with residues from *Mtb*, minimizing the model energy and repairing steric clashes together with other energetic or spatial conflicts. The most challenging task was to model the extra loop, because there is no template available. Several loop models were generated and examined (Figure 2-2). The correct group of structures was chosen based on the previous gamma loop computational and NMR studies (Figure 2-2C [149]) and the model with the lowest energy was retained for docking (Figure 2-2A).

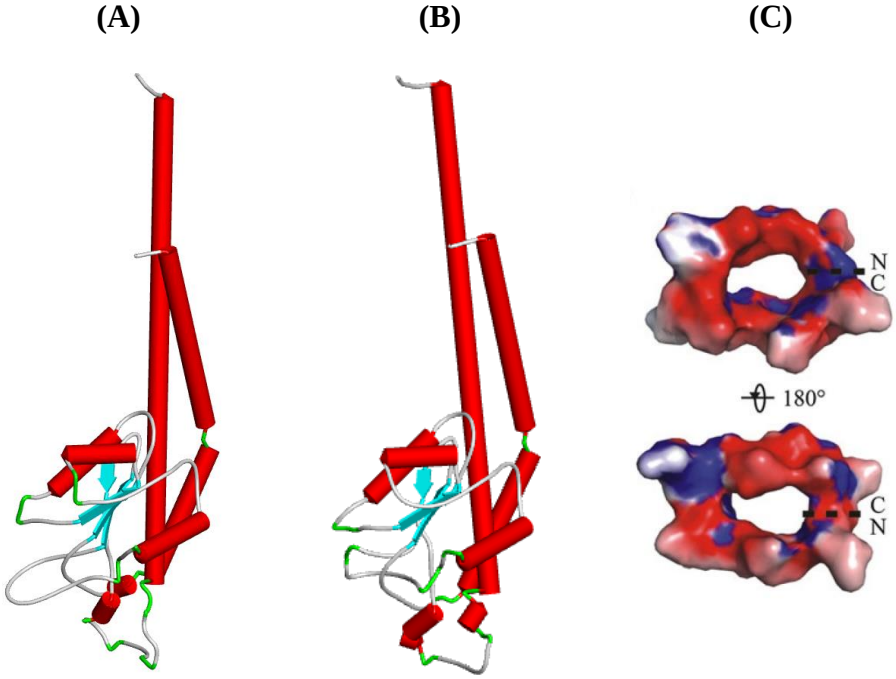

Figure 2-2: Examples of the different gamma loop models generated by Discovery studio with extended $\gamma_{166\text{-}179}$ loop (A) and packed $\gamma_{166\text{-}179}$ loop (B). The extended model was chosen based on the NMR structure of the $\gamma_{166\text{-}179}$ loop (C) [149].

The resulting homology model (Figure 2-4) was validated with ProCheck [158]. Ramachandran Plot statistics (Figure 2-3) showed good overall model quality with 91.7% residues in the most favoured regions, 6.5% in the additional allowed regions, 1.0% in the generously allowed regions and 0.8% in the disallowed regions.

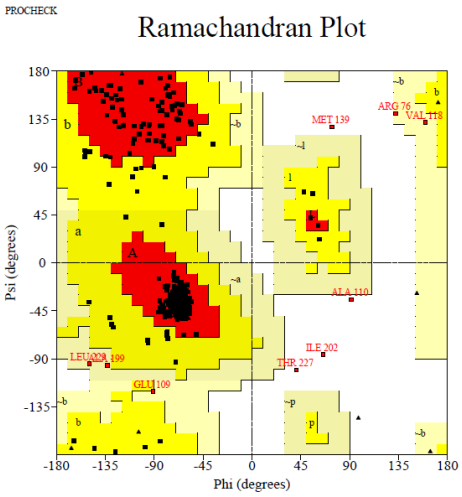

Figure 2-3: Ramachandran Plot of the homology model. Red areas depicting most favoured regions, yellow for additional allowed regions and beige for the generously allowed regions.

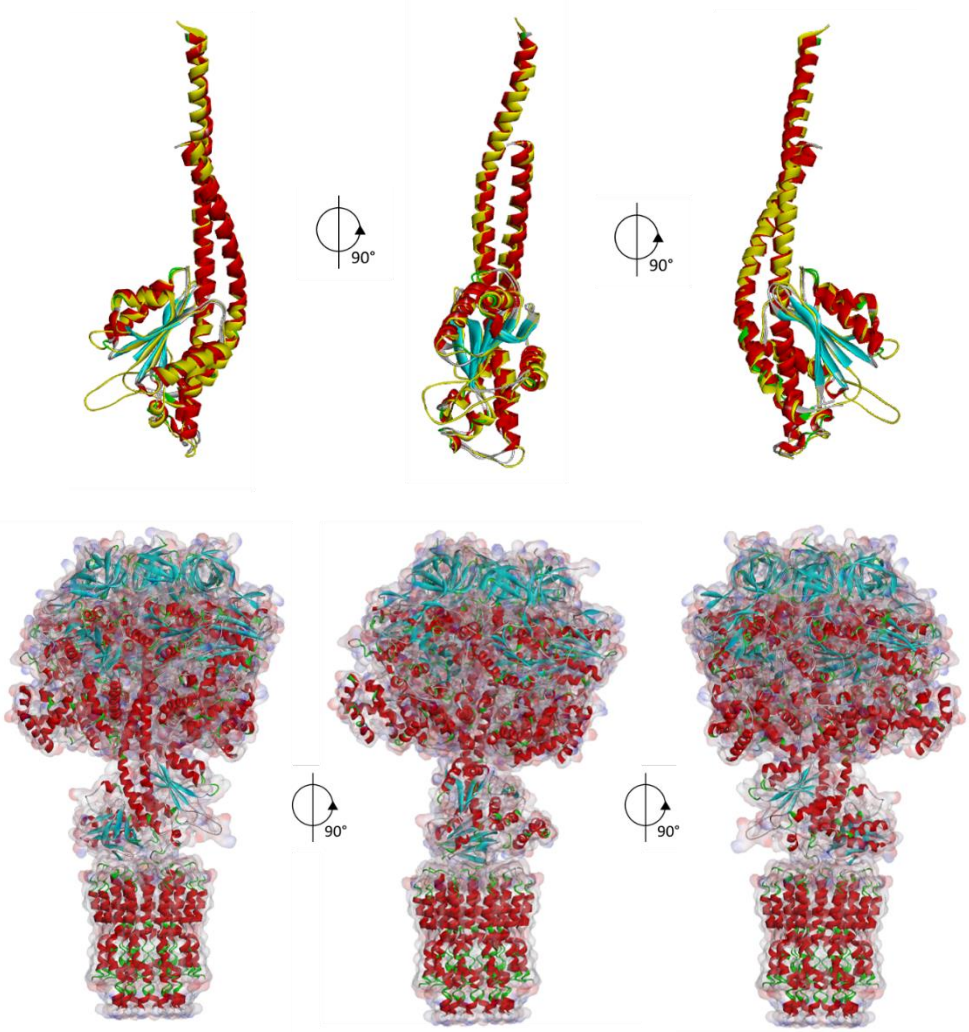

Figure 2-4: γ Subunit featuring the γ loop superimposed with the original 2PWD structure (top) and the final homology model (bottom).

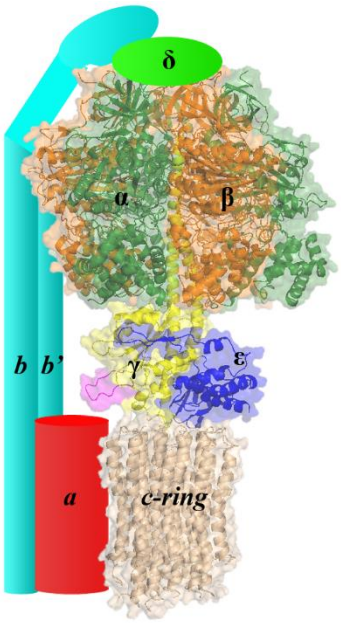

Figure 2-5: The arrangement of subunits of the *Mtb* F_1F_O ATP synthase is based on the homology model (template PDB ID: 2WPD, yeast). Orange α and dark green β subunits form the static hexameric catalytic part. One α and β subunit were removed to reveal γ (yellow) subunit acting as the central stalk rotor. The regulatory ε subunit in blue is in the contracted form. The γ166-179 loop is shown in magenta at the interface of the γ subunit and the wheat color *c*-ring. The structurally unknown a, b, b' and δ are shown as cartoon in the red, light blue and light green, respectively.

2.2 Virtual screening

The ChemDiv library (Downloaded from ZINC [159]) was used for the virtual screening because of its size and even sampling of the chemical space. The library contained approximately 1.5 million structures. In the first approach, all the compounds, that did not meet Lipinski and Veber's rules (i.e. did not have drug-likeness properties) were filtered out. According to Lipinski, drug-like compounds have to present these properties: the molecular mass lower than 500, no more than five hydrogen bond donors, less than ten hydrogen-bond acceptors and a Log P value lower than 5 (or MlogP . 4.15) [160]. Veber's rule ensures good bioavailability of the compounds by adding two more parameters: less than 12 rotatable bonds and a polar surface area smaller than 140 $Å^2$ [161]. By using these two sets of parameters, 10% of the compounds were filtered out. Subsequently, the filtered library was enriched by pharmacophore screening and subjected to docking (Figure 2-6).

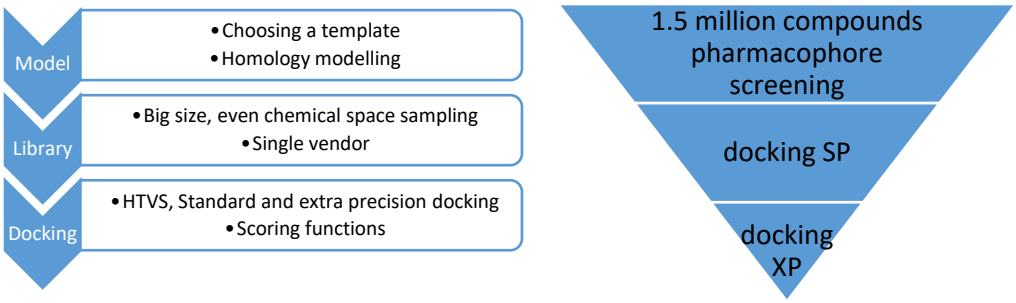

Figure 2-6: Modelling and docking workflow (left) and enriching the compound library by pharmacophore screening with by subsequent docking (right).

2.2.1 Pharmacophore modelling and screening

High-precision docking of a library with 1.5 million structures would be very lengthy and computationally expensive, so the docking to the $\gamma_{166\text{-}179}$ loop and *c*-ring interface was done in multiple steps. First, with help of Dr. Amaravadhi Harikishore from our lab, pharmacophore modelling was used following the previously reported workflow [162].

Pharmacophore modelling is based on identifying, clustering and generalising the key features responsible for the interaction of the ligand and the biding site resulting in the activation (or inhibition) of the biological response. These features usually consist of hydrogen bond donors and acceptors, which in general are responsible for most of the binding energy, hydrophobic centres and steric constraints, which delimits the size of the binding site (Figure 2-7) [163]. Pharmacophore modelling can be divided into ligand based pharmacophore modelling, analysing the common features of the series of active compounds, and structure based pharmacophore modelling, analysing the known structure of the biding site. As, to our knowledge, there are no inhibitors exploiting the γ subunit and *c*-ring interface, the structure based pharmacophore modelling was used.

Because of the great variety of possible interactions in the binding pocket, the initial pharmacophore modelling results in generation of hundreds of features, and therefore the number has to be reduced to typically three to seven features. Fewer features could be too general, not selective enough to effectively filter and enrich the library, and the opposite, too many features could be too specific and would yield too few or no hits [164]. First, similar and spatially close features are clustered and represented as a single feature, however the total number would

be still too high. Therefore, features have to be handpicked, based on the knowledge of the mechanism of action, structure of the known ligands or of the biding pocket, and should represent the largest common denominator for the active compounds. With this approach, the number of features significantly reduced from initial 1488 features to few dozen, which significant and representative of the binding site (Figure 2-8). Several combinations were of features were examined and the best performing pharmacophore model was used to enrich the library.

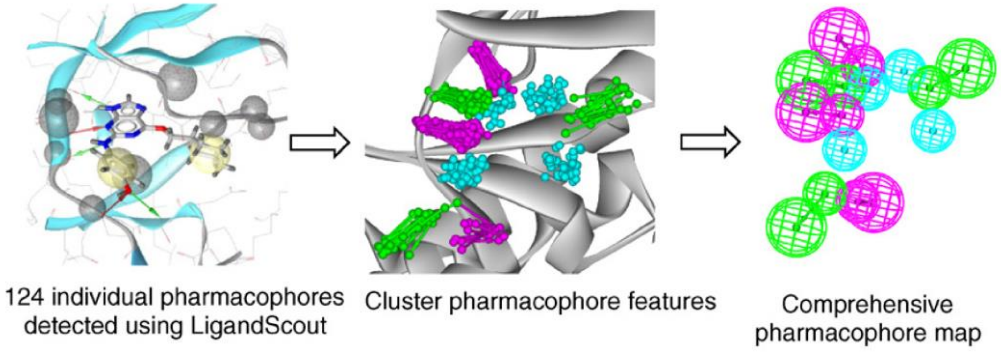

Figure 2-7: Generation of the structure based on the pharmacophore model in Discovery Studio [164].

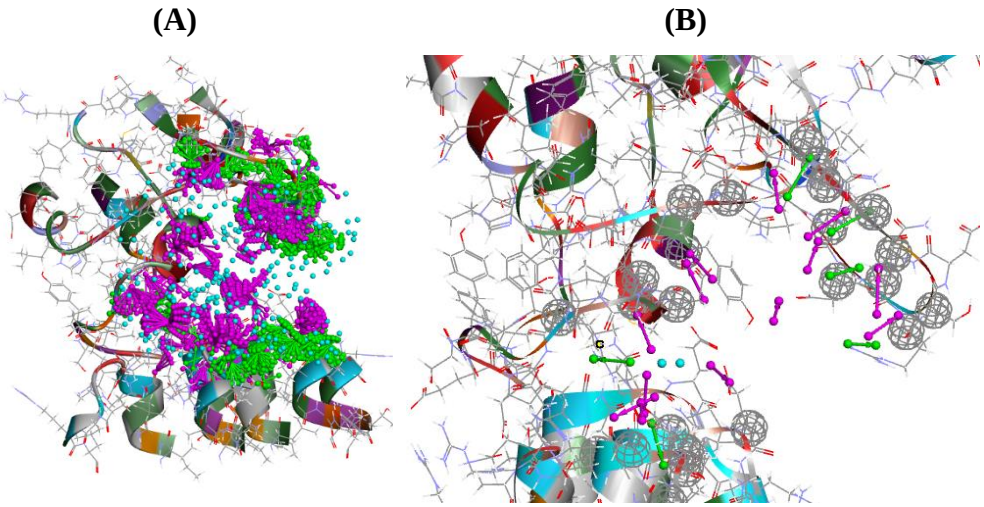

Figure 2-8: Ensemble of 1488 features initially generated. (A), compared to the significantly reduced number of clustered, filtered and handpicked pharmacophore features. Pharmacophore model of the proposed target interface of the γ-loop and *c*-ring. Hydrogen bond donors in magenta, hydrogen bond acceptors in green and exclusion volumes (steric constraints) in grey (B).

However, this modelling approach has its limitations: First, the human factor in picking the features to build the model can lead to biased models and

there is no standard for how to build one. Secondly, a library containing only few of several possible conformations, so the potential good ligands might be filtered out. Third, the fast and efficient screening comes in cost of overgeneralisation, and not being able to count in complex interactions and mechanisms, which might again lead in filtering out the active compounds [165].

2.2.2 Ligand library docking and results

With the pharmacophore in hand, the compound library was efficiently filtered based on the simple pharmacophore query. Afterwards, the upper fraction of the compounds was taken for docking in Maestro. Virtual screening was done using Glide module of Maestro, version 9.4.047 (Schrödinger). Docking grid was created with inner box size of 10 x 10 x 10 Å and outer box size of 22 x 22 x 22 Å (VdW radii of protein atoms scaled by 1.00 and charge cutoff for polarity 0.25). The first iteration of docking was done with Standard precision (SP), then further filtered the top-scoring compounds with Extra precision (XP) docking (Fig. 4). (VdW radii of ligand atoms scaled by 0.80 charge cutoff for polarity 0.15). Resulting compounds were ranked by consensus score of nine different scoring functions with Maestro's Glide XP score (the estimated binding affinity [166]) as the primary scoring function. The best 81 compounds were purchased from eMolecules (La Jolla, CA, USA).

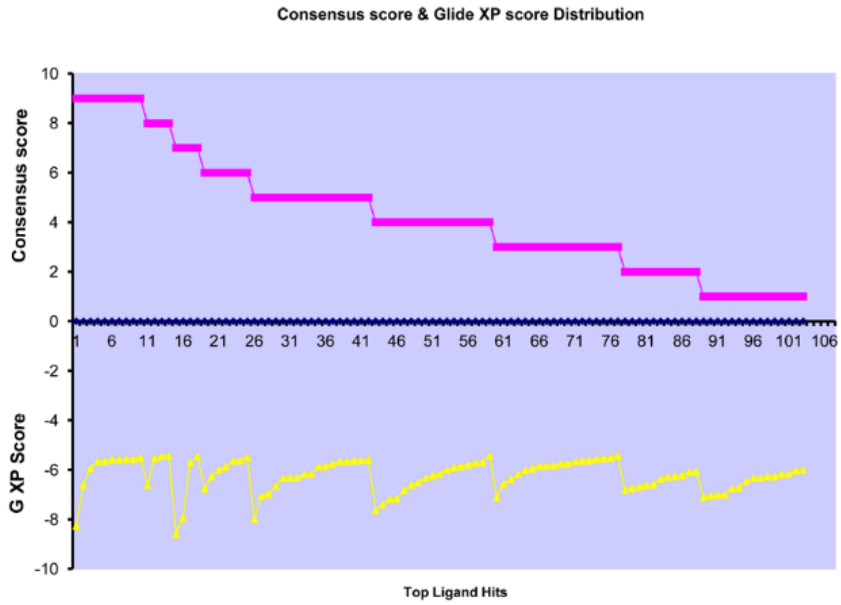

Figure 2-9: Consensus score of the top scoring ligands with G XP score as the Primary scoring function.

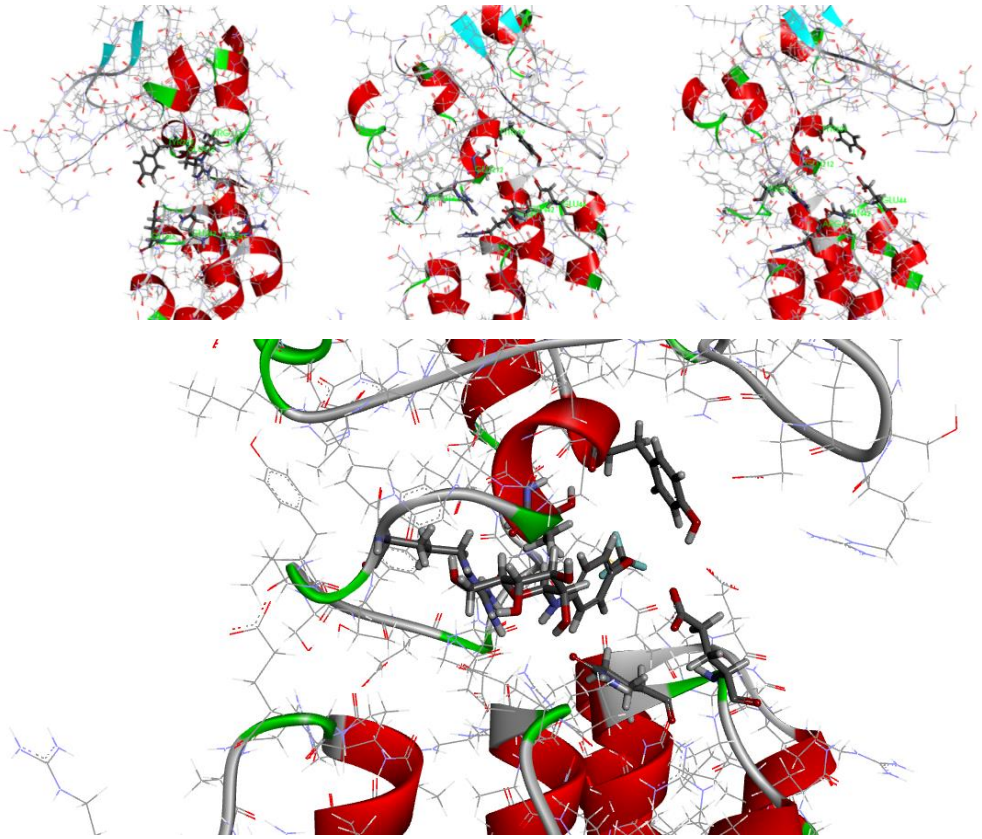

Figure 2-10: Amino acid residues contributing the most interactions for top 100 scoring poses. *c*-ring: R41, Q42, E44; γ subunit: Y209, R217, E212.

The top scoring ligands were examined and analysed. Based on the number of interactions for top 100 poses, the most interactions are generated by R41, Q42, E44 from the *c*-ring and Y209, R217, E212 from the γ subunit. These γ subunit residues are from the globular bottom part of the central stalk (Figure 2-10, Figure 2-11). It seems that the γ-loop is not providing the main interactions, however it might contribute by creating a cavity, and as later discussed, might have a functional and regulation role in the mycobacterial F_1F_O ATP synthases.

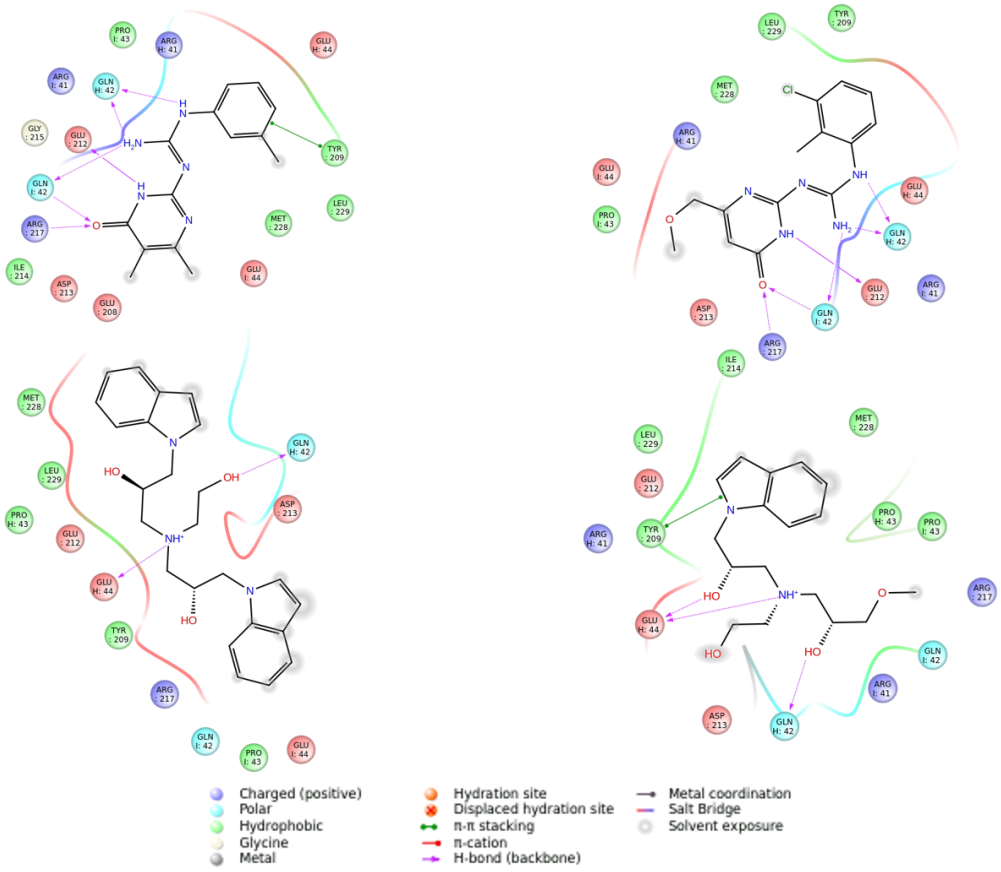

Figure 2-11: Schematic map of the different interactions between ligands and binding site.

Later microbiological testing identified two hit compounds, compound 6 and 2-3. Compound 6 with ZINC number 09573292 scored very well in the consensus scoring function by ranking in the top 20% in seven scoring functions out of nine. The glide XP GScore value -5.706 was also good and was overall ranked 17th.

Compound 2-3 with ZINC number 00092051 had very low consensus score, ranking in top 20% only in one scoring function out of nine. However, compound 2-3 scored very well in the glide XP GScore: -7.011 (10th best).

.

Microbiological and biochemical evaluation of the new *Mtb* F_1F_O ATP synthase inhibitors

3. Microbiological and biochemical evaluation of the new *Mtb* F_1F_O ATP synthase inhibitors

Parts of this chapter have been adapted from a manuscript that was published in The FEBS Journal [167]. Adam Hotra was a first author, was involved in the preparation of the manuscript, and took part in all experiments discussed in this chapter.

3.1 Materials

Phusion and Taq DNA polymerases were obtained from Thermo Fischer Scientific (USA); restriction enzymes were purchased from NEB (USA). Chemicals and antibiotics: kanamycin, hygromycin, rifampicin, streptomycin and dequalinium chloride, were purchased from Sigma-Aldrich (USA), antibiotic BDQ was purchased from Genegobio (USA). Media and their supplements for strain cultivation: Middlebrook 7H9, Middlebrook 7H10, Luria-Bertrand (LB), Dubos oleic agar, ADC and OADC, were purchased and prepared according to the manufacturer's instructions from Difco Laboratories (USA). CellTiter-Glo 2.0 was purchased from Life Technologies (USA), Random prime labelling kit (Roche USA). All other chemicals were of analytical grade and were obtained from Biomol (Hamburg, Germany), Merck (USA), Sigma-Aldrich (USA), Roche (USA) or Serva (USA).

3.2 Methods

3.2.1 Quantification of purified proteins using bicinchoninic acid (BCA)

BSA (bovine serum albumin) is used as a standard for protein quantification by BCA method. BCA reagent available in kit form from Pierce (Rockford, IL, USA.) was used for measuring protein concentration. In general, two dilutions of protein samples were taken and each of them was measured in triplicates. Optical density was measured at 562 nm against a blank. A standard curve with 50 μg/ml, 125 μg/ml, 200 μg/ml, and 250 μg/ml of BSA was then drawn from the OD_{562} and fitting equation was derived. The same equation was used to calculate the protein concentration.

3.2.2 Genetic manipulation

Genetic manipulation and recombineering using *M. smegmatis* mc^2 155 to generate the F-ATP synthase mutant with a deletion of amino acids 166 to 179 of the loop of subunit γ (Δγ166-179), were done by Dr. Goran Biuković (National University of Singapore) and described in Hotra, A, *et al.* [167]

3.2.3 Preparation of inverted membrane vesicles from *M. smegmatis*

Preparation of the vesicles is based on a published method by Koul *et al.* [151], and was done with the help of Dr. Goran Biuković and Dr. Priya Ragunathan. Briefly, cells (5 g wet weight) of *M. smegmatis* were resuspended in 10 ml of membrane preparation buffer (50 mM MOPS, 2 mM $MgCl_2$ pH 7.5) containing complete EDTA-free protease inhibitor cocktail (1 tablet/20 ml buffer, Roche-USA) and 1.2 mg/ml lysozyme. The suspension was stirred at RT for 45 minutes and additionally supplemented with 150 µl of 1 M $MgCl_2$ and 25 µl DNAse I (Thermo Fischer, USA) and stirred continually for another 15 minutes at room temperature (RT). All the subsequent steps were perfomed on ice. The cells were broken by four passages through a pre-cooled Model M-110L Microfluidizer processor at 18,000 psi. The suspension containing lysed cells was centrifuged at 4,200 x g for 20 minutes at 4 ^oC. Supernatant containing the membrane fraction was further subjected to ultracentrifugation 4,500 x g at 4 ^oC for 1 h. The supernatant was discarded and precipitated membrane fractions were resuspended in membrane preparation buffer containing 15% glycerol, aliquoted, snap frozen and stored at -80 ^oC. The concentrations of the protein (WT and the $\Delta\gamma_{166\text{-}179}$) in the vesicles, determined by BCA assay were 24.84 µg/µl and 31.79 µg/µl, respectively. The inverted membrane vesicles were stored at -80 °C until used for the experiments.

3.2.4 Assay for ATP-driven proton translocation

ATP-driven proton translocation in IMV's was measured by a decrease of 9-amino-6-chloro-2-methoxyacridine (ACMA) fluorescence using a Cary Eclipse Fluorescence spectrophotometer (Varian Inc., Palo Alto) according to Haagsma et al. [12]. IMV's (0.18 mg per ml) were preincubated at 37 °C in 10 mM HEPES-KOH (pH 7.5), 100 mM KCl, 5 mM $MgCl_2$ containing 2 µM ACMA and a baseline was monitored for 5 min. The reaction was started by

adding 2 mM ATP, or 2 mM NADH. After about 8 min, any proton gradient was collapsed by the addition of 2 μM of the uncoupler SF6847. The excitation and emission wavelengths were 410 nm and 480 nm, respectively.

3.2.5 ATP synthesis assay

ATP synthesis was measured by chemoluminescence: addition of Luciferin to the reaction mixture emits light the in presence of ATP and O_2. The intensity of light, quantified by relative light units, is proportional to the ATP in the solution (Figure 3-1). The assay was performed in the flat-bottom white microtiter 96 well plate (Corning USA). The reaction mix, made in assay buffer (50 mM MOPS, 10 mM $MgCl_2$ pH 7.5) contains 10 μM ADP, 250 μM Pi and 1 mM NADH. Concentrations of Pi were adjusted by addition of 100 mM KH_2PO_4 salt dissolved in the assay buffer. ATP synthesis was started by addition of membrane fractions (inverted vesicles at the final concentration 5 μg/ml). The reaction was incubated at RT for 30 minutes, following which 50 μl of CellTiter-glow reagent was added and incubated for 10 minutes in the dark at RT. Luminescence correlates to the amount of synthesized ATP, and was measured by Tecan plate reader Infinite 200 Pro (Tecan USA), using the following parameters: luminescence, integration time 500 msec, attenuation none, settle time 0. Synthesis of ATP was measured for WT and $\Delta\gamma_{166\text{-}179}$ mutant vesicles. Subsequently, inhibition of the ATP synthesis in the presence of BDQ, DCCD and compound 6 were measured.

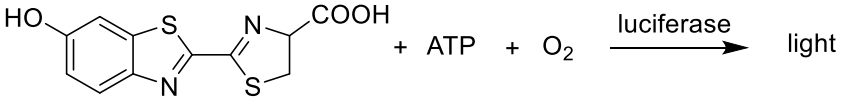

Figure 3-1: Principle of the Luciferin ATP synthesis assay [168] Luciferin emits light in the presence of the ATP and O_2. Emitted light is measured by spectrophotometer as Relative Light Units, which are proportionate to the amount of the ATP in the solution.

3.2.6 ATP hydrolysis assay

ATPase activity of the membranes was assayed in 1 ml of a solution containing 25 mM HEPES (4-(2-hydroxyethyl)-1-piperazineethanesulfonic acid), pH 7.5, 25 mM KCl, 5 mM MgCl2, 5 mM KCN, 2 mM phosphoenolpyruvate, 2 mM ATP, 0,5 mM β-NADH, 30 units of L-lactic dehydrogenase and 30 units of pyruvate kinase. Cuvettes were stored at -80°C.

They were thawed and pre-incubated in a water bath at 37 °C prior to measurement. Hydrolyzed ATP was regenerated by using an equivalent amount of NADH. ATP hydrolysis activity, which inversely corresponds to the slope of the decreasing amount of NADH in the solution was measured by the decreasing absorbance of NADH at a wavelength of 340 nm. The change of the absorbance was measured every 2 seconds for 5 minutes by a GE Healthcare Spectrophotometer Ultrospec 2100 pro with sample cell pre-warmed to 37 °C. Inhibitors were added to the solution before measurement and the vesicles were added at the beginning of the measurement. 10 μg/ml of *Geobacillus stearothermophilus* F-ATP synthase $\alpha_3\beta_3\gamma$ complex, obtained from Dr. Hendrik Sielaff from our team, was used as a control. Measurements of DCCD were done with 20-minute pre-incubation of DCCD with the vesicles in the solution and the absence of ATP, which was added only at the beginning of the measurement. ATPase activity was measured as units per milligram. One unit corresponds to 1 μM of ATP hydrolyzed/min.

3.2.7 Cytotoxicity assay using MTT

MTT assay was carried out as reported elsewhere (Plumb et al., 1989). Briefly, A549 cells were seeded at a density of 6×10^4 cells/well. Test compounds were dissolved in DMSO and the final DMSO concentration for all treatments was synchronized at 0.5% v/v in the growth medium. The treatment duration was 24 h, after which the medium was aspirated from the wells. MTT dye (50 μl of 2 mg/ml in PBS) and growth medium (200 μl) were added per well and incubated at 37°C in the dark for 3 h. The MTT containing medium was then aspirated and DMSO (200 μl) were added to each well. The plates were read at 570 nm using a Tecan M200 plate reader (Tecan Group Ltd., Mannedorf, Switzerland). Cell viability was expressed as the percentage ratio of treated cells normalized over DMSO controls. Median lethal concentrations (LC50) values were obtained from the dose-response curve using Graphpad Prism 6 (Graphpad Software Inc., San Diego, CA).

3.2.8 Solubility assay

Standards and samples for the compounds were prepared from stock DMSO solution diluted into phosphate buffered saline, the pH of the buffer was adjusted to 2.0, 6.0 and 7.4 using 1.0 N HCl or 1.0 N NaOH. Standards for the

calibration curve were diluted to 5, 10, 25, 50 and 100 µM concentration with 5% DMSO. The wavelength (λ_{max}) was determined by a wave scan where absorbance was highest compared to blank, using Tecan pro plate reader and UV-VIS cuvette. Samples were prepared by adding 5 µl of 100 mM 100% DMSO stock solution into 995 µl of buffer, incubated for 24 hours at room temperature and shaken on the orbital shaker at 300 rpm. After the incubation, samples were centrifuged at 13,000 rpm for 15 min. 250 µl of supernatant was collected and absorbance was measured at (λ_{max}). Kinetic solubility was calculated as solubility of the samples interpolated from the calibration curve, analysed in GrapPad 6 (Graphpad Software Inc., San Diego, CA).

3.2.9 Broth and agar MIC

The test compounds and the control drugs were screened against *M. smegmatis* mc^2 155 and *M. bovis* BCG. Initial stock solutions of the test compounds were made in 90% DMSO to a concentration of 10 mM. Ciprofloxacin was used as a positive control and the vehicle DMSO was used as negative control. In the first approach, the compounds were tested on microbial cultures at a fixed concentration of 50 µM. Each of the above strains were cultured at 37 °C in Middlebrook 7H9 broth supplemented with 0.2% glycerol and 10% ADC (Albumin Dextrose Catalase) until logarithmic growth was achieved (OD_{600} 0.4 - 0.6). The test inoculum was obtained by diluting the suspensions to OD_{600} 0.1 to a final volume of 1 ml in the test tubes and were incubated at 37 °C for 24 hours (*M. smeg.*) and 5 days (BCG). Test compounds, which showed no visible growth of bacilli in comparison with the positive and negative controls, were selected as hits.

Broth micro dilution method was used to determine the minimum inhibitory concentration (MIC) of the test compounds. Two-fold serial dilutions of the compounds were made from 200 µM to 0.05 µM. Each concentration was assayed in triplicates. The diluted test inoculum was added to all the wells (final volume 200 µl) in the microplate and was incubated at 37 °C for 24 hours (*M. smeg.*) and 5 days (BCG). The final OD of the cultures in the plate was measured by Tecan Infinite 200 PRO plate reader. The MIC_{50} was defined as the drug concentration that inhibited 50% of the bacterial growth when compared to the growth in the drug-free medium.

3.3 Results

3.3.1 Microbiology testing

The 81 best scoring compounds from the docking studies were obtained from eMolecules (La Jolla, CA, USA) and tested in the growth inhibiton assay on *M. smegmatis*. The most active compound was further characterised.

3.3.1.1 Growth inhibition assay at cut-off concentration 50 μM

With help of Dr. Subhashri Kundu (National University of Singapore), single point assays were performed to identify compounds, which are able to inhibit growth of *M. smegmatis*. The test tubes contained *M. smegmatis*, growth media and tested compounds diluted to the cut off concentration of 50 μM. A hit compound, that would be used for the future studies, should inhibit the bacterial growth at this concentration. Drug free test tubes were used as a negative control, where the growth of *M. smegmatis* could clearly be seen after 24 h incubation. The test tubes with ciprofloxacin, a broad-spectrum antibiotic, served as a positive control. Ciprofloxacin completely inhibited growth of *M. smegmatis*, so the test solution remained clear. Two compounds – compound 6 and compound 2-3 (Figure 3-2) inhibited the growth of *M. smegmatis*. The test tubes containing these two compounds remained as clear as the positive control.

3.3.1.2 Construction of the dose-response curve

A 96 well plate assay was carried out a, in order to calculate half maximal inhibitory concentration (IC_{50}), which is the concentration of the compound required for the 50% growth inhibition. The bacterial growth after 24 hours incubation, measured as bacterial concentration, was determined by absorbance at 600 nm (OD_{600}) with the Tecan plate reader. Data obtained were plotted and a dose-response curve was computed. IC_{50} value was obtained from the graph by finding the concentration, at which the bacterial growth is inhibited by 50%. Compound 6 showed good inhibition with IC_{50} value 11 μM (Figure 3-3A). However, compound 2-3 did not show any inhibition despite having the dilution at concentration of 100 μM, which is higher compared to single point assay (50 μM) where growth inhibition was observed.

(A) **(B)**

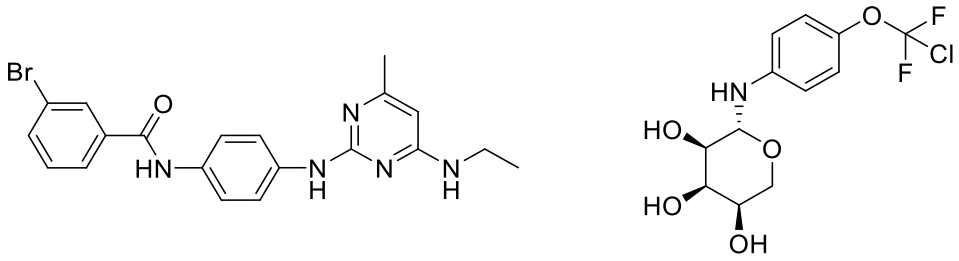

	Compound 6	Compound 2-3
Molecular weight:	426	325
XLogP3-AA	4.7	1.3
H-Bond Donor:	3	4
H-Bond Acceptor:	5	8
Rotatable Bond Count:	6	4

Figure 3-2: Structure of the hit compound 6 (A) and compound 2-3 (B), and overview of the basic characterisation.

3.3.1.3 Further testing of compound 2-3

Because of contradictory results in the case of the compound 2-3 in the single point assay and 96 well plate assay were repeated. No clarification with respect to its inhibitory activity was obtained. Therefore, the tests to find out why compound 2-3 did not show any clear inhibitory activity in the 96 well plate assay were scaled up. This time, the compounds were tested in test tubes with serial dilutions starting from concentration of 1.6 mM. The OD_{600} was measured and a dose response curve was constructed. The IC_{50} calculated from this testing was 150 µM. Previous 96 well plate assays started at the concentration of 100 µM so this could be the reason why no growth inhibition with compound 2-3 was observed. However, it does not explain the inconsistency of the results between first and subsequent testing the single point tests. It is proposed that compound 2-3 might be not stable over time. Because of this, the true concentration in the stock solution might have decreased and would result in a higher calculated IC_{50}. Therefore, it was decided to proceed to further experiments only with compound 6.

3.3.1.4 Testing on *M. bovis* BCG and *Mtb*

After testing the compounds on *M. smegmatis,* the IC_{50} for the *M. bovis* (BCG) was determined, which is more closely related to *Mtb* than *M. smegmatis.* The assay in test tubes was performed with the same procedure as in the single point assay. However, as the generation time of BCG is longer, test tubes had to be incubated for a longer time of five days. Both compounds were tested, but again the inhibitory effect only for compound 6 was present. The resulting IC_{50} was 40 µM, which is higher than in case of *M. smegmatis* but still within the acceptable range (Figure 3-3C).

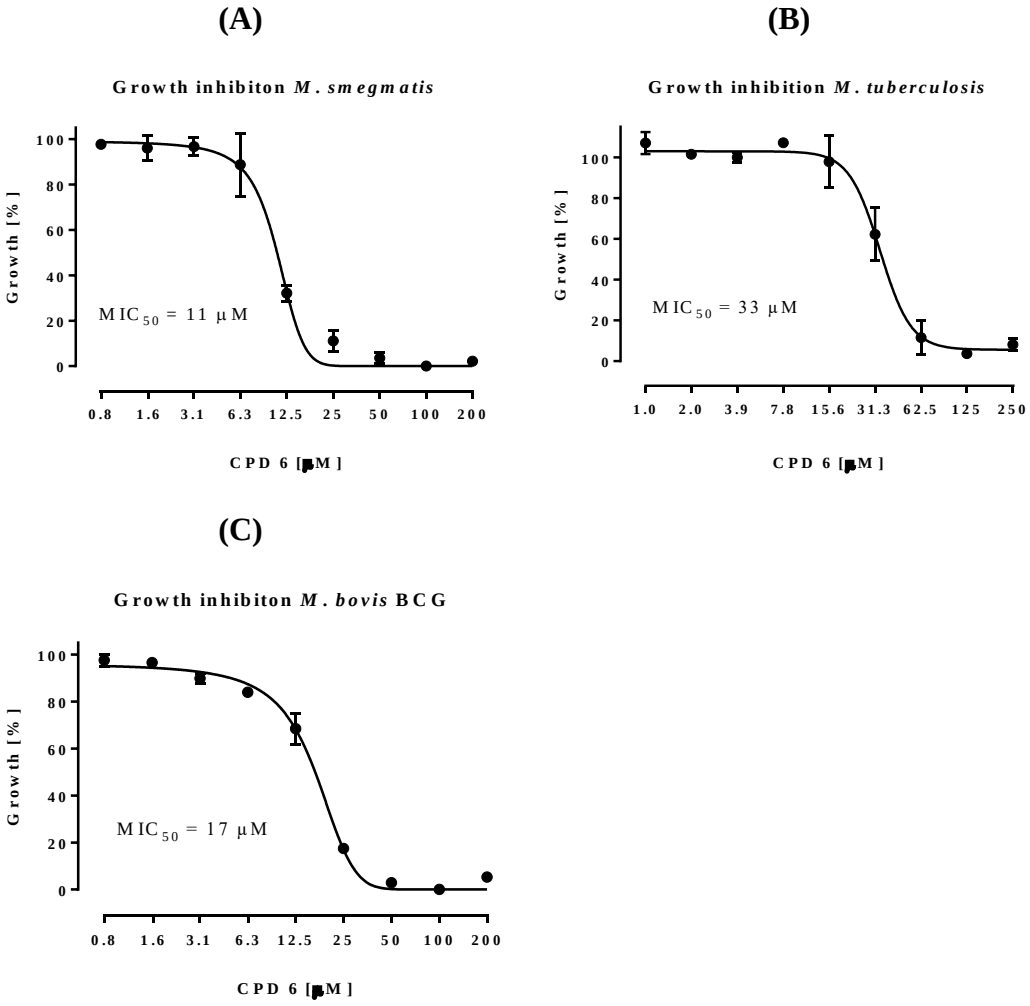

Figure 3-3: Growth inhibition of *M. smegmatis, M bovis BCG* and *Mtb* by cpd 6 with MIC_{50} of 11, 17 and 33 µM, respectively.

As compound 6 exhibited good antimicrobial activity for both *M. smegmatis* and *M. bovis* (BCG), Dr. Pooja Gopal (National University of Singapore) validated its activity on *Mtb.* The cpd 6 activity on *Mtb* stayed in

similar range with moderate MIC_{50} = 33 μM (Figure 3-3B). Early upstream confirmation of the activity against the target, *Mtb*, is essential, as many promising hits might fail at later stage despite having good activity against the model organism such as *M. smegmatis*. Consistent antimicrobial activity is not important only to show that cpd 6 has wide antimycobacterial activity, but also to justify using different strains in later biochemical characterisation. Due to the nature of the experiments, ATP hydrolysis and synthesis experiments were carried out on the inverted membrane vesicles prepared from *M. smegmatis*, however the whole cell ATP synthesis, oxygen consumption rate and additive effect with Q203 were tested using *M. bovis* (BCG). By showing that cpd 6 has similar activity against these different strains, it is justified comparison and correlation between these experiments.

3.3.1.4.1 Mutant selection

A frequently used method to identify the mode of action of antibiotics is to generate spontaneous mutants resistant to the drug. In most cases, bacteria would develop the resistance to antibiotics by these main mechanisms: refluxing the drug from the cell, decreasing cellular uptake of the drug, biochemical modification of the drug to turn in into less active or inactive product and by the target site modification [169]. Resistant strains with altered binding site should have the corresponding mutation in the DNA coding the target protein and would be possible to identify by DNA sequencing, thus providing the insight into the mode of the action of the antibiotic. The binding site of Q203 and BDQ was also postulated by this method. *In vitro* mutants and clinical isolates of BQD resistant strains had, among the others, mutations in the ATPE region, coding for the subunit *c*, which was later genetically and biochemically confirmed [151].

To generate resistant mutants, the optimal combination of the initial inoculum and the compound concentration is needed. As a starting point, and with the help of Mr. Jickky Palmae Sarathy (National University of Singapore), The agar MIC of cpd 6 which was measured, resulting in a value 20 μM. The agar plates were prepared with rising cpd 6 concentrations (1x, 2x, 4x, 8x, 12x, 18x fold MIC) as well as with three different inoculum (10^5, 10^6, 10^7) to select optimal conditions (Table 3-1). The combination of 10^7 inoculum and

concentration of cpd 6 = 80 µM was chosen, as this combination was the first to inhibit growth, as opposed to previous steps 40 µM or 10^6.

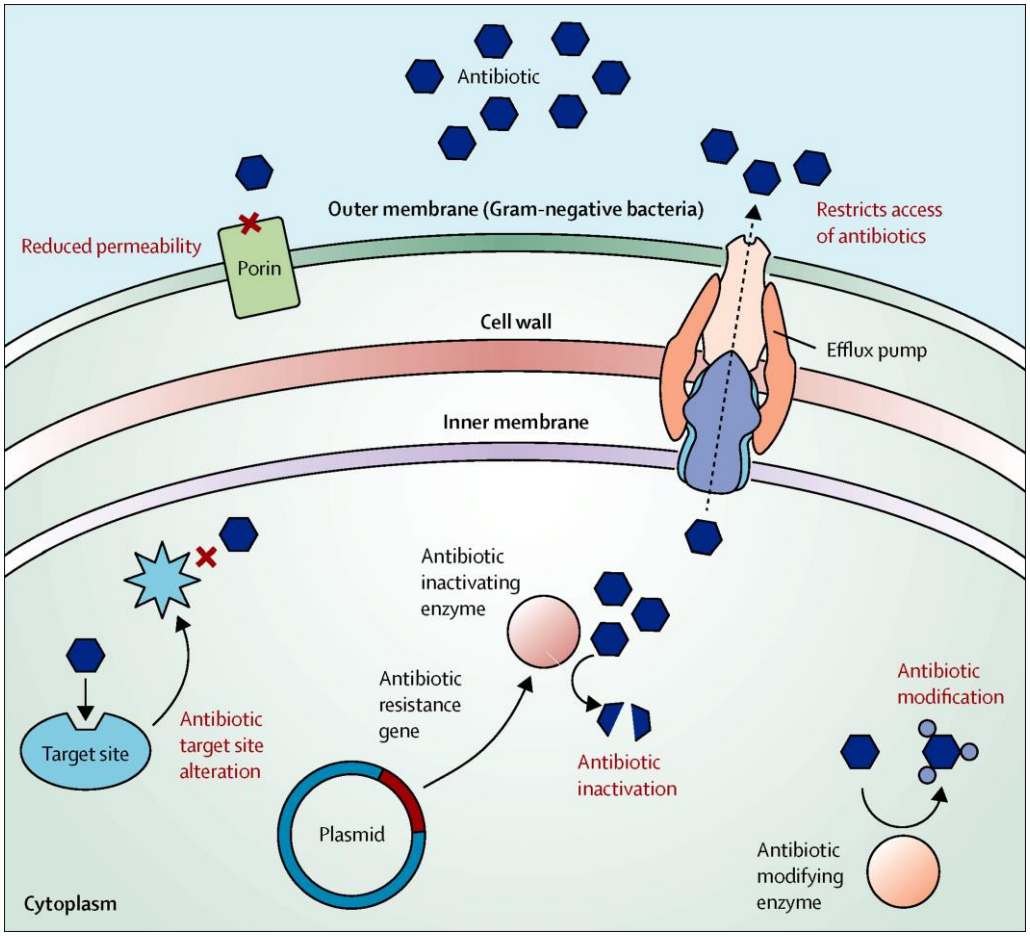

Figure 3-4: Mechanism of antimicrobial resistance. Bacterial resistance to drugs can have different origins: reduced permeability, activation of efflux pumps, antibiotic modification and inactivation or the target protein alteration. [169]

Table 3-1: *In vitro* selection experiment of mutants of *M. smegmatis* resistant to cpd 6.

	cpd6 [µM]					
Inoculum	**20 (1x MIC)**	**40 (2x MIC)**	**80 (4x MIC)**	**160 (8x MIC)**	**240 (12x MIC)**	**360 (18x MIC)**
10^5	No growth	No growth	No growth	No growth	No growth	No growth
10^6	Growth	No growth	No growth	No growth	No growth	No growth
10^7	Growth	Growth	No growth	No growth	No growth	No growth

However, after two weeks, no colony growth was observed at this combination Therefore, the concentration of cpd 6 was lowered to 70 μM while keeping the constant inoculum 10^6. After two weeks incubation with the new conditions, 11 colonies were obtained. To confirm resistance to cpd 6, colonies were restreaked again on 70 μM plates. 10 colonies were confirmed, with resulting low mutation rate ($10/(40 \times 10^7) = 2.5 \times 10^{-8}$). This mutation rate is comparable with mutation rate of BDQ with rate of 2×10^{-8} at 4 times MIC, and 1×10^8 at 8 times MIC for *M. smegmatis* (5×10^{-7} at 4 times MIC and 5×10^{-8} at 8 times MIC, for *Mtb*) [170]. Broth and agar MIC_{50} was determined and compared with WT (Table 3-2). For most of the colonies the resistance is low, except moderate increase for colony 06 (broth MIC_{50} = 23.9 μM and agar MIC_{50} = 60 μM) and colony 11 (broth MIC_{50} = 13.1 μM and agar MIC_{50} = 60 μM). This is, however, still only a small increase in MIC_{50} when compared to mutants resistant to derivates of Q203 which were reported to have several orders of magnitude increase in MIC_{50} [145] as well as mutants resistant to BDQ with MIC_{90} shift from 0.003 to 3.0 μg/ml (1000—fold increase) [170]. All the cpd 6 resistant colonies were screened for mutation in the F-ATP synthase operon but no mutation was found. Low mutation rate with the narrow mutant selection window might indicate either the target protein is essential and only nonspecific resistance was developed or the compound has affinity to two independent targets, which could be the reason why no mutations in the ATP synthase operon were observed [171].

Table 3-2: Broth and agar MIC_{50} of the resistant mutants.

	wt	**01**	**03**	**04**	**05**	**06**	**07**	**08**	**09**	**10**	**11**
Broth MIC_{50} [μM]	8.5	7.6	8.3	6.8	6.5	23.9	7.4	11.9	7.9	9.8	13.1
Agar MIC (fold increase)	1x	2x	2x	2x	2x	3x	2x	2.5x	2x	2x	3x

3.3.2 Biochemistry

Since the compound activity assays were done on the whole cells, the growth inhibition alone did not give us any insight into the cpd 6 mode of action. The F-ATP synthase as the target of the compound needed to be confirmed. Therefore, the activity of cpd 6 in various biochemical assays was investigated.

3.3.2.1 Enzymatic assays on the inverted membrane vesicles

Cpd 6 was designed to bind to the F-ATP synthase, and by doing so, to block ATP synthesis and hydrolysis. To investigate this putative mode of action, an assay specific to the F-ATP synthase had to be established. Since the F-ATP synthase needs a proton motive force to synthesise ATP and the complex of transmembrane F_O part with cytosolic F_1 part has not been isolated and purified yet, the assay using the IMVs was selected, which were formed spontaneously by disrupting the cell membrane in the French press or in the microfluidizer. Series of washings and centrifugations ensures that these vesicles contain mainly membrane embedded proteins such as respiratory chain proteins.

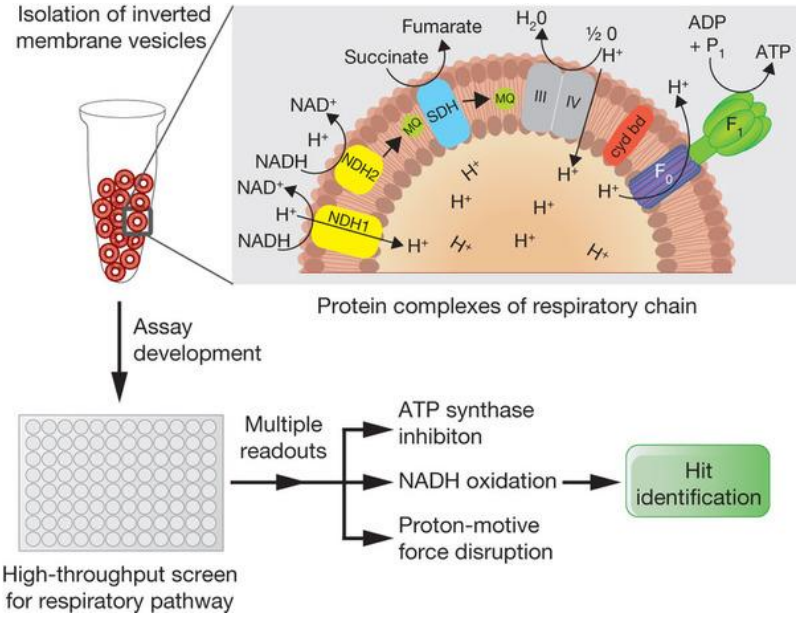

Figure 3-5: Scheme of the assay on the inverted membrane vesicles and the composition of the IMVs [102]. Membranes contain all the respiratory chain proteins and in the presence of NADH they are able to set up a proton-motive gradient and synthetize ATP. Production of ATP can by inhibited directly by blocking ATP synthase, or by upstream inhibition of the respiratory chain *e.g.* disrupting the proton-motive force and inhibiting of NADH oxidation.

The respiratory chain enzymes, when supplemented with NADH, are able to generate an electrochemical gradient inside the vesicles. Consequently,

this proton-motive force is used by F-ATP synthase to synthesize ATP from ADP and Pi. Vesicles can be characterised by series of specific respiratory chain inhibitors so that the effect of the compounds on the individual enzymes can be observed (Figure 3-5). Therefore, IMVs represent an ideal system for ATP synthase testing and characterisation. Furthermore, the same method was used as one of the methods to validate ATP synthesis as BDQs mode of action [172].

3.3.2.1.1 ATP hydrolysis assay

Previously, Haagsma *et al.* concluded that the F-ATP synthase of *M. smegmatis* would not be able to hydrolyse ATP. However, this was observed only indirectly by measuring ATP hydrolysis driven proton pumping [173]. The ATP hydrolysis does not necessarily have to be linked to the proton pumping. In case of uncoupling of the ATP hydrolysis from proton pumping, the sole measurement of the change in proton gradient is not sufficient to claim that F-ATP synthase of *M. smegmatis* is not able to hydrolyse ATP. In our assay, however, also indirectly, the actual hydrolysis of ATP is measured. Hydrolysed ATP is regenerated back by pyruvate kinase which transfers phosphate from phosphoenolpyruvate to ADP, producing ATP and pyruvate. Subsequently, pyruvate is converted to lactate by lactate dehydrogenase while NADH is oxidised to NAD^+. ATP hydrolysis is thus directly linked to the oxidation of NADH (Figure 3-6A). These two different redox states have different absorbance profiles. Both absorb strongly at 260 nm because of the adenine moiety in present the structure, however, only NADH which has the reduced form of nicotinamide is absorbing at 340 nm Figure 3-6B). Therefore, oxidation of NADH can be directly measured by UV spectrometer. In this hydrolysis assay, the rate (slope) of the NADH consumption after the addition of the vesicles is measured (Figure 3-6C) and the hydrolysis rate is calculated.

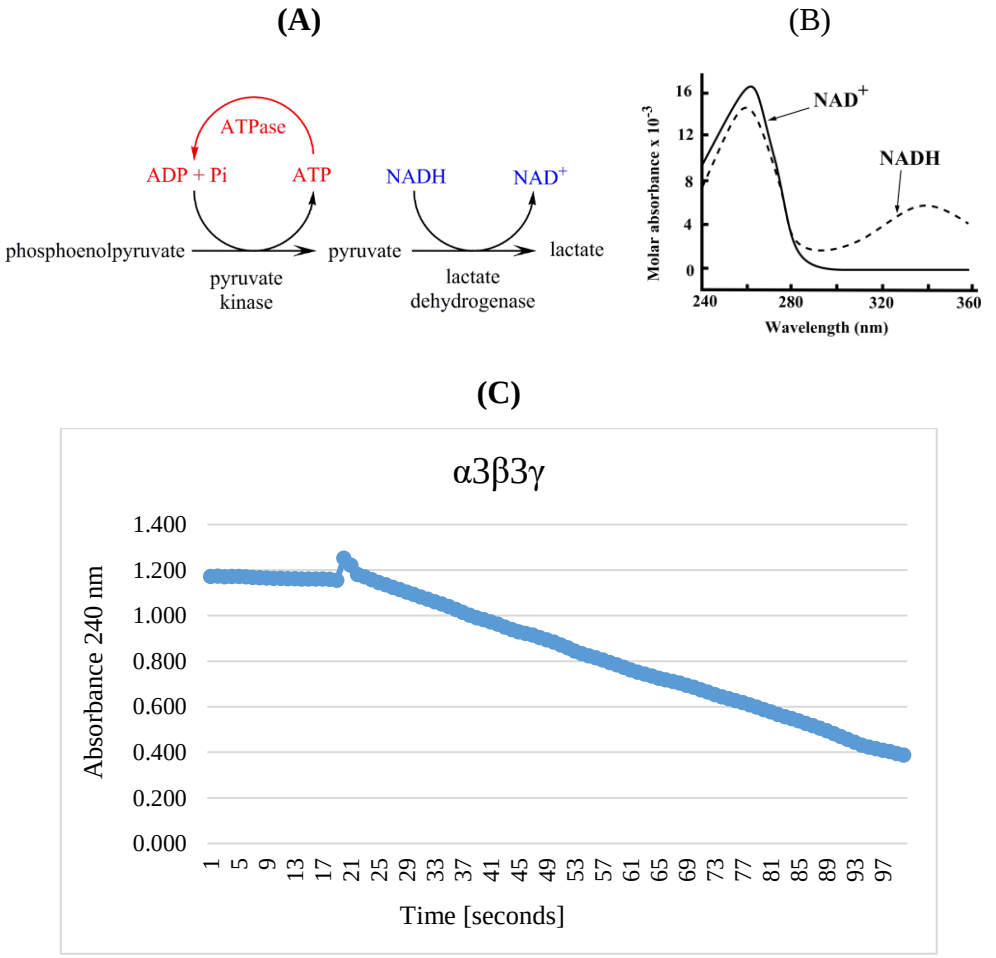

Figure 3-6: The principle of the ATP hydrolysis assay. (A) Hydrolyzed ATP is regenerated by pyruvate kinase, producing pyruvate, which in turn is transformed into lactate. During this reaction NADH is oxidized to NAD^+ and it is proportionally linked to the ATP hydrolysis (A). NADH and NAD^+ have different absorption profile, therefore the consumption of NADH can be measured by drop in absorbance at 340 nm (B). Hydrolysis starts after addition of the vesicles or the protein (in this case of the control experiment using *Bacillus subtilis* F-ATP synthase $\alpha_3\beta_3\gamma$ complex) into the buffer containing enzymes, NADH and ATP (C). The slope of the decrease of the NADH absorbance is measured and the rate of hydrolysis is calculated.

IMVs contain the type II NADH dehydrogenase (NDH-2), which would competitively oxidize NADH. Therefore, the NDH2 inhibitor thioridazine (80 µM [174]) has been added to the assay. In *M. smegmatis* NDH-2 represents 95% of total NADH-oxidation [175]. As later demonstrated in Figure 3-8A-B, IMVs of WT *M. smegmatis* revealed an ATP hydrolysis activity of about 36 nmol/min·mg total protein. To confirm, that hydrolysis is indeed catalyzed by the *M. smegmatis* F-ATP synthase, the effect of various F-type ATP synthase

inhibitors like resveratrol, 4-chloro-7-nitrobenzofurazan (NBD-Cl), and BDQ, which affect *M. smegmatis* mc^2 155 growth, as well as quercetin and efrapeptin C, were tested. Resveratrol, which inhibits the rotation of F_1F_O ATP synthase by binding to the interface of the α and β subunits and the C-terminus of subunit γ [176], reduced the ATP hydrolytic activity of the *M. smegmatis* IMV's to 22% (100 μM of resveratrol). A concentration dependent measurement with resveratrol resulted in an IC_{50}-value of about 50 μM (Figure 3-7A), which is comparable with those reported for the purified bovine mitochondrial F_1-ATPase (6.4 μM; [177]). Quercetin, a close analog of resveratrol with the same binding site inside the F-ATP synthase [177], reduced ATP hydrolysis to 44% (100 μM of quercetin; Figure 3-7B). In addition, an IC_{50} of 75 μM for quercetin could be determined. By comparison, BDQ showed inhibition of ATPase activity with an IC_{50} comparable to quercetin (75 μM, Figure 3-7C). BDQ has been described to inhibit ATP synthesis by binding with its dimethylamino moiety to residue E65 and sitting with its quinoline moiety on the F69 platform of the *c*-ring [178]. In addition, as revealed by IMV and whole cell analyses of *M. smegmatis* mc^2 155, BDQ has no effect on the membrane potential (Δψ), which may suggest that the charge across the membrane is maintained through as yet undetermined processes during BDQ challenge [179]. The authors proposed a mechanism of uncoupling, which involves the binding of BDQ to the *c* subunit and perturbing the *a*-*c* subunit interface, allowing an uncontrolled proton leak uncoupled from ATP synthesis. Like the inhibitor DCCD, which binds to the catalytic β subunits of F_1 [180] and the *c* subunit of F_O [181], a second possible binding-site for BDQ has been proposed to be in the interface of the ε subunit and the *c*-ring, where the drug would hinder rotation of the *c*-ring relative to the γε-powerstroke in a wedge-like fashion [147]. As ATP hydrolysis is catalysed in the F_1 domain the present data imply that BDQ inhibits not only ATP synthesis (IC_{50} = 4.5 nM, see below) but also ATP cleavage (IC_{50} around 90 μM) and that this effect may occur via binding to a second binding site inside the F-ATP synthase complex.

Another potent inhibitor, 4-Chloro-7-nitrobenzofurazan (NBD-Cl), binds covalently to tyrosine residue 331 of the so-called nucleotide empty β subunit (β_E) [182], and is also allocated in the proximity of the central stalk. Like resveratrol, NBD-Cl inhibited effective ATP hydrolysis with an IC_{50} value of

around 100 µM (Figure 3-7D). While most of the inhibitors showed strong inhibition of ATP hydrolysis, efrapeptin C with a binding site in F-ATP synthase similar to those for resveratrol and quercetin [183] (Figure 3-7E) exhibited a reduction of 20% ATPase activity (100 µM efrapeptin C).

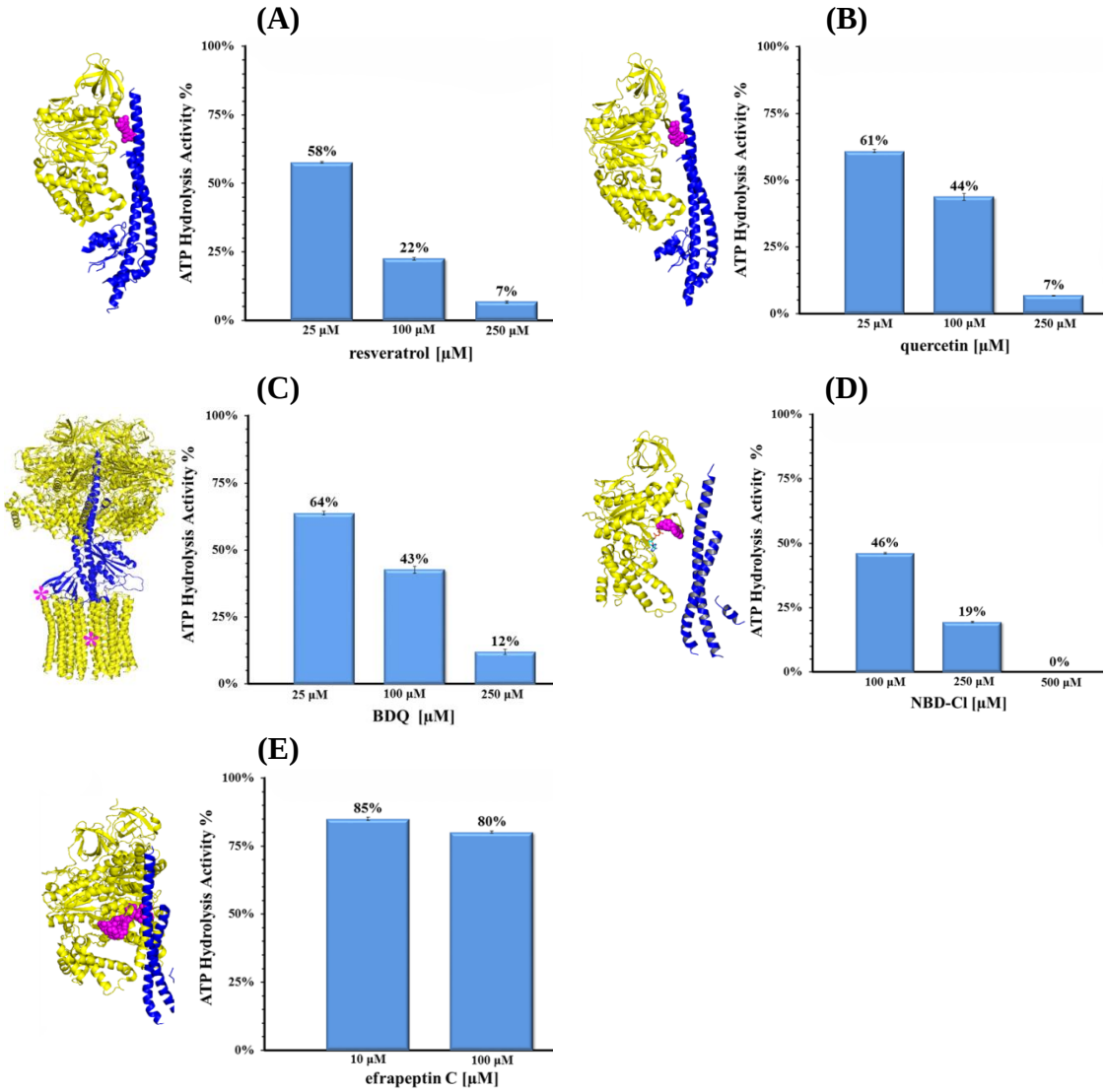

Figure 3-7: ATP hydrolysis and inhibition of wild type *M. smegmatis* IMV's. Concentration dependent inhibitory effects on the ATPase activity of IMV's of WT *M. smegmatis* by resveratrol (*A*), quercetin (*B*), BDQ (*C*), 4-Chloro-7-nitrobenzofurazan (NBD-Cl) (*D*), and efrapeptin C (*E*). The inhibitors (*magenta*) and their respective binding sites insight the crystal structure of F_1 or F-ATP synthase are shown.

3.3.2.2 The γ166-179 loop as potential drug target

Mycobacterium has an extra loop of 13 amino acids (165-178), which is predicted to be located near the interface of the γ subunit and the *c*-ring [149]. This loop, which is unique to the *Mycobacterium* can be a highly specific drug target. The effect of the $\gamma_{166\text{-}179}$ loop on the ATP synthesis and ATP hydrolysis were tested on *M. smegmatis* inside-out vesicles with a deletion of the $\gamma_{166\text{-}179}$ loop ($\Delta\gamma_{166\text{-}179}$). The $\Delta\gamma_{166\text{-}179}$ mutant of *M. smegmatis* was generated by Dr. Goran Biuković (National University of Singapore).

After characterization of the WT IMV's, the effect of the loop-deletion of the *M. smegmatis* $\Delta\gamma_{166\text{-}179}$ mutant protein on ATP hydrolysis was investigated. As revealed in Figure 3-8A-B, the hydrolysis rate of the Δγ166-179 mutant including IMVs increased by about 34% (55 nmol/min·mg total protein) compared to the vesicles of the wild type complex, which shows that the mutation did alter ATPase activity.

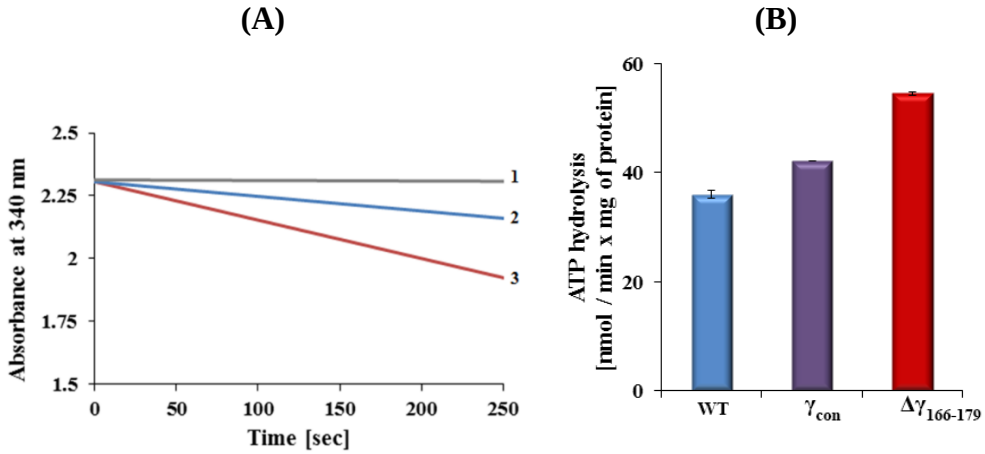

Figure 3-8: Comparing ATP hydrolysis for the wild type and the $\Delta\gamma_{166\text{-}179}$ mutant. (A) Continuous ATPase activity of WT and the *M. smegmatis* $\Delta\gamma_{166\text{–}179}$ mutant protein measured at 2 mM MgATP. Line 1 (gray) represents IMVs containing WT protein in the presence of the NDH-2 inhibitor thioridazine (80 µM) without MgATP, showing the inhibitory effect of thioridazine. Lines 2 and 3 (blue and red) represent IMVs containing WT and $\Delta\gamma_{166\text{–}179}$ mutant protein in the presence of thioridazine and MgATP. (B) Specific ATPase activity of WT F-ATP synthase, the γcon strain (complementation construct *M. smegmatis* ΔatpG x pMV262atpG) and $\Delta\gamma_{166\text{–}179}$ mutant protein. Values are means SD based on the three independent determinations.

To confirm that the observed difference in ATP hydrolysis of the WT and $\Delta\gamma_{166\text{-}179}$ mutant IMVs is indeed caused by the loop deletion, the Δ*atpG* mutant strain was complemented with the WT copy of the *atpG* gene. This was

done by overexpression of *atpG* under the strong constitutive promoter hsp60 on plasmid pMV262 [184] transformed into *M. smegmatis ΔatpG*(166-179), harbouring the gene Δ*atpG* coding for Δγ (see [167]). As revealed in Figure 3-8B, the hydrolysis rate of IMVs derived from the constitutive expression system described above decreased (42.2 nmol/min·mg total protein) when compared to the one of the $\Delta\gamma_{166\text{-}179}$ mutant, reflecting that the complementation was successful and that the loop-deletion caused the observed increase of ATPase activity of the $\Delta\gamma_{166\text{-}179}$ mutant strain.

3.3.2.2.1 Proton-translocation in the inverted membrane vesicles

In order to determine whether ATP hydrolysis is coupled with proton-pumping, the proton-translocation in IMV's of *M. smegmatis* was measured in the presence of the fluorescent dye 9-amino-6-chloro-2-methoxyacridine (ACMA) by Dr. Priya Ragunathan. In the presence of H^+, fluorescence of ACMA is quenched. As shown in Figure 3-9A, adding the substrate ATP to the IMV containing assay resulted in no further drop of fluorescence, besides the typical slight ATP-caused quenching signal. This indicated that the F-ATP synthase of *M. smegmatis* does not show an ATP hydrolysis driven proton transport, which is in line with previous findings. These studies demonstrated that irrespective of the Mg:ATP ratio or the pH value (pH 5.5–8.0) nor ATPase-driven proton pumping could be detected in slow or fast growing mycobacteria [173]. To exclude the leakiness of the IMV's, NADH has been added to the assay, proton gradient was established and accumulation of H^+ inside the vesicles caused a significant quenching of ACMA, generated by the respiratory chain complexes (Figure 3-9B). Addition of the uncoupler SF6847 revealed the associated increase in fluorescence, confirming that the IMV's are intact.

In comparison, when ATP was added to IMV's including the *M. smegmatis* $\Delta\gamma_{166\text{-}179}$ mutant protein proton-conduction occurred, resulting in a quenching of about 61%. This result confirms also that the ATPase activity detected above is of intact IMV's with complete F_1F_O ATP synthase complexes. Afterwards, SF6847 resolved the generated proton pumping shown by an increase in fluorescence (Figure 3-9B). Furthermore, NADH-driven proton pumping of the IMV's of the *M. smegmatis* $\Delta\gamma_{166\text{-}179}$ mutant protein revealed a quenching result similar to that for the wild-type IMV's, indicating that the

observed change in ATP-driven proton pumping of the IMV's of the *M. smegmatis* $\Delta\gamma_{166\text{-}179}$ mutant is caused by the loop deletion in the F-ATP synthase mutant form. Furthermore, the data show for the first time that the additional 13 amino acid loop at the bottom of the globular domain of the mycobacteria γ subunit, proposed to be in the vicinity of the polar loop residues of the *c*-ring, is at least one critical structural element preventing ATP-driven H^+-pumping of mycobacterial F-ATP synthases.

The data above and revealed recently [173] demonstrate that although at a relatively low level, ATP becomes hydrolyzed by the fast growing *M. smegmatis* F-ATP synthase without coupled proton-pumping. Furthermore, slow growing mycobacteria like *M. bovis* BCG show neither detectable ATPase activity [149] nor H^+-pumping translocation of their F-ATP synthase [149]. The question arises, why does the fast-growing *M. smegmatis* F-ATP synthase hydrolyse ATP to ADP although it does not pump protons? As previously discussed by Zharova and Vinogradov [185] in studies on F-ATP synthases of tightly coupled vesicles of *Paracoccus denitrificans*, two alternative mechanisms of respiratory control have been described so far. A first mechanism invokes the so-called "thermodynamic" control [186]. In this model, an increase in the respiratory activity by ADP is considered as a change in the ATP/ADP ratio that results in activation of redox reactions to restore the disturbed equilibrium. A second model suggests that respiration is kinetically controlled by ADP via either the adenine nucleotide translocase (in case of mitochondria) or some intrinsic mechanisms of the F-ATP synthase [187]. Since the essence of the respiratory control is that ADP accelerates respiration, ADP generated by the *M. smegmatis* F-ATP synthase may actually stimulate the respiratory chain, leading to the formation of ATP. This may be one aspect enabling this mycobacterium to grow faster compared to its counterpart *M. bovis* BCG, whose F-ATP synthase does not show detectable ATP hydrolysis.

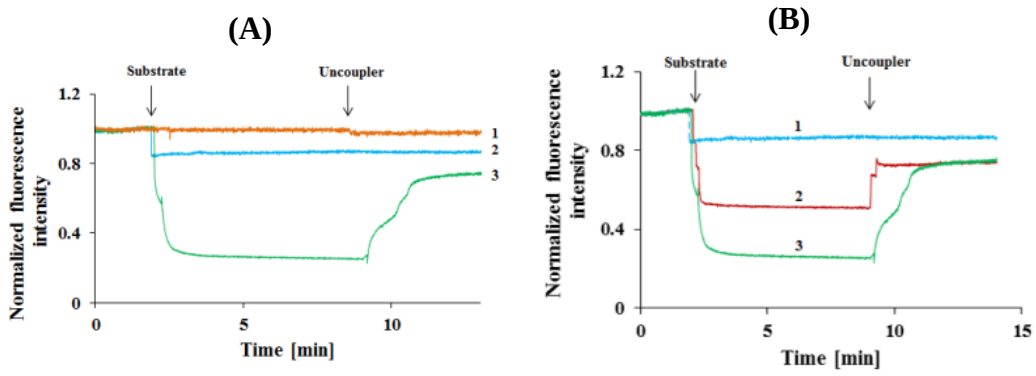

Figure 3-9: Substrate driven proton-pumping in IMV's. *M. smegmatis* wild type (*A*) and Δγ166-179 mutant (*B*) membrane vesicles were diluted to 0.18 mg/ml in buffer containing 10 mM HEPES-KOH (pH 7.5), 100 mM KCl, 5 mM $MgCl_2$ and 2 µM ACMA. Fluorescence quenching of ACMA was studied after the addition of a substrate (2 mM ATP (profile 2) or 2 mM NADH (profile 3). The uncoupler (SF6847) was added at the indicated time point to collapse the proton gradient. In the control experiment, buffer was added in place for substrate (profile 1in (*A*)). Fluorescence quenching of ACMA in wild type IMV's by ATP (profile 2 and 1 in (*A*) and (*B*), respectively) is shown along with that of the Δγ166-179 mutant form for better comparison.

3.3.2.2.2 ATP synthesis activity of $\Delta\gamma_{166\text{-}179}$ vesicles

The ATP synthesis activity of the wild type and the $\Delta\gamma_{166\text{-}179}$ mutant vesicles were measured. The amount of ATP synthetized by $\Delta\gamma_{166\text{-}179}$ was 5.83 picomoles, which was only about the half of that of wild type (11.32 picomoles) at the same concentration of vesicles (Figure 3-10A). The effect of BDQ on ATP synthesis of the WT and $\Delta\gamma_{166\text{-}179}$ mutant were evaluated for a wide range of BDQ concentrations from 5 µM to 0.04 nM. The maximum ATP synthase activity of the $\Delta\gamma_{166\text{-}179}$ vesicles was below 2.5 picomoles when compared to 4 picomoles synthetized by the wild type enzyme. In comparison to the WT enzyme, ATP synthesis by the $\Delta\gamma_{166\text{-}179}$ mutant was overall reduced for all concentrations of BDQ. Interestingly, the inhibition of the $\Delta\gamma_{166\text{-}179}$ (Figure 3-10D) starts at the lower concentrations of BDQ (2.5 nM) than in the WT (9 nM) (Figure 3-10C).

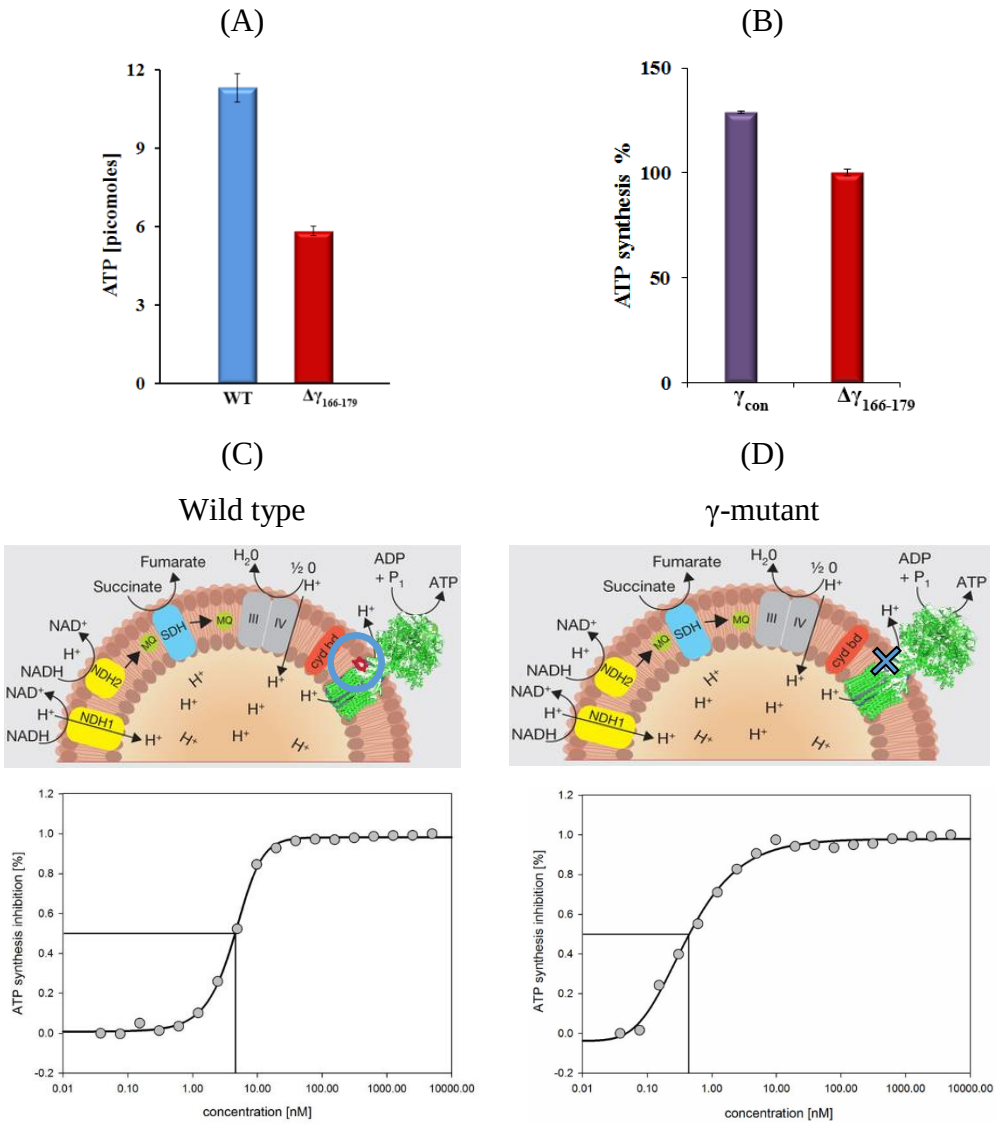

Figure 3-10: ATP synthesis of the IMVs. ATP synthesis of the $\Delta\gamma_{166\text{-}179}$ mutant IMVs (5.8 nmol) is only half compared to WT IMVs (11.3 nmol) (A), The ATP synthesis is partially restored in the complemented strain (B), confirming that the drop of ATP synthesis was caused by deletion of the γ-loop. The IC_{50} of BQD is lower 10-fold lower in the $\Delta\gamma_{166\text{-}179}$ mutant (D) compared to the WT (C).

To demonstrate an effect of the γ-loop deletion in ATP synthesis the ATP production of the WT- and the $\Delta\gamma_{166\text{-}179}$ mutant containing vesicles were measured. The WT F-ATP synthase of the *M. smegmatis* IMVs showed an ATP synthesis formation of 11.3 nmol. In comparison, 5.8 nmol have been synthesized by IMV's of the $\Delta\gamma_{166\text{-}179}$ mutant protein and therefore 54% of the WT protein (Figure 3-10A). As revealed in Figure 3-10B, the addition of inhibitor BDQ reduced ATP synthesis. To determine the half-maximal inhibitory concentration, the BDQ concentration was varied from 0.04 nM to 5 µM. The

IC_{50} value of about 4.5 nM determined is in line with those reported recently for *M. smegmatis* (2.5 – 12.9 nM [28,29] and *M. phlei* (20 – 25 nM, [8]). In comparison, although the $\Delta\gamma_{166\text{-}179}$ mutant membrane vesicles showed a lower overall ATP synthesis formation, the determined IC_{50} value of BDQ is about 0.4 nM and therefore lower than for the WT protein (Figure 3-10C).

3.3.2.2.3 Characterisation of compound 6

With the ATP hydrolysis and ATP synthesis assay established, and demonstrated the importance of the γ-loop, the hit compound 6 could be tested against its putative target, the F-ATP synthase. Furthermore, the combination with BDQ and Q203 was tested to investigate the additive effect.

3.3.2.2.4 Effect of cpd 6 on ATP synthesis and hydrolysis

Cpd 6 inhibited ATP synthesis with good IC_{50} = 0.3 µM, indicating that cpd 6 is most probably acting by inhibiting respiratory chain proteins. The ATP hydrolysis inhibition of cpd 6 at 100 µM (52%) was comparable with BDQ (43%), quercetin (44%) and NBD-Cl (46%) (Figure 3-12). Since it was previously shown that hydrolysis of the vesicles is catalyzed by the mycobacterial F-ATP synthase we can conclude that compound 6 is inhibiting the ATPase activity. Therefore, compound 6 is not only inhibiting ATP synthesis but also ATP hydrolysis, suggesting that cpd 6 might be targeting the ATP synthase. The difference in the inhibitory concentration of hydrolysis and synthesis is due to the different concentration of vesicles used for the assays, 200 µg/ml in case of hydrolysis versus 5 µg/ml for the synthesis.

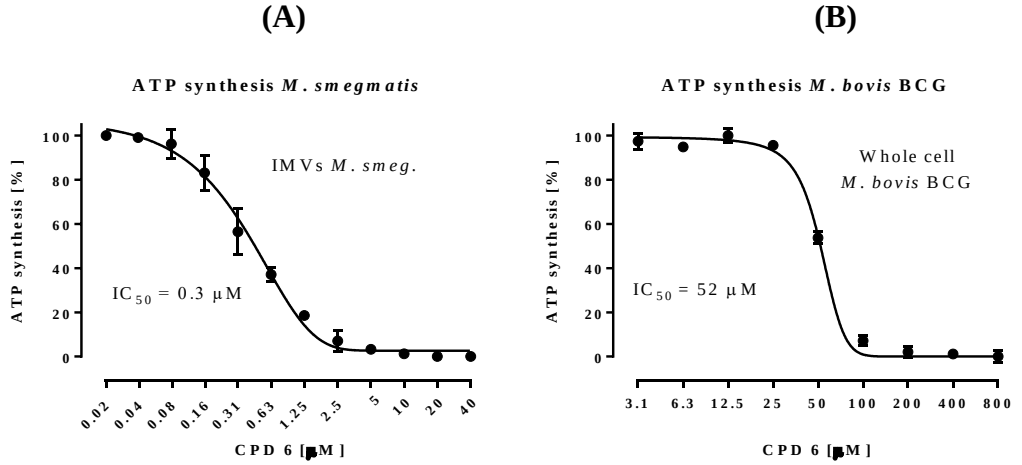

Figure 3-11: Inhibition of ATP synthesis in *M. smegmatis* IMVs and in whole cells.

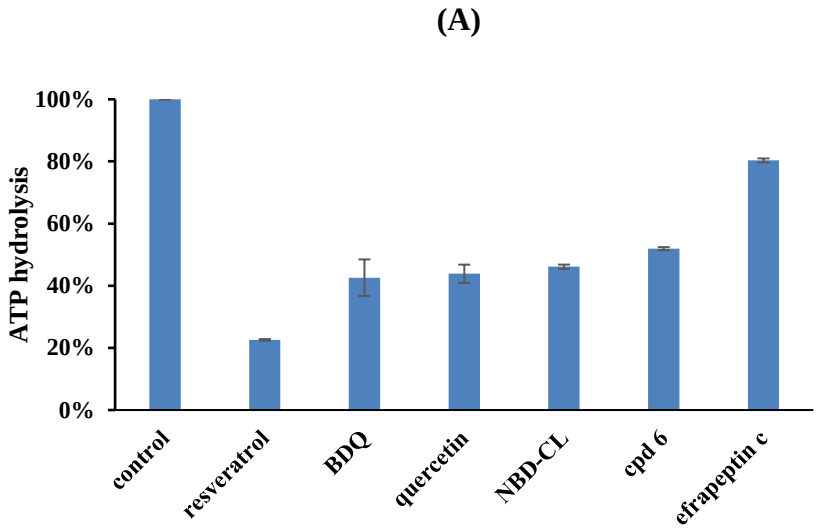

Figure 3-12: Cpd 6 compared to several known inhibitors of F_1F_O ATP synthase at a concentration of 100 µM showed good inhibition of 52%, similar to 4-chloro-7-nitrobenzofurazan (NBD-Cl) - 46%, quercetin - 44% and BDQ - 43%.

3.3.2.2.5 ATP synthesis inhibition by cpd 6 on $\Delta\gamma_{166\text{-}179}$ mutant

The ATP synthesis inhibition by cpd 6 on vesicles from *M. smegmatis* WT was compared to the vesicles from $\Delta\gamma_{166\text{-}179}$ mutant (Figure 3-13). Despite our expectation, based on the design of the cpd 6 to bind in the proximity of the γ-loop, the inhibition curves have a very similar profile, with IC_{50} around 1.25 µM, and achieving complete ATP inhibition at 10 µM. However, as discussed above in the modelling studies, all the docked ligands had preference to bind to the globular base of γ subunit, where the γ-loop did not provide interaction with the ligands, but served more as a structural feature forming a binding cavity.

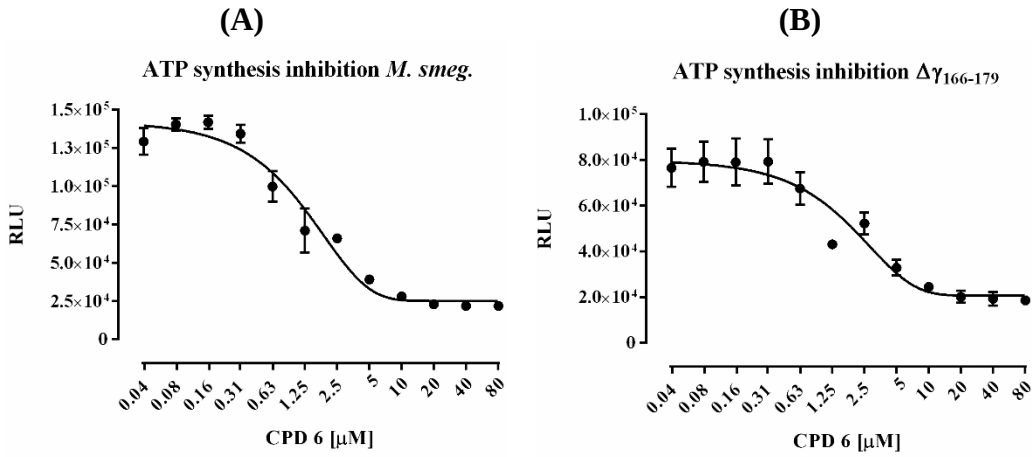

Figure 3-13: Inhibition of the ATP synthesis by cpd 6 on WT *M. smegmatis* compared to the $\Delta\gamma_{166\text{-}179}$ mutant.

3.3.2.2.6 Additive effect on growth inhibition

Based on the similar activity profile of the cpd 6 and BDQ, the combination of the drugs was tested. To assess an additive effect of cpd 6 and BDQ, the effect drug combinations on the growth inhibition of *M. smegmatis* was examined (Figure 3-14). BDQ inhibited the growth at 31.25 nM, however if used in combination with 6.25 µM of cpd 6, the inhibition was achieved 7.81 nM of BDQ. With rising concentrations of cpd 6, the IC_{50} of BDQ dropped from 9.6 nM (no cpd 6), to 4.2 nM (0.78 µM of cpd 6) and 2.5 nM (3.13 µM of cpd 6), and finally to complete inhibition at 12.5 µM of cpd 6. These data confirm the additive effect of the drug combination.

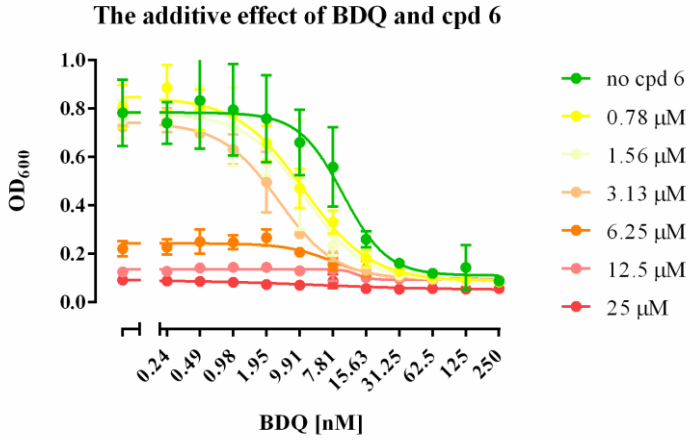

Figure 3-14: The additive effect of BDQ and cpd 6 on growth inhibition of *M. smegmatis*. Dose-response curve of the BDQ is shifting toward lower concentration of BDQ after addition of the cpd 6, further supporting the hypothesis that they target the same cellular mechanism.

3.3.2.2.7 Whole cell ATP synthesis

After confirming the additive effect on the growth inhibition, additive effect on the putative mechanism of action of cpd 6, the ATP synthesis was examined. In the whole cell ATP synthesis assay, performed with help of Dr. Nitin Kalia (LKC Medicine, NTU), an additive effect of BDQ and cpd 6 was observed. At a concentration of 200 nM BDQ alone inhibited ATP synthesis from $3.7x10^4$ RLU to $8x10^3$ RLU. However, in the presence of 37.5 µM of cpd 6 only 12.5 nM of BDQ were needed to achieve similar inhibition ($6.5x10^3$ RLU). Furthermore, IC_{50} of BDQ was significantly lowered from 42 nM for BDQ alone to 2.36 nM in combination with cpd 6 at 75 µM (Figure 3-15). Shift of the dose response curves towards lower concentrations might indicate that BDQ and cpd

6 have a common target. On the other hand, the combination of cpd 6 and Q203, while still additive, is not significantly affecting the Q203 IC_{50} values. Even though Q203 reached the maximum inhibition at 12.5 nM ($1.6x10^4$ RLU), combination with 75 μM of cpd 6 resulted in further ATP synthesis inhibition up to ($3.5x10^3$ RLU). It is hypothesised that although Q203 fully inhibited the Cyt-*bc*$_1$, the proton gradient was still maintained by Cyt-*bd*, resulting in lower, but still present, synthesis of ATP. Downstream inhibition of the ATP synthase by cpd 6 could explain the further complete ATP synthesis inhibition (Figure 3-16). This was confirmed by a Cyt-*bd* knockout mutant from Prof. Kevin Pethe's lab (LKC Medicine, NTU), where no further inhibition of ATP synthesis was observed after the addition of cpd 6. At 12.5 nM of Q203 alone and with combination of 75 μM of cpd 6, the ATP levels are the same ($3.9x10^3$ RLU). In the absence of Cyt-*bd*, the proton gradient is maintained only by Cyt-*bc*$_1$. Therefore, maintenance of the proton gradient of the Cyt-*bd* knockout is fully inhibited by Q203, and it is not sufficient for the ATP synthesis.

(A)

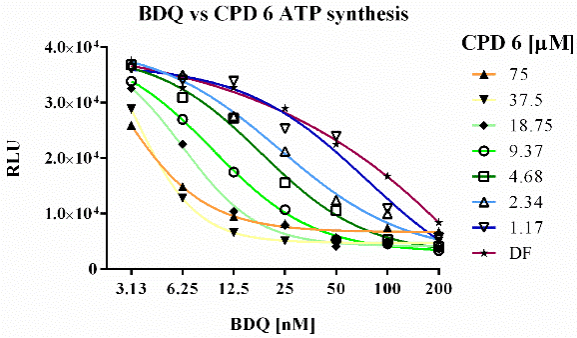

(B)

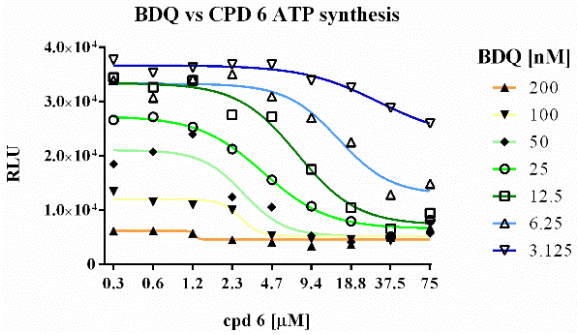

(C)

BDQ IC_{50} = 42 nM

cpd 6 [µM]	BDQ IC_{50} [nM]
0.29	49.83
0.58	60.92
1.17	76.36
2.34	23.33
4.68	18.20
9.37	9.41
18.75	6.25
37.50	3.16
75.00	2.36

(D)

cpd 6 IC_{50} = 52.5 µM

BDQ [nM]	cpd 6 IC_{50} [µM]
3.125	30.02
6.25	15.1
12.5	7.352
25	4.034
50	2.85

Figure 3-15: Whole cell checkerboard ATP synthesis assay with combination of BDQ and cpd 6. ATP synthesis inhibition curve of BDQ significantly shifts to the lower concentration with increasing concentration of cpd 6 (A). BDQ alone starts inhibiting the ATP synthesis from 100 nM. Same effect was observed at 6.25 nM of BDQ with addition of 75 µM of cpd 6. Additive effect of cpd 6 was starting as low as 2.34 µM (compared to IC_{50} = 52.2 µM). Same effect is observed when cpd 6 inhibition curve is plotted with the increasing concentration of BDQ (B). This strong additive effect is confirmed by calculated IC_{50} values. Drop of BDQ's IC_{50} to 18.2 nM, which is below half of its original value to is achieved with only 4.68 µM of cpd 6 (C). Similarly, drop of cpd 6's IC_{50} below half its original value to 15.1 µM is achieved with only 6.25 nM of BDQ (D).

(A)

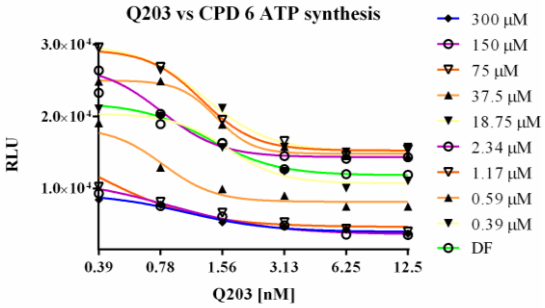

(B)

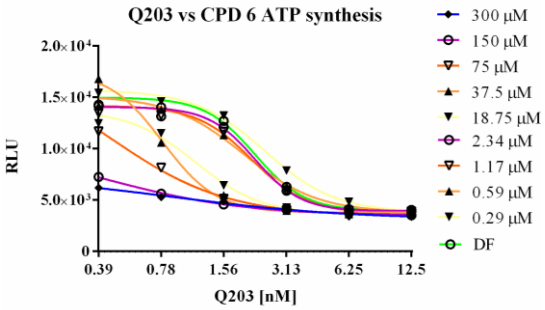

Figure 3-16: Additive effect of cpd 6 and Q203 on the whole cell ATP synthesis inhibition. In the WT *M. smegmatis* (A), Q203 cannot fully inhibit the ATP synthesis. However, when cpd 6 is added, the ATP synthesis significantly drops to almost full inhibition (Q203 at 12.5 nM = $1.8x10^3$ RLU, Q203 at 12.5 nM in combination with 75 µM of cpd 6 = $3.9x10^3$ RLU). Q203 inhibits the ATP synthesis only partially by inhibiting Cyt-bc_1, while the non-proton pumping cyt-*bd* remains uninhibited. In the Cyt-*bd* knock-out whole cell ATP synthesis (B) no further inhibition by cpd 6 was observed at the high Q203 concentration, suggesting its target downstream in the respiratory chain.

Synthesis of the hit compound 6 and its analogs

4. Synthesis of the hit compound 6 and its analogs

4.1 Materials and Methods

Reactions requiring anhydrous conditions were carried out using oven-dried glassware unless stated otherwise. Anhydrous DCM was freshly distilled from CaH_2 under nitrogen. All chemicals were obtained from commercial sources and used as received otherwise noted.

Thin layer chromatography (TLC) was carried out on Merck silica gel 60 F_{254} glass plates and column chromatography was carried out on silica gel, 230-400 mesh. Purity of the reported compounds was established by comparing the integrals of the peaks belonging to the compounds to the ones arising from impurities.

FTIR spectra were recorded on Shimadzu IR Prestige-21. Mass spectra were recorded on Thermo Scientific LCQ FLEET in ESI+ mode, reported in m/z values for the molecular ion detected. High resolution MS were recorded on Waters UPLC-QTOF Premier.

Melting points were acquired on a Stuart SMP3 melting point apparatus (Cole-Parmer, United Kingdom).

NMR spectra were recorded on JEOL ECA400SL or JEOL ECA 400 spectrometers. Chemical shifts are reported in parts per million (ppm, δ) and referenced to residual solvents, deuterated chloroform (CDCl3) (δ7.260) and deuterated dimethyl sulfoxide (DMSO-d6) (δ 2.500) or to tetramethylsilane (TMS) (δ0.0) for ^{1}H spectra and to DMSO-d6 (δ 39.43) or $CDCl_3$ (δ77.23) for ^{13}C NMR. Coupling constants (J) are reported in Hertz (Hz). Proton coupling patterns were described as singlet (s), doublet (d), triplet (t), quartet (q), septet (sept), doublet of doublets (dd), multiplet (m) and broad (br).

All characterization data of intermediates and final compounds are in the Supplementary data.

4.2 Proposed retrosynthesis for cpd 6 and analogs

Compound 6 is commercially available, however, to the best of our knowledge, the synthesis has not been reported. Nothing about it has been reported, neither in the literature or in patents. For the further studies of cpd 6, and for the generation of its analogs the synthesis had to be established. Here we suggest the general retrosynthesis for cpd 6 and analogs.

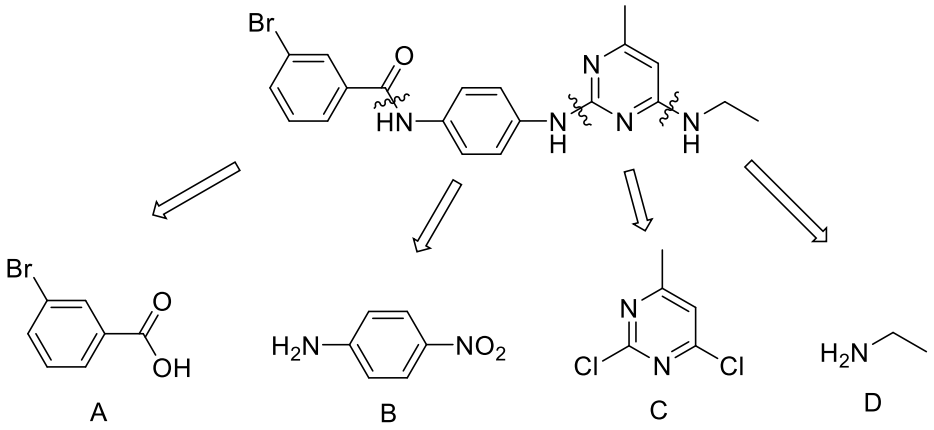

Figure 4-1: Retrosynthesis of cpd 6. The disconnection into a benzoic acid (A), *p*-nitroaniline (B), a substituted pyrimidine (C) and an alkylamine (D) was proposed.

We suggest disconnection of cpd 6 molecule into a benzoic acid (A), a *p*-nitroaniline (B), a substituted pyrimidine (C) and an alkylamine (D). In the first step, we propose synthesis of the left-hand side (LHS) fragment by aromatic nucleophilic substitution of the chlorinated pyrimidines (D) with alkylamines (C). As there are two chlorides in the molecule, two possible isomers might form, leading to low yield. Therefore, it is preferable to introduce this step first, on the smallest fragment. We suggest the preparation of the LHS fragment starting from commercially available substituted benzoic acids (A), converted into corresponding benzoyl chlorides coupled with *p*-nitroaniline (B), followed by the reduction of the nitro group, to ensure only monosubstituted aniline fragments. This fragment would provide to be a suitable nucleophile for the final coupling with the LHS fragment, which now allows aromatic nucleophilic substitution only at single position.

This convergent synthesis approach lowers the complexity and allow higher atom economy. Furthermore, its modularity would allow for easy combination of different LHS and RHS substituents, which is well in line with

the proposed synthesis of cpd 6 analogs. These reactions use simple and well-established reactions, with only simple molecules as the by-products.

4.3 Synthesis of *N*-benzoyl *p*-nitroanilines

The *N*-benzoyl diamino-1,4-benzenes were prepared according to Boger *et al.* [188]. In the first step, benzoic acid chloride was coupled with *p*-nitroanaline using Schotten-Baumann conditions, followed by hydrogenation. Benzoyl chlorides, as a starting material were either obtained from commercial sources or were prepared from the corresponding benzoic acids by treatment with oxalyl chloride in dichloromethane in the presence of a catalytic amount of *N*,*N*-dimethylformamide. The product was obtained in nearly quantitative yield and directly used in the next step. *p*-Nitro aniline in tetrahydrofuran was treated with benzoyl chlorides in the presence of 2 eq. of potassium carbonate, and stirred overnight at room temperature. As the product precipitated from THF, the reaction mixture was filtered and the obtained solid was washed with water and hexane to give the desired product.

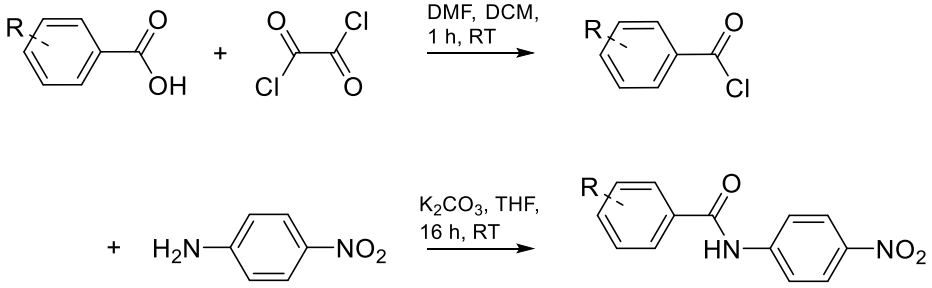

Figure 4-2: Synthesis of the *N*-benzoyl *p*-nitroanilines.

In this variation of the Schotten-Baumann reaction, the base is the solid phase, as opposed to the traditional Schotten-Baumann reaction where the two phases consist of an aqueous and an organic phase. The purpose of the base, dissolved in the aqueous phase, is to neutralise the acid, a by-product of the reaction, which would otherwise protonate the amine, thus stopping the reaction. This variation was preferable because of the very low solubility of the products.

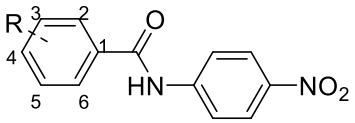

Figure 4-3: Atom numbering of the *N*-benzoyl *p*-nitroanilines.

Table 4-1: Yields of the *N*-benzoyl *p*-nitroanilines.

R	Position	Yield
AcO (**1-1**)	3	90%
Br (**1-2**)	3	98%
H (**1-3**)	NA	48%
F (**1-4**)	3	69%
Me (**1-5**)	4	64%
OMe (**1-6**)	4	77%

To avoid undesired reactions of the 3-hydroxy analog, the acetyl protective group was used (**1-1**). In their procedure, Tran *et al.* [189] reported that the compound was directly prepared from 3-hydroxybenzoic acid and *p*-phenylenediamine using HATU (1-[Bis(dimethylamino)methylene]-1H-1,2,3-triazolo[4,5-b]pyridinium 3-oxid hexafluorophosphate), which avoids protecting and deprotecting step. Although, we were not able to replicate this procedure, our overall yield of the hydrogenated product **2-1** is 58%, which is reasonably close to their reported yield 65%. The proton and carbon NMR spectra are in accordance with those reported by Tran *et al.* [189]. In the second step, the *N*-benzoyl *p*-nitroanilines, except for the 3-bromo-*N*-(4-nitrophenyl)benzamide (**1-2**), were reduced according to the reported procedure [188], with palladium on carbon in EtOAc, under pressure a 50 psi of H_2 for 1 h at RT, in almost quantitative yield. In the case of 3-bromo-*N*-(4-nitrophenyl)benzamide, these conditions would remove the bromine substituent on the benzene ring. Therefore, for the initial small batch reduction, Zn (1.5 w) was used with HCl added dropwise at a rate 1 ml/hour at 45°C, until all of the zinc was consumed. Because this approach would not be suitable for scaled up the synthesis, we opted for platinum on carbon poisoned with sulphur, which should be sufficient for reducing nitro group but mild enough to preserve the bromine substituent. Richey and Yu [190] selectively reduced the nitro group of a dibenzoxapine containing a bromo moiety by using sulfided platinum on carbon 5% wt. in THF at 50 psi and RT during 2 hours.

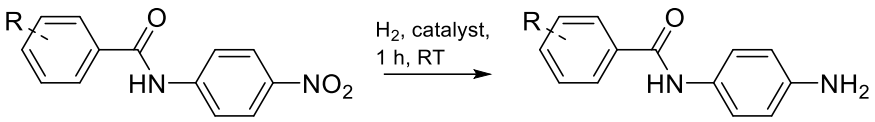

1-1 to **1-6** **2-1** to **2-6**

Figure 4-4: Hydrogenation of *N*-benzoyl *p*-nitroanalines.

First, to hydrogenate 3-bromo-*N*-(4-nitrophenyl)benzamide with a platinum on carbon poisoned with sulphur, the atmospheric pressure of hydrogen at room temperature for 3 h was used, the same conditions in which lead to debromination in the presence of palladium on carbon. These conditions were too mild to reduce the nitro group, therefore we gradually the increased temperature and the pressure of hydrogen. Only at 100°C and 100 psi, partial reduction of the nitro group was observed. A prolonged time of the reaction, from overnight to 48 h, lead to complete reduction of the nitro group, while preserving the bromide (Table 4-2).

Table 4-2: Hydrogenation of the 3-bromo-*N*-(4-nitrophenyl)benzamide.

catalyst	**reaction time**	**pressure**	**temperature**	**Et_3N**	**outcome**
Pd on C	3h	atm	RT	-	debrominated
Pt on C sulfided	3h	atm	RT	+	starting material
	3h	50 psi	RT	+/-	starting material
	overnight	50 psi	50°C	-	starting material
	overnight	50 psi	80°C	-	starting material
	overnight	100 psi	50°C	-	starting material
	overnight	100 psi	80°C	-	starting material
	overnight	100 psi	100°C	-	~ 75% (calc. from NMR)
	48 h	100 psi	100°C	-	100%

We were not able to hydrogenate the *N*-benzoyl *p*-nitroanalines prepared from 3-amino benzoic acid and the picolinic acid. The compounds probably decomposed as were not able to recover the starting material. The acetic and trifluoracetic protecting groups for the 3-amino substituted compound, as well

as a combination of various milder reaction conditions we applied, however without any success. In case of the trifluoracetic protecting group, a small amount of reduced product was observed in the crude NMR spectrum, but unfortunately, we were not able to separate it from other impurities.

4.4 Synthesis of alkyl-substituted chloropyrimidines

First, chloropyrimidines were prepared from uracil, 6-methyl uracil and thymine by heating at reflux in $POCl_3$. Chloropyrimidines were subsequently reacted with various alkylamines in ethanol at RT, 16h, using *N*-ethyl-*N*,*N*-diisopropylamine as a base. When 5-methyldichloropyrimidine (**3-1**) reacted with ethylamine, only one isomer (**4-1**) was obtained. Similarly, in the case of the substitution of the 6-methyldichloropyrimidine (**3-2**), a single isomer **4-2a** was also expecting , presuming that chloride at 4 position is more reactive than position 2 as reported by others [191]. Under similar conditions (*N*-ethyl-*N*,*N*-diisopropylamine, ethanol at 20°C for 20h) this reaction was described as being regioselective. However, when the substitution with ethylamine was carried out, on the TLC only starting material and one product was observed, but upon further inspection of the crude NMR, another isomer was found. The minor isomer **4-2b** and the starting material had the same R_f, which gave a false impression of only one isomer being formed.

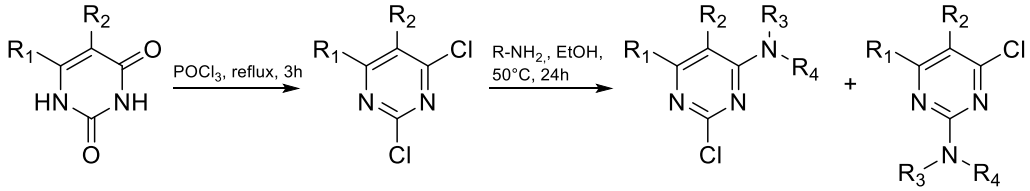

Figure 4-5: Synthesis of alkyl-substituted chloropyrimidines

The alternative conditions for this reaction uses THF as a solvent, with a wide range of temperatures and different organic or inorganic bases, however the yields, the completion and the ratio of isomers are usually very similar to ours *e.g.* tetrahydrofuran at 30°C for 18h with 4-ethylamine substituted (**4-2a**) product 25% to 2-ethylamine substituted product (**4-2b**) 31% [192]. The only improvement seems to be using lithium perchlorate in diethyl ether for 24h improving the yield to 50% of 4- substituted product with only 7% of the 2-substituted isomer [193].

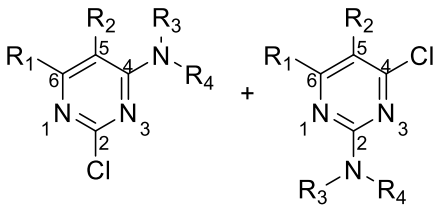

4-2a to **4-8a** **4-2b** to **4-8b**

Figure 4-6: Numbering of the alkyl-substituted chloropyrimidines.

Table 4-3: Yields of the 2-substituted and 4-substituted chloropyrimidines.

R	Methyl position	4-substituted isomer [%]	2-substituted isomer [%]
ethylamine (**4-1**)	5	56	0
ethylamine (**4-2**)	6	33	14
isopropylamine (**4-3**)	6	53	46
diethylamine (**4-4**)	6	4	65
glycine ethylester (**4-5**)	6	48	18
ethanolamine (**4-6**)	6	27	51
methylamine (**4-7**)	6	42	30
ethylamine (**4-8**)	NA	63	17

The different regioisomers could not be distinguished by one-dimensional ^{1}H or ^{13}C NMR spectroscopy, as their spectra have the same pattern and differ only by their chemical shifts. Therefore, to gain insight into the regiochemistry of the products, two-dimensional NMR spectroscopy was used to obtain additional structural information describing the spatial arrangement of the isomers. The 4-substituted isomer would have substituents close to the aromatic proton, compared to the 2- substituted isomer, where these groups are far from each other (Figure 4-7). To exploit this difference, we opted for Nuclear Overhauser effect spectroscopy (NOESY). NOESY is based on the Nuclear Overhauser effect which correlates nuclei physically close in space up to 3.5 Å, as opposed to traditional NMR techniques where spins are coupled through chemical bonds. It is widely used in organic chemistry to elucidate structure and regiochemistry of organic compounds as well as in protein structure

determination, where it provides information about mutual distance between different amino acid residues [194].

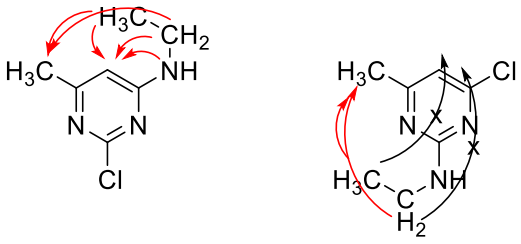

Figure 4-7: Example of spatial proximity of the 4-substituted isomer where the nuclei are physically close enough to give cross peak with aromatic proton, as opposed to the 2-substituted isomer, where the distance is too big.

We were able to identify all the regioisomers by NOESY (Figure 4-17 - Figure 4-15), except for isomers **4-5a** and **4-5b**, where NOESY spectra were not conclusive. In this case one of the isomers in EtOAc was crystallised and the structure by X-ray crystallography was obtained (Figure 4-11).

Following the general procedure, the desired isomer (**4-2a**) was obtained with yield 33% and minor product (**4-2b**) with 14% yield which is slightly lower compared to recently published conditions with include THF, 30°C for 18 h, with yields 54% and 34% respectively. Our isomer identification by NOESY was confirmed by comparison with the published spectra [192], where shifts had consistent difference of 0.8-0.15 ppm, probably due to the wrong referencing, and identical melting points (reported: mp 73-74°C, 4-substituted; 90-91°C, 2-substituted, found: 74-75°C).

The desired 4-substituted isomer **4-3a** had a cross peak between the aromatic proton (6.04 ppm) and the aliphatic methyl (1.21 ppm), as opposed to the 2- substituted isomer **4-3b** which did not have any cross peaks in this region.

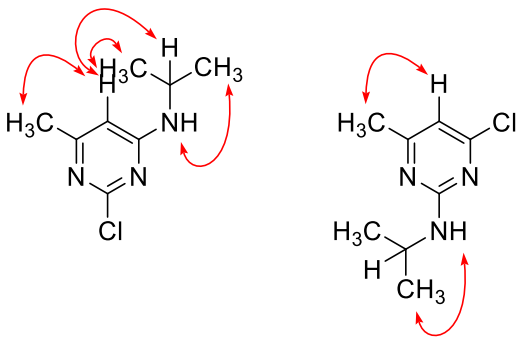

Figure 4-8: Spatial proximity of protons (red arrows) in **4-3** isomers.

The desired isomer **4-4a** was obtained in a very poor yield of 4% (65% for the undesired product **4-4b**), which is partially due to the flash chromatography purification (3:1 hexane:EtOAc), where the desired product eluted very closely to the starting material. In the NOESY spectrum of the desired isomer **4-4a** the cross peaks of diethyl amines methyls (1.16 ppm) and methylenes (3.61 ppm) with aromatic proton (6.32 ppm) and aromatic methyl (2.27 ppm) can be clearly seen. On the other hand, these cross peaks are not present in the 2- substituted isomer **4-4b** as the distance between these protons would be too big to generate the cross peak. Another reported synthesis include 4-diethylamino-6-methyl-1(3)H-pyrimidin-2-one or 4-chloro-6-methyl-2-methylthiopyrimidine as starting material, which would however require the preparation of different starting materials and would add additional steps to the synthesis. In their paper of chlorination of 6-methyluracil with phosphorus oxychloride in the presence of trialkyamines, Gershon, H., *et al.* [195] report the opposite assignment of the isomers, however, "the structure of these amines were postulated and not established."

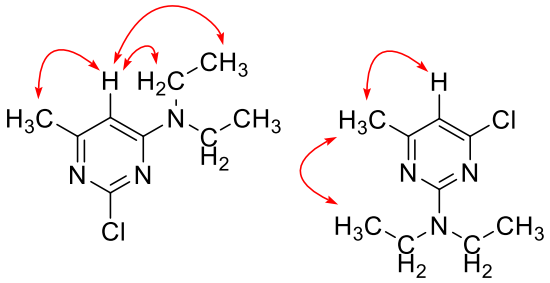

Figure 4-9: Spatial proximity of protons (red arrows) in **4-4** isomers.

The glycine ethyl ester is the longest and the most flexible substituent in the whole series, therefore the alkyl chain can reach into the proximity of the aryl proton and methyl in the case of the both isomers. The NOESY spectra were thus not conclusive. The minor product **4-5b** was successfully crystallised and subjected to the x-ray crystallography. The structure was solved and it was identified as the undesired isomer (Figure 4-11).

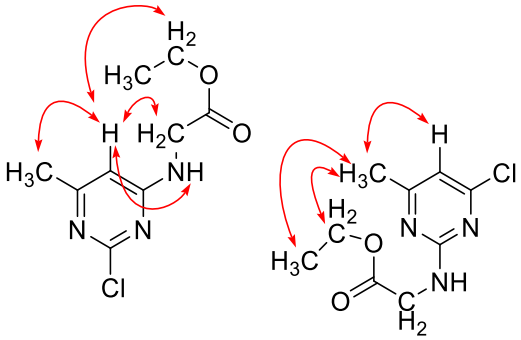

Figure 4-10: Spatial proximity of protons (red arrows) in **4-5** isomers.

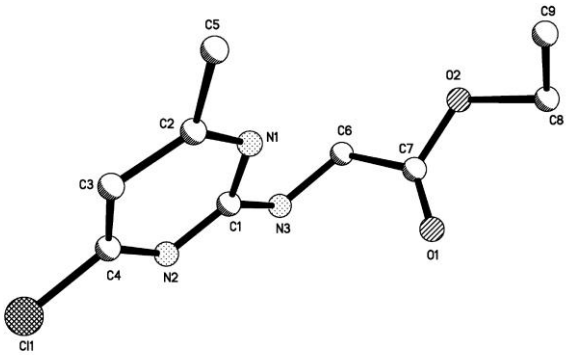

Figure 4-11: X-ray structure of the minor **4-5b** regioisomer.

NOESY spectra of isomer **4-6a** showed a cross peak between the aromatic proton (6.12 ppm) and both methyne protons (2.09, 1.86 ppm), as well as with the hydroxyl proton (1.52 ppm). No aromatic proton cross peak in spectra of isomer **4-6b** were observed (Figure 4-17).

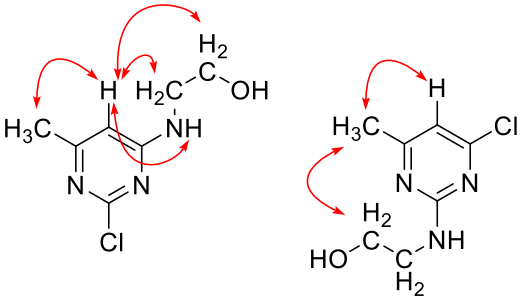

Figure 4-12: Spatial proximity of protons (red arrows) in **4-6** isomers.

Reported conditions used 30% methylamine in ethanol, with microwave irradiation at 110 ^{o}C for 30 minutes, with low yields 17% and 27 % for the **4-7a** and **4-7b** isomers, respectively. The authors identified the regioisomers using NOE, however both reported spectra are the same [196]. In the NOESY spectra of the **4-7a** cross peaks between methyl amines methyl (2.95 ppm) and the

aromatic proton (6.09) ppm as well as aromatic methyl (2.35 ppm) was observed. No cross peaks in this region for the other isomer **4-7b** was observed (Figure 4-18).

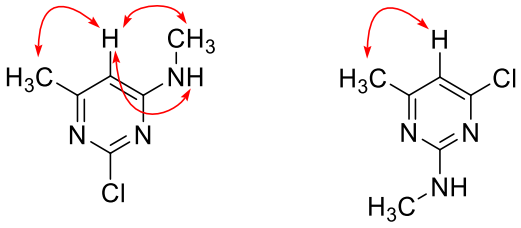

Figure 4-13: Spatial proximity of protons (red arrows) in **4-7** isomers.

In the NOESY spectrum of **4-8a** the methylene protons (3.36 ppm) have a clear cross peak with the aromatic proton (6.24 ppm), whereas **4-8b** isomer does not have any such cross peak (Figure 4-19).

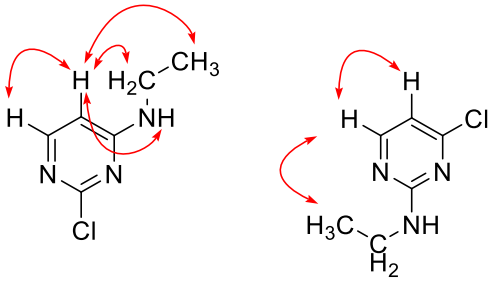

Figure 4-14: Spatial proximity of protons (red arrows) in **4-8** isomers.

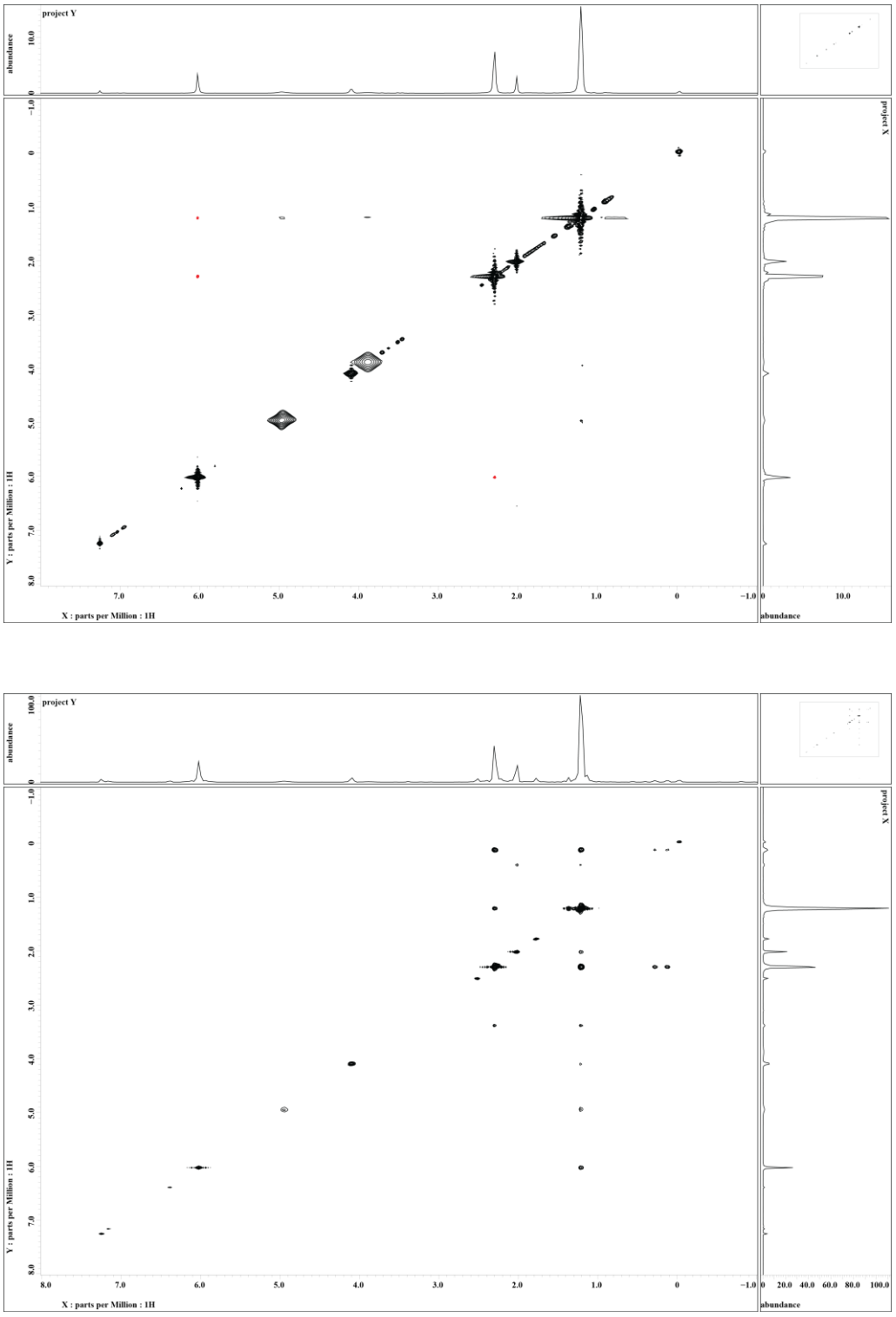

Figure 4-15: NOESY spectra of **4-3a** (top) and **4-3a** (bottom.)

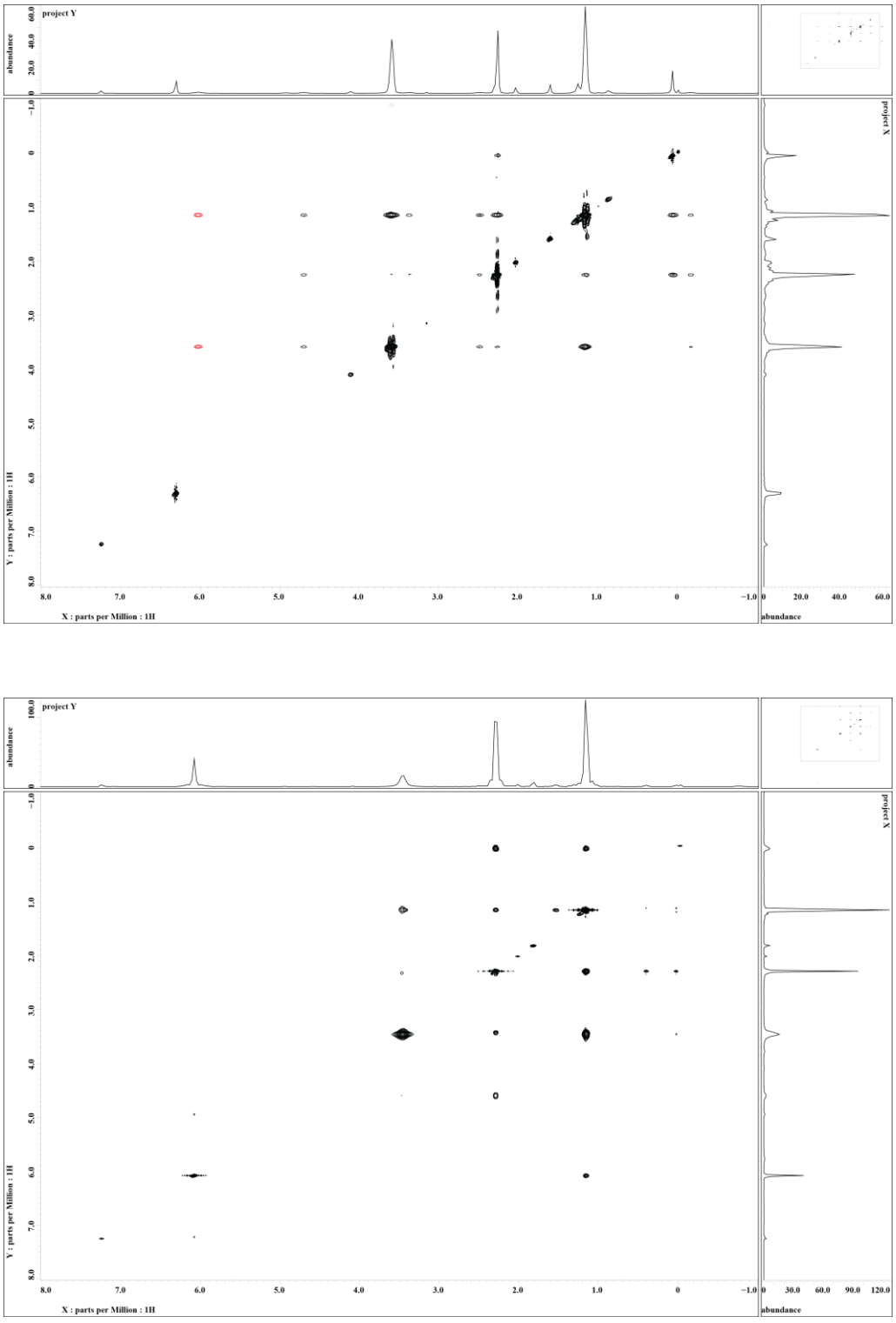

Figure 4-16: NOESY spectra of **4-4a** (top) and **4-4a** (bottom.)

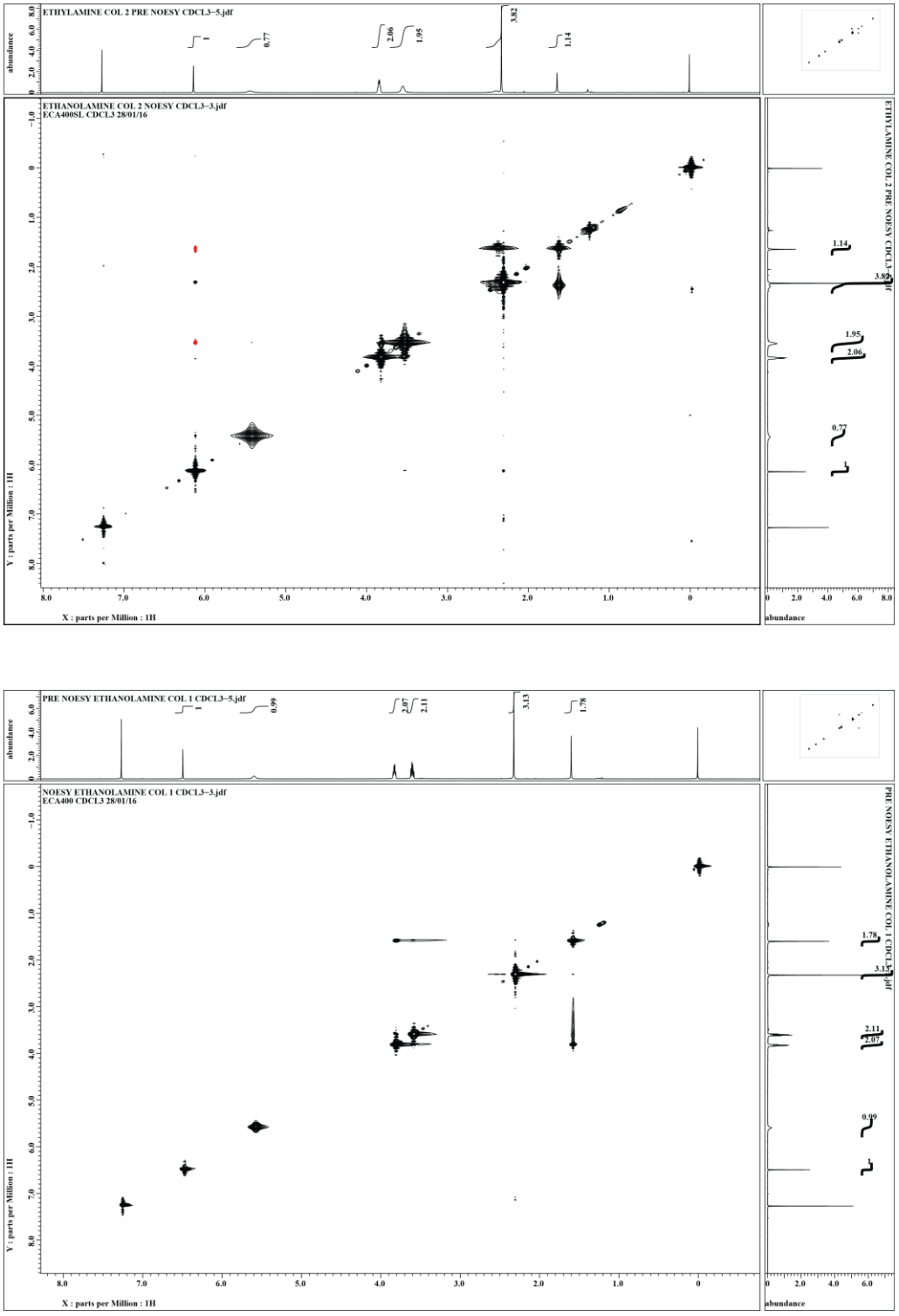

Figure 4-17: NOESY spectra of **4-6a** (top) and **4-6a** (bottom).

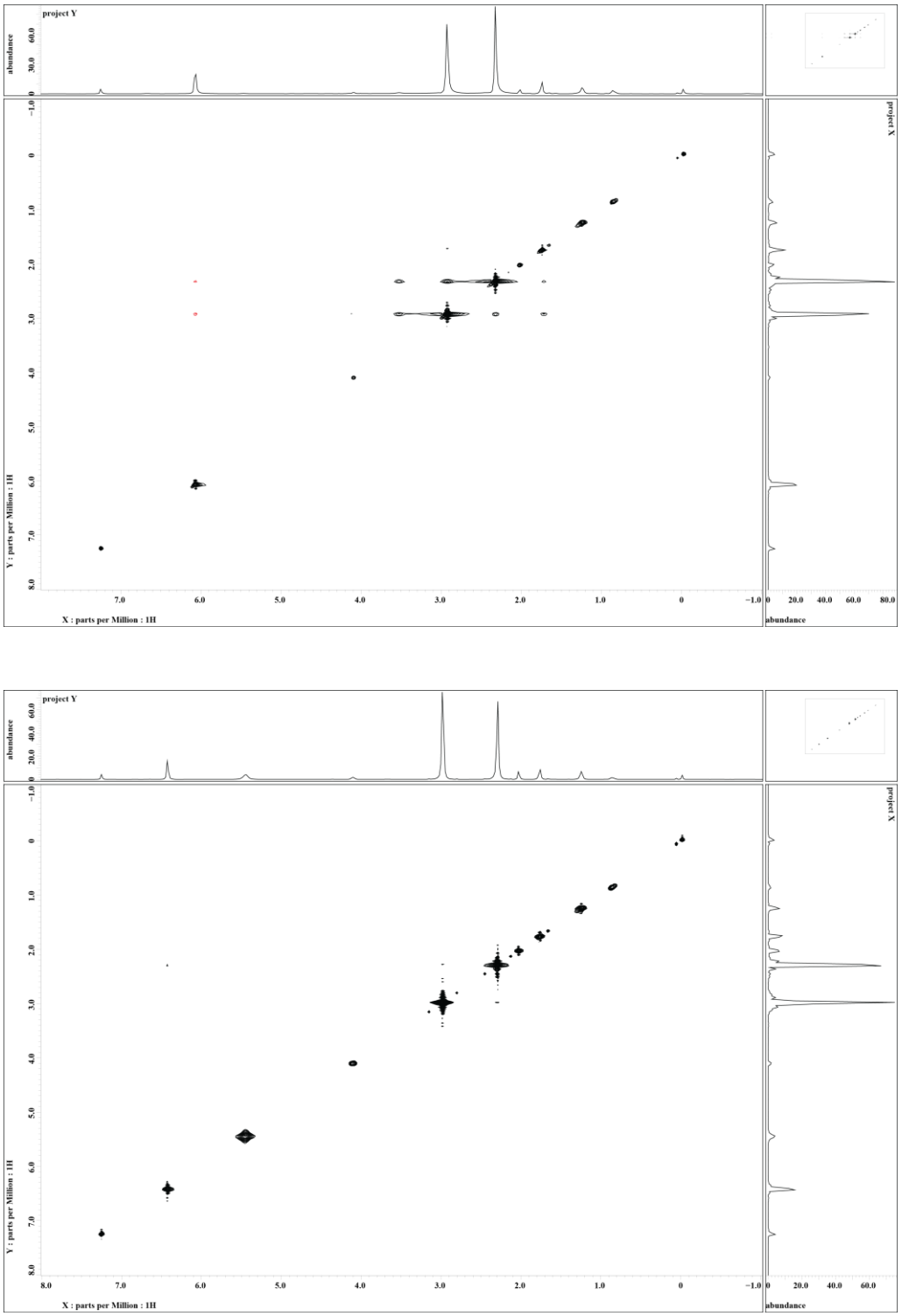

Figure 4-18: NOESY spectra of **4-7a** (top) and **4-7b** (bottom).

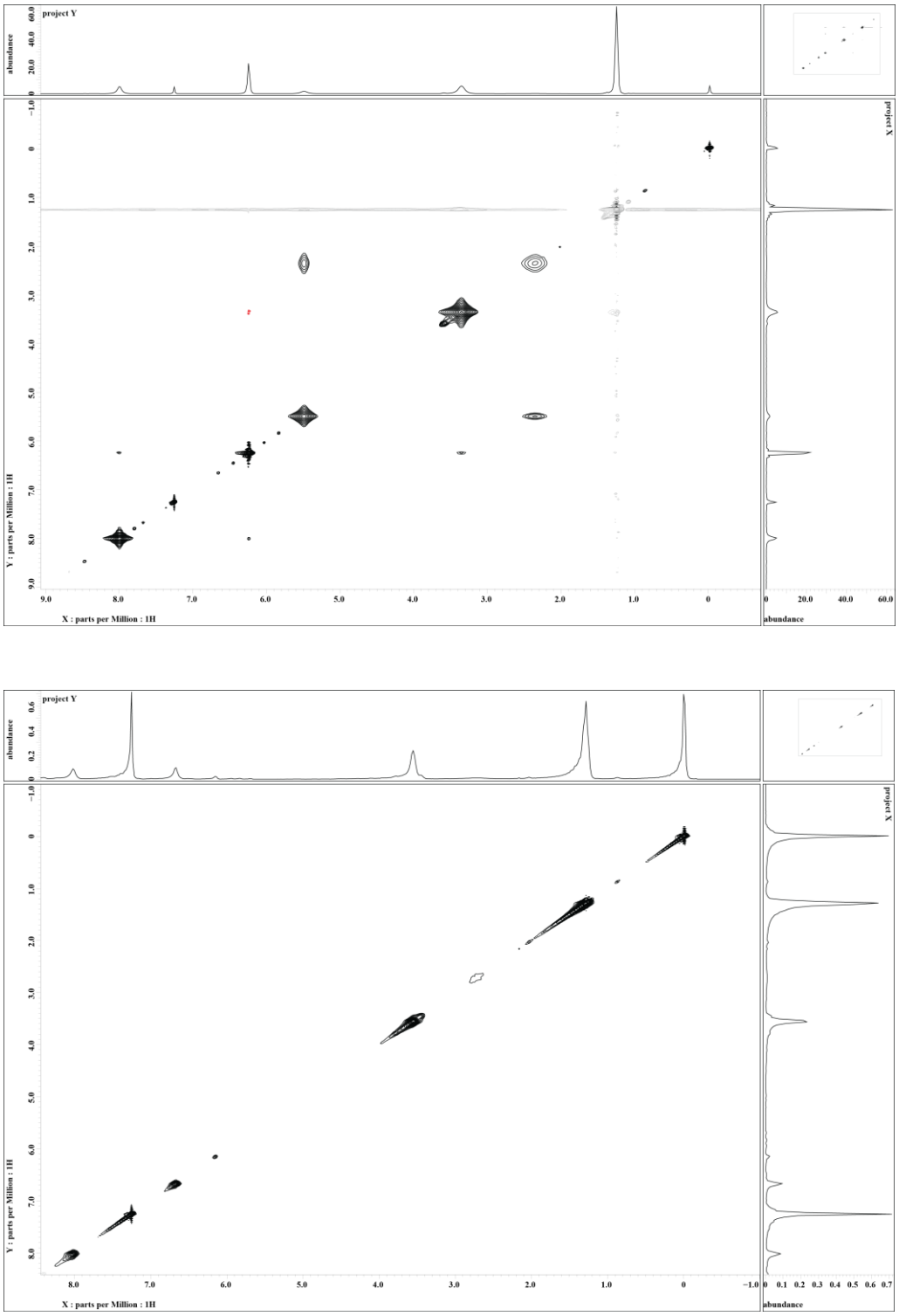

Figure 4-19: NOESY spectra of **4-8a** (top) and **4-8a** (bottom).

We tried to find a pattern to identify the correct isomers without NOESY. It seems that for the simple alkylamines the 4-substituted isomer is the major product, however this is not true for ethanolamine and diethylamine analogs. We noticed that one of the isomers always has the broad peak for the alpha carbon protons. We suggest a that two resonance structures of these isomers exist, so that rotation around the amine bond is hindered, due to its partial double bond character, which could cause the peak broadening (Figure 4-20). Unfortunately, there was no correlation between the peak broadening and the position of the substitution.

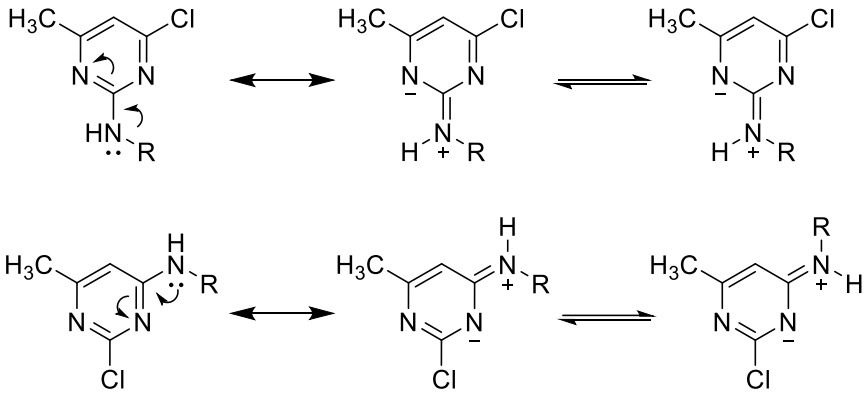

Figure 4-20: The resonance structure of substituted pyrimidines causing the peak broadening.

Table 4-4: Peak broadening pattern of the chloropyrimidines.

R	**4-substituted isomer**	**2-substituted isomer**
Ethylamine (**4-2**)	Broad	Sharp
Isopropylamine (**4-3**)	Broad	Sharp
diethylamine (**4-4**)	Sharp	Broad
glycine ethylester (**4-5**)	Sharp	Broad
ethanolamine (**4-6**)	Broad	Sharp
Methylamine (**4-7**)	Sharp	Broad
desMe ethylamine (**4-8**)	Broad	Sharp

The last step of the synthesis was the coupling of the LHD and RHS to obtain the final product. In the literature, most of the reported procedures for couplings of the chlorinated pyrimidines and aromatic amines are done in microwave synthesisers. Under these conditions, the product was obtained,

identified in the crude NMR spectrum, however in low yields, and we were not able to effectively isolate a pure product. Therefore, alternative conditions of dioxane at reflux were employed (Figure 4-21). First, no product formation was observed, however after prolonged time (2 – 5 days), the product was formed in moderate to excellent yields and could be isolated by simple filtration. This approach also allows for easy and successful scale up to multigram synthesis.

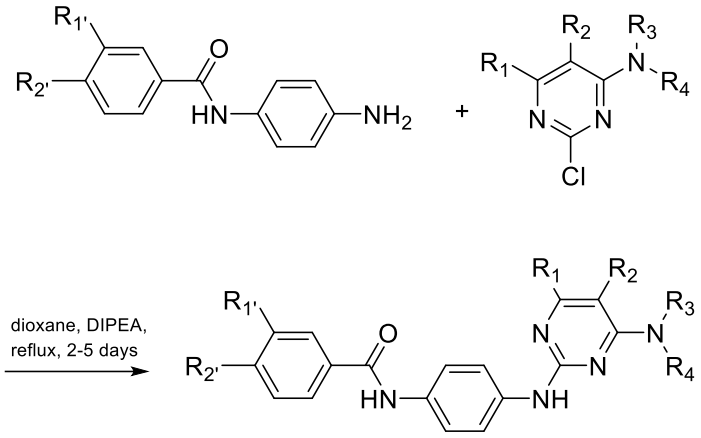

Figure 4-21: Final coupling of the *N*-benzoyl *p*-aminoanalines and pyrimidine chlorides to obtain analogs **5-1** to **5-15**.

4.1 Results and activity of the analogs

A viable route for the synthesis of cpd 6 and its analogs was devised in a simple, convergent and scalable way (Figure 4-22). Including cpd 6, 16 analogs were prepared, with different substitution on the LHS and RHS. SAR for this series of analogs was proposed, and a new series of analogs were designed.

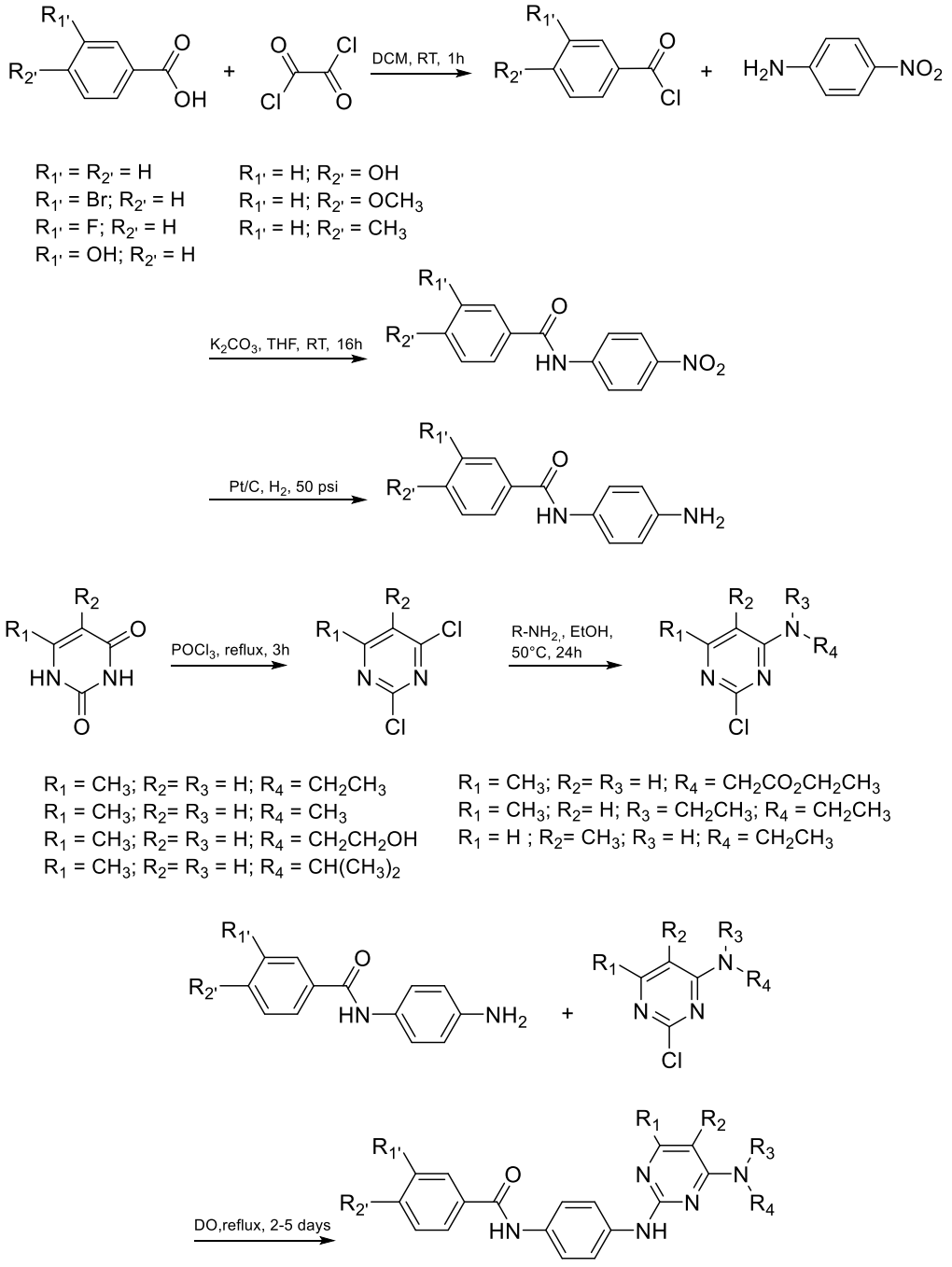

Figure 4-22: General scheme of the synthesis of the cpd 6 and its analogs.

The signals in the ^{1}H NMR spectra of commercially obtained cpd 6 and our synthesised cpd 6 did not overlap in the aromatics region (Figure 4-23), however it is known that the shifts of the protons near to basic nitrogen atoms can be influenced by pH, due to protonation. To test this hypothesis, trifluoroacetic acid was gradually added to an NMR sample of cpd 6 synthesised in our lab. As the acid was added, the aromatic peaks shifted towards the chemical shifts of the purchased cpd 6. The purchased cpd 6 might have contained acidic impurities which could have protonated the aniline nitrogen resulting in the shift of the aromatic protons.

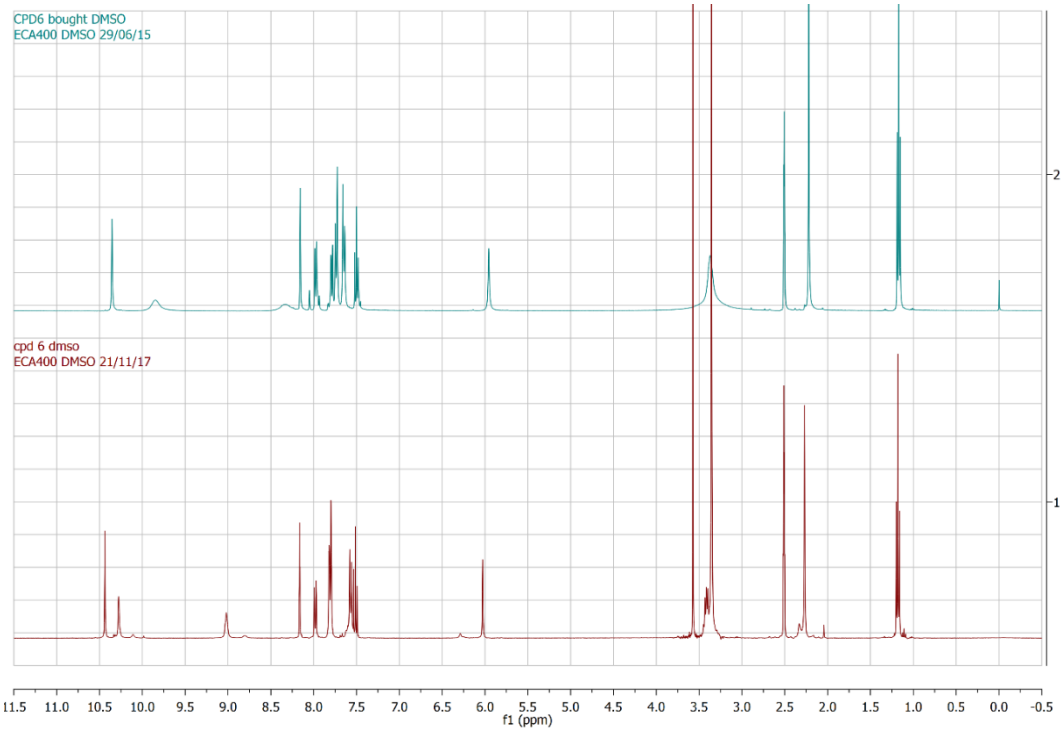

Figure 4-23: Spectra of the commercially obtained cpd 6 (cyan) and our synthesised cpd 6 (red). Peaks overlap at the aliphatic region however some peaks at the aromatic region are not identical.

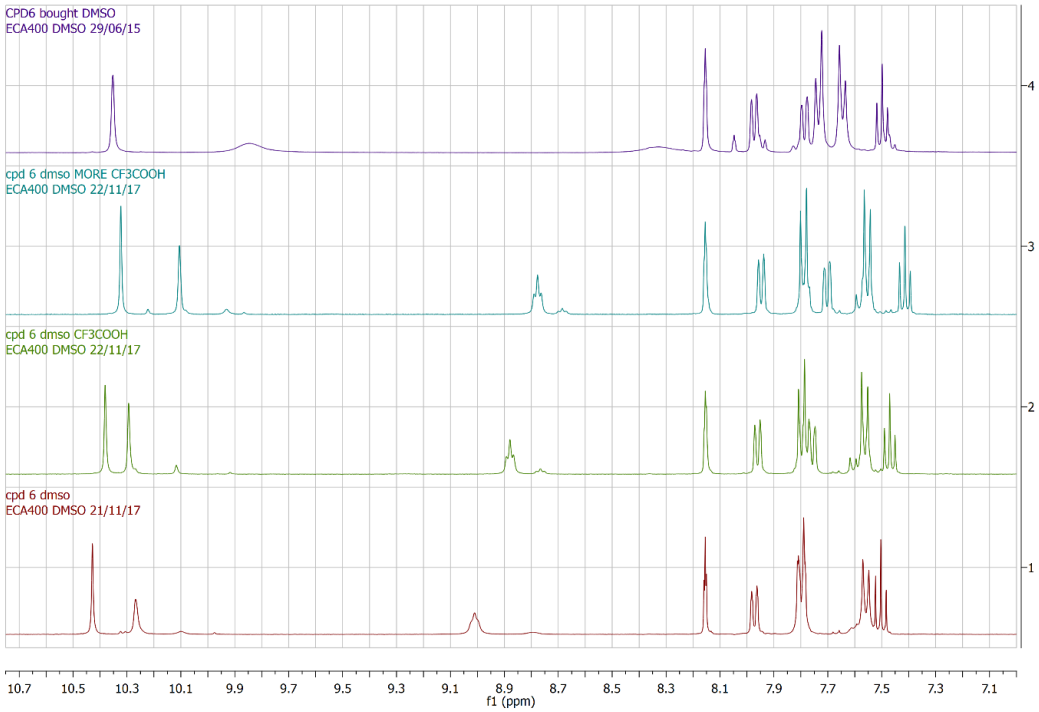

Figure 4-24: Shift of the aromatic peaks of the synthesised cpd 6 with increasing acidity (increasing concentration trifluoroacetic acid from red to cyan) are converging toward the commercially available cpd 6 (purple).

The MIC_{50} and the profile of the inhibition curve of the synthetized compound 6 is identical to the originally purchased cpd 6 which supports our claim based on the chemistry data that these two compounds are identical.

(A) **(B)**

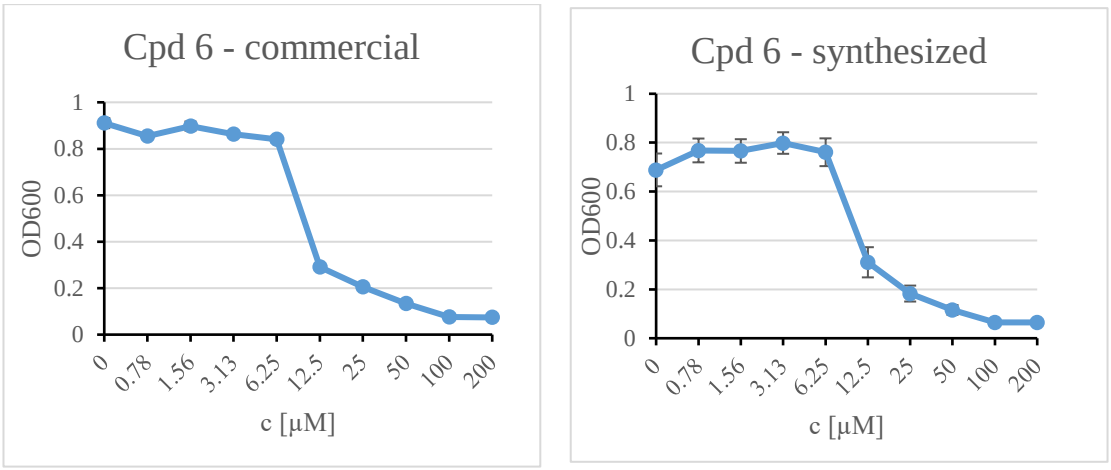

Figure 4-25: Comparison of the commercially obtained (A) and synthesised (B) cpd 6. Their growth inhibition profile is equivalent, supporting the chemistry data proving that they are identical.

To assess the antimycobacterial activity of the newly synthesised analogs **5-1** to **5-15**, all the compounds were tested for ATP synthesis inhibition on IMVs and growth inhibition on *M. smegmatis* (table 2).

Table 4-5: Growth inhibition of *M. smegmatis* and inhibition of ATP synthesis on IMVs by cpd 6 and its analogs.

name	R_1	R_2	IC_{50} [µM]	MIC_{50} [µM]
Cpd 6	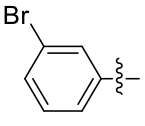	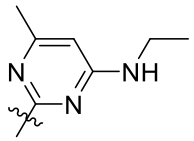	0.30 ± 0.02	10.77 ± 0.43
5-1	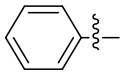	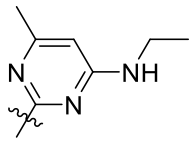	1.65 ± 0.16	26.94 ± 1.396
5-2	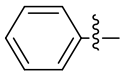	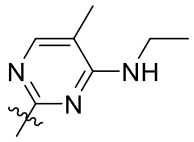	0.90 ± 0.058	39.0 ± 1.907
5-3	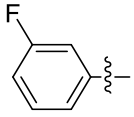	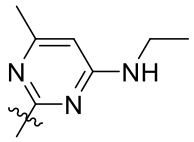	0.26 ± 0.05	18.72 ± 1.246
5-4	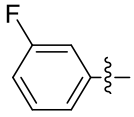	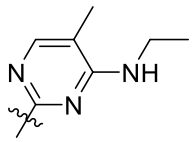	0.92 ± 0.042	43.51 ± 3.57
5-5	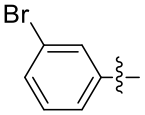	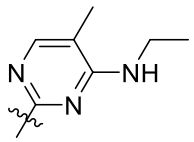	0.62 ± 0.08	12.32± 0.73
5-6	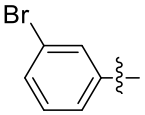	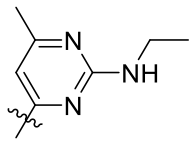	0.38 ± 0.03	20.82 ± 1.90
5-7	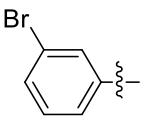	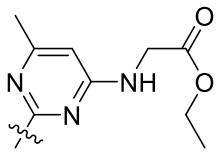	2.01 ± 0.16	15.54 ± 1.52

name	R_1	R_2	IC_{50} [μM]	MIC_{50} [μM]
5-8	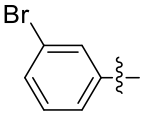	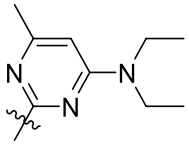	10.8 ± 2.8	75.79 ± 13.15
5-9	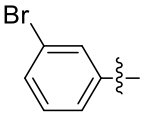	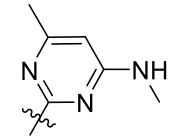	0.39 ± 0.06	12.4 ± 0.56
5-10	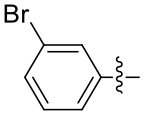	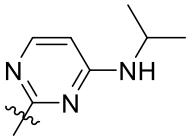	2.69 ± 0.21	50.1 ± 4.5
5-11	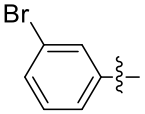	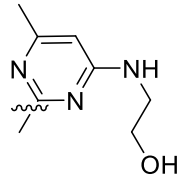	0.42 ± 0.03	19.02± 1.50
5-12	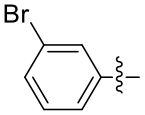	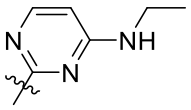	1.03 ± 0.25	16.82± 2.6
5-13	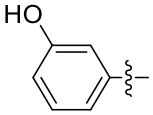	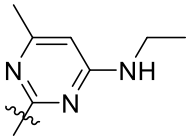	1.16 ± 0.09	79.57 ± 9.13
5-14	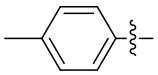	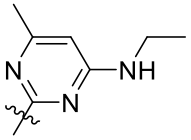	0.39 ± 0.02	31.76 ± 7.8
5-15	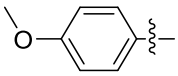	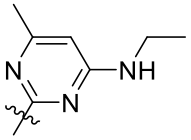	0.69 ± 0.06	17.28 ± 2.26

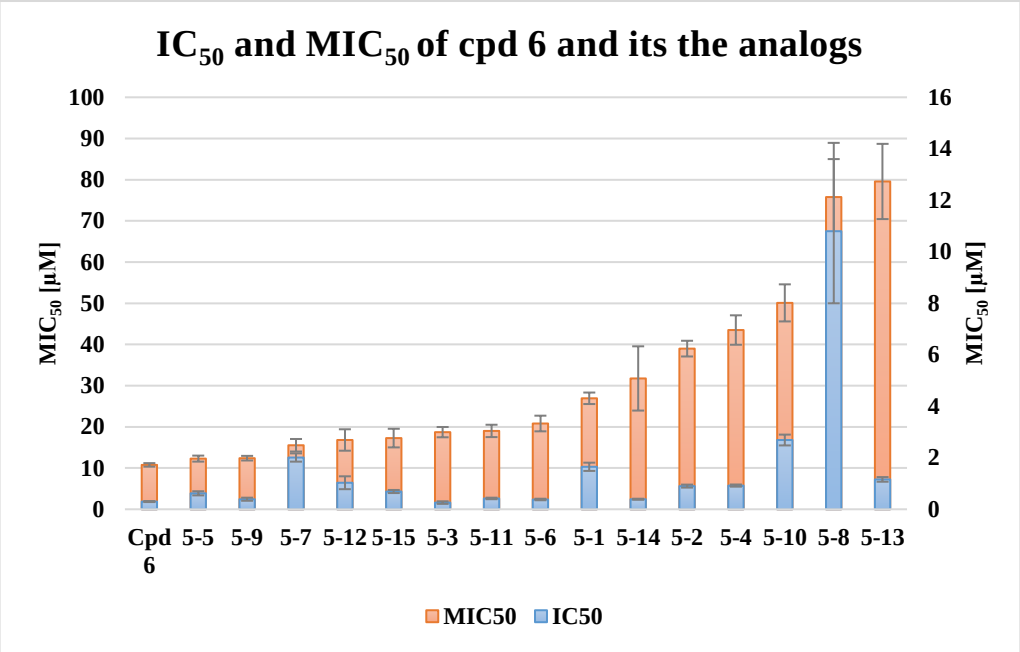

Figure 4-26: The MIC_{50} (left axis, bar chart) and IC_{50} (right axis, scattered plot) of compound 6 and its analogs.

When the predicted affinity of the analogs was plotted and compared to the measured MIC_{50}, unfortunately no strong correlation was observed. This discrepancy can be explained by several variables affecting the compounds biological effect. This prediction is based solely on the calculated affinity to the target, not taking into consideration physicochemical properties, influencing solubility, cell penetration, lipophilicity and other phenomenon involved in the drugs kinetics and dynamics. A similar effect in the MIC_{50} – IC_{50} plot was observed, where correlation is stronger, but still not completely conclusive. However, IC_{50} and MIC_{50} are both reflecting these variables, because the IC_{50} is measured on the inverted membrane vesicles, where solubility, lipophility *etc.* might play a similar role as in the whole cell. Low correlation might be also influenced by the relatively low number of observations and clustered variation of the observations, where most of the compounds have MIC_{50} and IC_{50} in the similar range, except the analog **5-8**, which is the compound with the lowest activity.

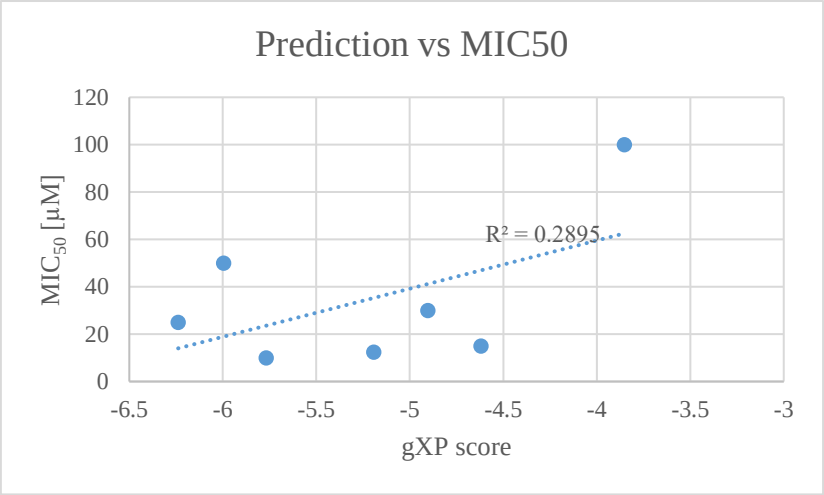

Figure 4-27: Docking score vs. MIC_{50} of the analogs.

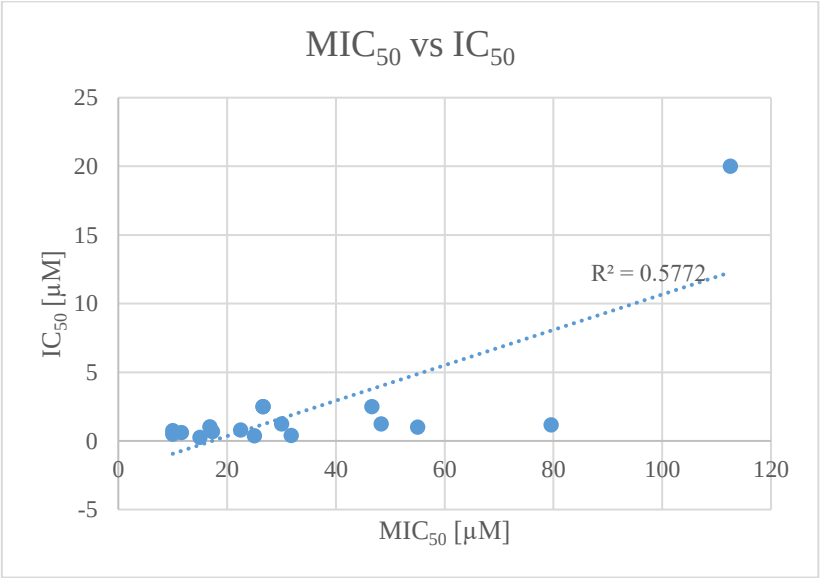

Figure 4-28: Correlation between MIC_{50} and IC_{50}.

4.1.1.1 Solubility of cpd 6 and analogs

One of the major problems of drug candidates is the solubility of these drugs in water. Current drug candidates such as BDQ and Q203 are considered to be poorly soluble or insoluble in water. Herein, poorly soluble drugs or insoluble drugs face poor absorption after consumption. With lower absorption rates, the bioavailability of these drug candidates would also decrease. Thus, this may result in inadequate amount of drugs available in the systemic circulation or at the site of action. Studies have found that the modification of drug candidates during drug development states are more desirable as compared to altering the properties of the drug during formulation step [197]. Although so, there are still cases in which drug candidates are formulated with additional surfactant

adjuvants or the utilization of the salt form of the drug to improve solubility. Keeping in mind that cpd 6 is still undergoing drug development, the former method to solubilize drugs during development have been utilized in this study. All solubility and toxicity experiments were performed with the help of Dr. Pang Yi Yun.

Solubility can be expressed in two different manners. First, as the thermodynamic solubility, defined as the maximum amount of the compound in the solution in the equilibrium with the solid state at given temperature and pressure. Second, the kinetic solubility usually represents the solubility in the supersaturated state. In practice, for the thermodynamic solubility, the solid is added to the solution and the amount of the solubilised compound is measured. On the other hand, in kinetic solubility, the compound is added already solubilised and concentrated, typically in DMSO, creating supersaturated solution, where the excess of the compound precipitates. Even though the thermodynamic solubility might be more accurately representing the solubility of the compound, it is labour intensive and involves handling of very minute amounts of the solid [198]. Therefore, the kinetic solubility, where the drugs are usually in the stock DMSO solution and are easy to handle, is the most widespread used, and was the method chosen for testing of the cpd 6 and analogs.

For the kinetic solubility assay, three analogs were tested to sample the whole series. First, cpd 6, the original hit and the most active compound, second, **5-15**, moderately active with MIC_{50} = 17.3 μM, having methoxy substituent on the benzene ring, and third, the least active analog **5-8** with MIC_{50} = 75.8 μM, disubstituted amine on the pyrimidine ring. This choice should reflect different activity and two different modifications to the original cpd 6. Solubility of cpd 6 was calculated as 23.8, 7.7 and 2.0 for pH 7.4, 6.0 and 2.0, respectively. Other two measured analogs **5-8** and **5-15** have significantly better solubility. Solubility for analog **5-15** was calculated as 30.8 μM (pH 7.4), 74.5 μM (pH 6.0) and > 100 μM (pH 2.0) and for analog **5-8** as 69.6 μM (pH 7.4) 70.0 μM (pH 6.0) and > 100 μM (pH 2.0) (Figure 4-29). Although the more soluble analogs are less active than cpd 6, these results suggest, that in the next series of the analogs, the solubility might be improved with preserving or even improving the antimicrobial activity.

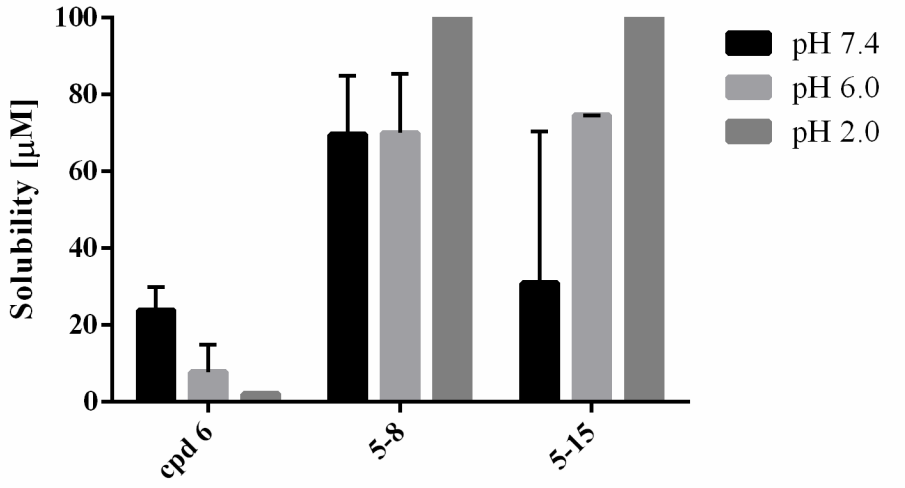

Figure 4-29: Solubility of cpd 6, analogs **5-8** and **5-15** at pH 7.4, 6.0, 2.0. Both analogs have significantly higher solubility at all measured pH, which is promising for the design of the next series of analogs with higher solubility and activity.

4.1.1.2 Cytotoxicity of cpd 6 and analogs

As tuberculosis affects mainly the lungs, the potential drug candidate should penetrate and reach high concentration in the lung tissue. Therefore, A549 cell line, human cancerous lung epithelial cells, was chosen for cytotoxicity assay. The same compounds for toxicology testing as for solubility were retained. Compounds were incubated with cells for 24 hours, the cell viability was calculated compared to the DMSO standards and the toxicity IC_{50} was obtained from the curve fitting. For cpd 6, the calculated toxicity IC_{50} was at 7.7 µM (Figure 4-30A) and for analog **5-15** IC_{50} at 14.5 µM, unfortunately in the same range as their antimicrobial activity. It is interesting that analog **5-15**, in all three replicates, had very steep dose response curve. At 12.5 µM the viability of the cells is almost 100%, however at the next step, at 25 µM, the viability is essentially 0% (Figure 4-30C). This unusual steep mode of action was not observed in any other analogs all the assays. Generally, three possible explanation of the steep dose-response curve are suggested: high enzyme K_d, multiple binding sides in the enzyme and the inhibitors phase transition [199]. Considering that the same enzymes are involved in the assay and the ligands from the same series should have the same mode of action, the third option involving phase transition is the most probable. The third tested compound, analog **5-8** had quite low toxicity, IC_{50} = 194 µM, approaching at the limit of the

assay and the solubility of the compound. Toxicity of analog **5-8** is almost the triple of its antimicrobial activity, MIC_{50} = 75.8 μM, thus having a more favourable safety window (Figure 4-30C). Despite analog **5-8** being the least active compound and only three compounds tested from this series of analogs, it gives us confidence to be able to design the next generation of analogs with high antimicrobial activity and improved safety window.

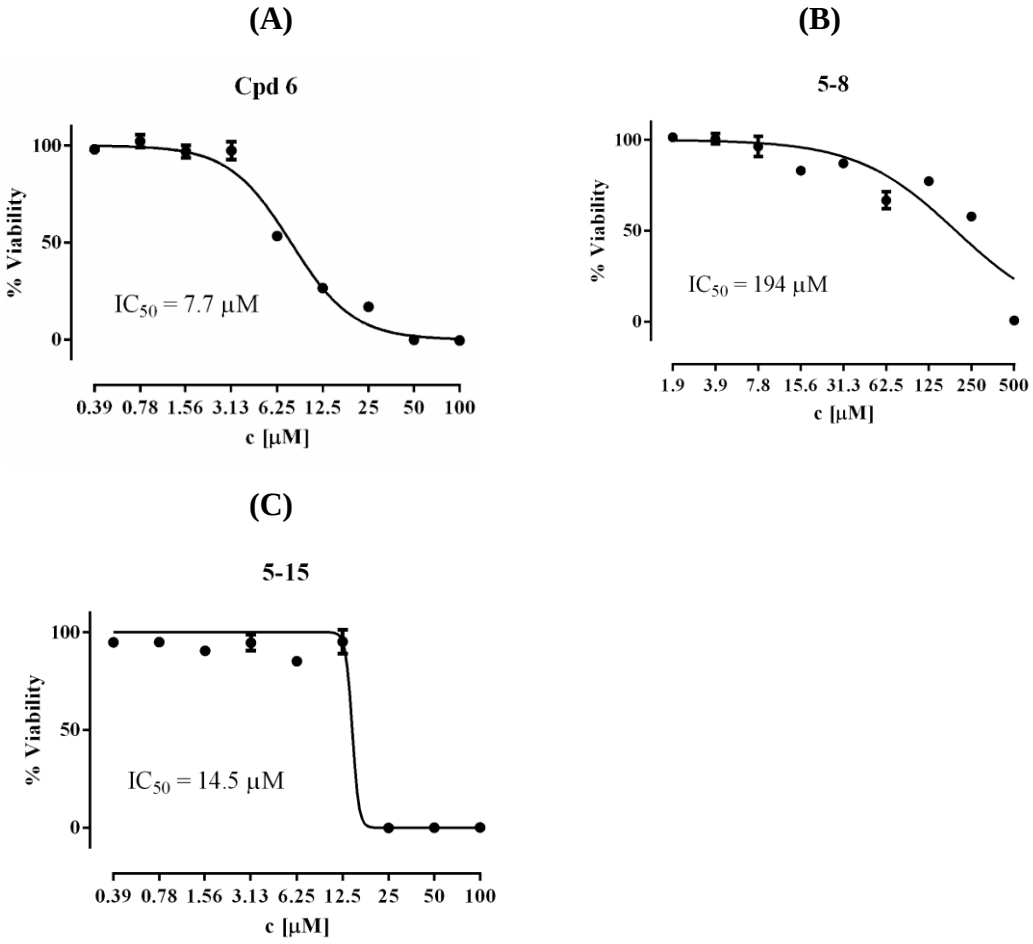

Figure 4-30: Toxicity of the compound 6 (A), analogs **5-8** (B) and analogs **5-15** (C).

Discussion

5. Discussion

Tuberculosis, being one of the leading pathogens that results in high mortality, requires long term drug therapy to completely eliminate *Mtb* infection. Despite the declining rates in TB infections, there are still various challenges in TB treatment. For almost a century, there has been only one available TB vaccination: BCG, which still possesses various limitations, such as the waning of the vaccination in adolescents and young adults. In addition, the increment in drug resistance towards currently utilized first and second line drugs provides a challenge towards the complete elimination of TB. In contrast to targeting cell wall biosynthesis and/or protein synthesis, a new target towards *Mtb* was recently found. *Mtb* is able to move from an active state, to a dormant state. In dormancy, *Mtb* has also been shown to produce a specific type-II NADH:ubiquinone oxidoreductase that is absent in humans. This has motivated researchers to find specific targets in the respiratory chain, such as F_1F_0 ATP synthase. In this study, molecular modelling and docking studies have led to the identification of a compound, cpd 6, that is capable of inhibiting the ATP synthesis and hydrolysis.

5.1 Identification of the hit compound

The high-resolution structure of mycobacterial F_1F_0 ATP synthase is not available, therefore the homology model had to be build. Although the size and complexity of the F_1F_0 ATP might lower the quality of the homology model, the structure of the key feature, the γ-loop from *Mtb*, was previously solved by NMR by Dr. Priya Ragunathan from our lab. Subsequent pharmacophore modelling and docking identified the top scoring ligands, of which 81 were tested for growth inhibition of *M. smegmatis*. Two compounds inhibited growth at the concentration of 50 μM. Cpd 2-3 was eliminated when tested against a dose-response curve. The inconsistent results observed from the inhibition of growth strongly suggests that cpd 2-3 may not be stable over time. With these results, it is probable that the expected concentration of cpd 2-3 may not be consistent in the systemic circulation, and as such, this study does not consider further investigation into cpd 2-3. Cpd 6 exhibited good inhibition MIC_{50} of 11 μM and was retained for further biochemical characterisation. The inhibition of the ATP hydrolysis by cpd 6 was comparable to known ATPase inhibitors, and the ATP

synthesis inhibition in IMVs reached the submicromolar range, with IC_{50} of 0.3 μM.

Although the potency of the cpd 6 is not in the nanomolar range as with the potency of Q203 or BQD, it was demonstrated that using the combination of cpd 6 with either BDQ and Q203 resulted in an additive effect. Inhibiting the respiratory chain by several different mechanisms could lower the risk of developing the resistance, or shorten the time needed to target the dormant bacteria. Moreover, the use of the combination of drugs is well in line with the current multidrug TB regimen.

5.2 Role of the unique $\gamma_{166\text{-}179}$ loop

The role of the γ-loop in the regulation of the ATP synthesis was investigated by comparing the ATP synthesis and hydrolysis between WT and $\Delta\gamma_{166\text{-}179}$ IMVs. IMVs with deletion of the γ-loop increased the ATP hydrolysis rate; however, the ATP synthesis drop to half compared to the WT. Moreover, the $\Delta\gamma_{166\text{-}179}$ mutant was more sensitive to the inhibition by BDQ, lowering the ATP synthesis IC_{50} of the BDQ 10-fold.

This demonstrates that the deletion of the $\Delta\gamma_{166\text{-}179}$ in *M. smegmatis* F-ATP synthase increases the accessibility of BDQ, and that this loop maybe in proximity to the additional binding site of γε and *c*-ring interface as mentioned recently [20]. The increase in ATP hydrolysis driven H^+-pumping and reduced ATP-formation by the IMV's of the $\Delta\gamma_{166\text{-}179}$ mutant protein presented, may imply that ATP synthesis may not simply be the reversal of ATP hydrolysis or at least may differ in minor point(s), as described for F-ATP synthases of mitochondrial particles [23,30] or liposomes of co-reconstituted bacteriorhodopsin and *Geobacillus stearothermophilus* F-ATP synthase [31]. It may be speculated that the unique 13-residue loop of mycobacterial F-ATP synthases may block the relative rotation of the γε-rotor relative to the *c*-ring, by its interaction with the *c*-ring loop, and that the energy provided by the low ATP hydrolysis activity of the fast-growing *M. smegmatis* presented and described recently [12], is not sufficient to unlock the inhibitory loop-loop interaction.

However, in case of the cpd 6, the inhibition of the ATP synthesis remained the same for both the WT and the $\Delta\gamma_{166\text{-}179}$ mutant. As shown in the schematic map of the cpd 6 docked at the binding site (Figure 5-1), the main interactions are coming from the *c*-ring and bottom globular part of the γ subunit. The interaction between E212 and amines from the cpd 6 especially seems to be the key for the binding. This is further supported by the experimental data, in which the secondary amine in the pyrimidine ring was disubstituted, resulting in the significant decrease in MIC_{50} and IC_{50}.

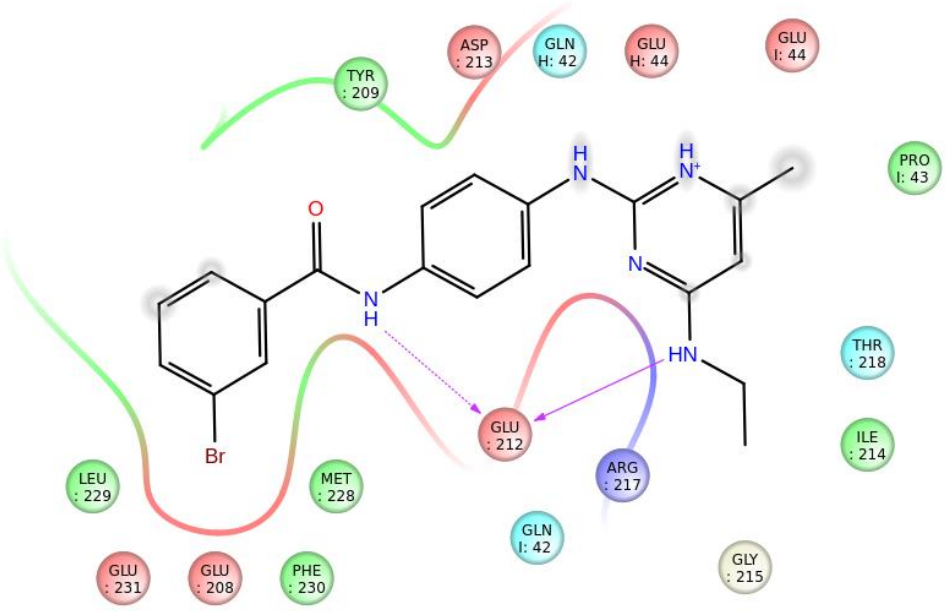

Figure 5-1: Schematic map of the cpd 6 docked at the binding site at the interface of the γ subunit and the *c*-ring. All the main interactions involved the amino acid residues from the globular bottom part of the γ subunit.

As discussed above, the hypothesised binding site of the cpd 6 is in the interface of the γ subunit and *c*-ring, which might be involved in the regulation of the ATP synthesis and hydrolysis, via the loop-loop interaction. Binding of the cpd 6 might block the interaction directly, or indirectly, by reducing the flexibility of the of the loops. This is illustrated in the Figure 5-2, where cpd 6 docked at the binding site, locks in the groove formed between the γ subunit and the *c*-ring.

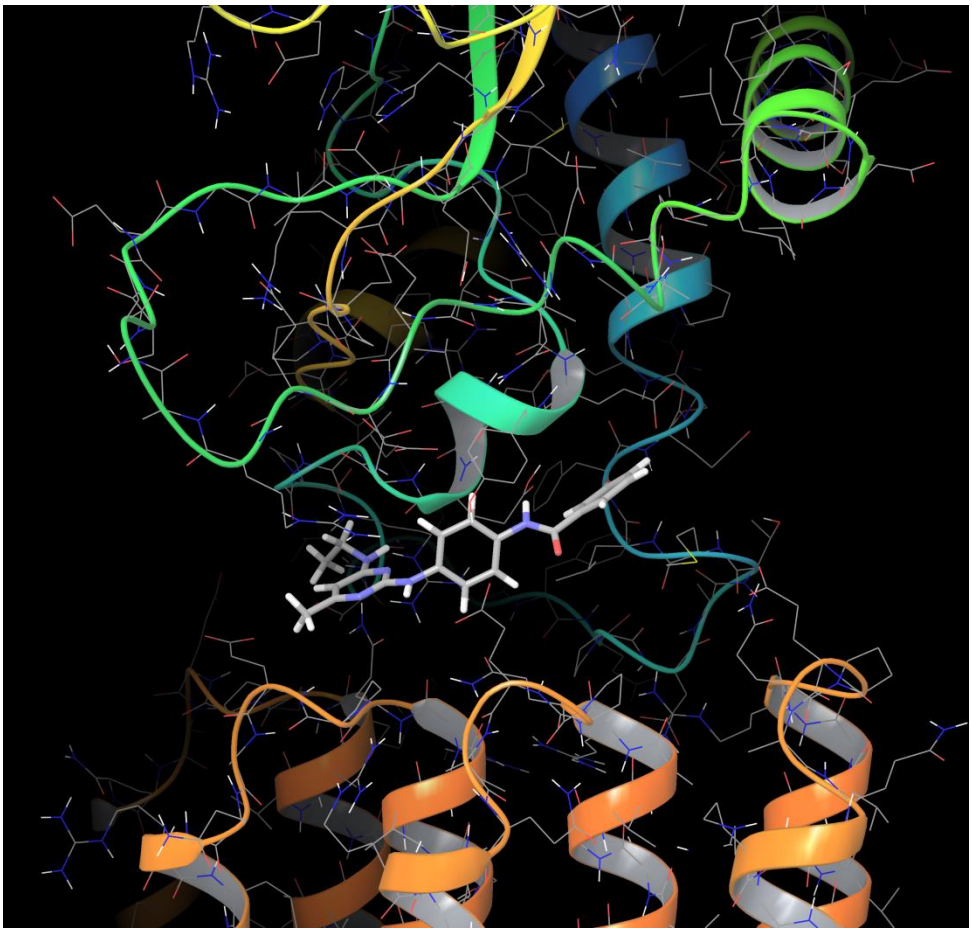

Figure 5-2: Compound 6 docked at the binding site at the interface of the *c*-ring and γ subunit.

Overall, this workflow, that includes modelling, ligand screening, validation and synthesis of the analogs could be followed to target and exploit other unique features of the mycobacterial F-ATP synthase, such as 36-amino acid C-terminal domain of the subunit α [200] or tryptophan 16 residue from the subunit ε [201], reported by our lab.

5.3 Structure-activity relationship

In the structure-activity relationship study, the effect of different substituents on the benzoic acid, various alkylamines, and methyl substituted on the pyrimidine ring was examined. In general, substitutions on the benzoic acid ring are well tolerated in the ATP synthesis assays; however, these compounds have lower antimicrobial activity. The pyrimidine ring can be modified without significantly raising IC_{50} and MIC_{50} by moving the methyl substituent to position 5, or by completely removing it. The pyrimidine isomer analog cpd 6 iso also did not lose any activity. The presence of a disubstituted alkylamine moiety on

the pyrimidine ring resulted in a drop in the both inhibitory activities suggesting that a secondary amine is essential (Figure 5-3). Shortening of the alkyl amines (methyl), or adding an alcohol group are well tolerated. However bigger substituents (isopropyl, glycine ethyl ester) are not desired. Unfortunately, none of the analogs displayed higher activity than cpd 6.

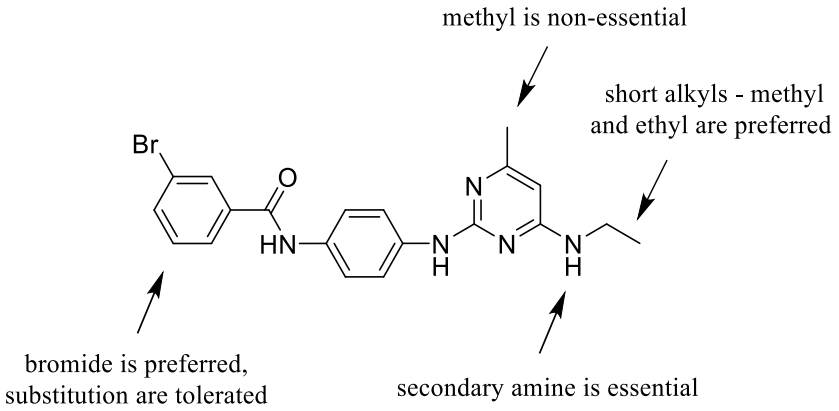

Figure 5-3: Structure-activity relationship of the cpd 6. The secondary amine on the pyrimidine ring is essential, substituted preferably by short alkyls such as methyl or ethyl. Methyl on the pyrimidine ring is non-essential, and therefore this position could be explored for the further substitution. Substituent on the benzamide ring are in general, well tolerated; however, the bromide is the most active.

5.4 Design of the next series of the compound 6

The synthesis for the cpd 6 and series was established in a convergent manner, that would allow the preparation of a diverse series of the analogs. In the next series of analogs, the role of the linker will be explored. We suggest using *m*-phenylenediamine, 5-member saturated or unsaturated rings, and adding the heteroatom to the ring to the geometry of the analogs as well as the distance between LHS and RHS. Furthermore, the use of various alkylamine linkers would provide a flexibility to the analogs (Figure 5-4, left).

In the current series, it was observed that the presence of secondary amine with a short alkyl, preferably ethyl, is required. Therefore, this will be conserved, and in the next series, the number and position of the nitrogen in the ring will be varied. Additionally, the ring closure to form an indole, which still possesses the secondary amine and spatially could overlap the cpd 6, was proposed (Figure 5-4, right). As the methyl position on the pyrimidine ring is non-essential, it can be replaced by chloride to provide an analog which could be further substituted easily.

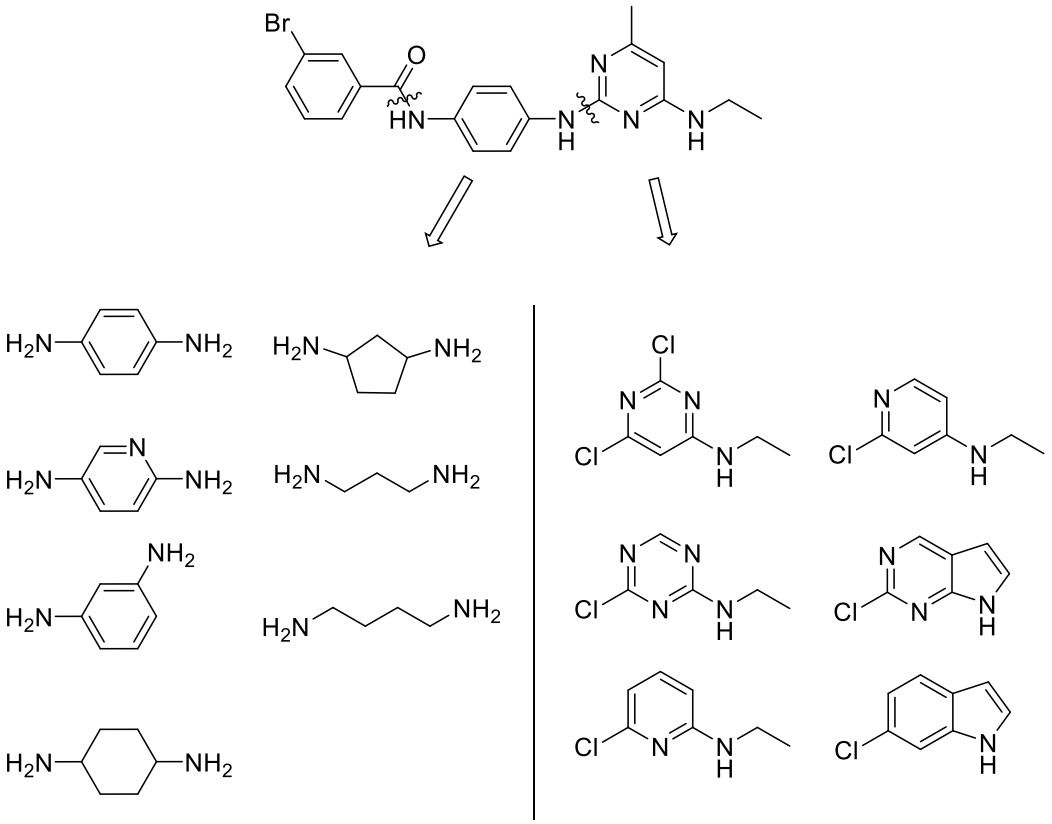

Figure 5-4: Next series of analogs to explore the structure-activity relationships of the linker (left) and pyrimidine ring (right)

Conclusion

6. Conclusion

To study the $\gamma_{165–178}$ loop, a newly identified drug target in the mycobacterial F_1F_O ATP synthase, the ATP synthesis and hydrolysis assays was successfully established. The ATP hydrolysis in *M. smegmatis* IMVs was observed and reported for the first time. Afterward, the role of the $\gamma_{165–178}$ loop was investigated by genomic deletion of the $\gamma_{165–178}$ loop. Interestingly, this deletion resulted in higher ATP hydrolysis rate compared to the WT, while the ATP synthesis dropped to almost a half of the wild type. This change was almost completely restored by the complementation and overexpression of the WT gene encoding the γ subunit. Hence, its hypothesised role in regulation of the ATP synthesis and hydrolysis was confirmed and therefore the $\gamma_{165–178}$ loop as a target for the design of the ATP synthase inhibitors was validated.

A homology model of the *Mtb* F_1F_O ATP synthase with the unique $\gamma_{165–178}$ loop was built. Interface of the *c*-ring, globular par of subunit γ and $\gamma_{165–178}$ loop was identified as a suitable docking site. A library of 1.5 million compounds was enriched by pharmacophore modelling and screening and subsequently submitted to docking using Glide module of the Maestro suite. Compounds were ranked by consensus scoring and best 81 commercially available compounds were tested for growth inhibition of *M. smegmatis* at the concentration of 50 μM. Cpd 6 was identified as a hit compound and was further characterised. Cpd 6 was able to inhibit the growth of *M. smegmatis* at 11 μM and the ATP synthesis in IMVs at 0.3 μM. Additionally, cpd 6 inhibited the oxygen consumption and the whole cell ATP synthesis. Moreover, cpd 6 displayed an additive effect when used in combination with BDQ or Q203.

A viable synthetic route for cpd 6 was proposed. This approach allowed us to synthesise cpd 6 in several grams scale with a high atom economy. Furthermore, series of the cpd 6 analogs was synthesised. The growth inhibition of *M. smegmatis* and ATP synthesis inhibition activity of the analogs were determined. Based on these results the simple structure-activity relationship was proposed, which will be used in the design of the next series of the analogs.

Experimental and supplementary data

7. Experimental and supplementary data

7.1 Chemistry

7.1.1 General procedures

General Procedure for Synthesis of 2-chloro-pyrimidin-4-amines (GP1):

The corresponding amine or amine hydrochloride and of 2,4-dichloro-6-methylpyrimidine (5.0 g, 30.7 mmol) with 2eq diisopropylethylamine were stirred for 24h in ethanol at 50°C. The solvent was evaporated and the isomers were separated with column chromatography using hexane:EtOAc 8:2. The correct isomer was identified by NOESY.

General Procedure for Synthesis of *N*-(4-nitrophenyl)benzamides (GP2):

To the corresponding benzoic acid (2 g) in dichloromethane (25 ml) was added dropwise oxalyl chloride (1.5 ml, 1.2 eq) in the presence of a catalytic amount of dimethylformamide. The mixture was stirred at RT for 1 h and then concentrated. 4-Nitroaniline (1eq) and K_2CO_3 (2eq) were added to the obtained material in THF (40 ml) and stirred for 16 h at RT. The product was filtered and washed with water and hexane.

General Procedure for Hydrogenation of *N*-(4-nitrophenyl)benzamides (GP3):

The corresponding *N*-(4-nitrophenyl)benzamide (0.5-2 g) with palladium on carbon (10% wt) in 20 ml of ethyl acetate and was hydrogenated under 50 psi of H_2 and stirred at RT for 3 h. The flask was depressurised, the reaction mixture was filtered through Celite, the solvent was evaporated to obtain the product.

General Procedure for Synthesis of *N*-(4-((4-aminopyrimidin-2-yl)amino)phenyl)-benzamides (GP4):

The corresponding *N*-(4-aminophenyl)benzamide (200 mg – 2 g) and 2-chloranylpyrimidin-4-amine (1eq) with *N*,*N*-Diisopropylethylamine (1eq) was heated at reflux in dioxane (4-20 ml) for 2-5 days. The reaction mixture was filtered and the product was obtained.

7.1.2 Experimental

3-acetoxybenzoic acid (1-1a)

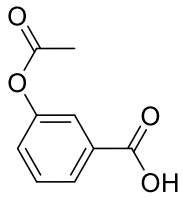

Acetic anhydride (10 ml, 105.79 mmol) was added dropwise to a cooled solution of 3-hydroxybenzoic acid (2 g, 14.48 mmol) in pyridine (20 ml), and the mixture was stirred at RT overnight. The mixture was cooled, poured onto ice and extracted with diethyl ether (50 ml). The product was obtained as a colourless solid (2.29 g, 88%). ^{1}H NMR (400 MHz, DMSO-d_6) δ 8.58 (s, J = 4.1 Hz, 1H), 7.83 (d, J = 7.9 Hz, 2H), 7.66 (s, J = 2.0 Hz, 2H), 7.55 (t, J = 7.9 Hz, 2H), 7.39 (d, J = 6.7 Hz, 3H), 2.29 (s, J = 1.9 Hz, 6H);[1] ^{13}C NMR (100 MHz, DMSO-d_6) δ 169.7, 167.0, 151.0, 132.7, 130.3, 127.1, 126.9, 123.1, 21.3.[1]

3-((4-nitrophenyl)carbamoyl)phenyl acetate (1-1)

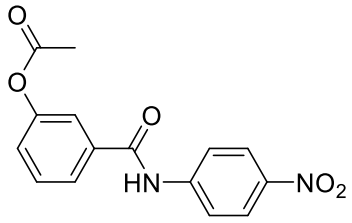

The product was prepared according to the GP2 from **1-1a** (2.29 g, 12.71 mmol) and 4-nitroaniline (1.75 g 12.69 mmol). The product was obtained as colourless solid (3.41g, 90%). ^{1}H NMR (400 MHz, DMSO-d_6) δ 10.86 (s, 1H), 8.28 (d, J = 9.3 Hz, 2H), 8.07 (d, J = 9.3 Hz, 2H), 7.90 (d, J = 7.9 Hz, 1H), 7.75 (s, 1H), 7.62 (t, J = 7.9 Hz, 1H), 7.42 (d, J = 5.9 Hz, 1H), 2.32 (s, 3H);^{13}C NMR (100 MHz, DMSO-d_6) δ 169.7, 165.7, 150.9, 145.8, 143.1, 136.1, 130.2, 126.3, 125.9, 125.3, 121.8, 120.4, 21.3; FTIR (nujol, cm^{-1}) υ_{max} 3562, 1730, 1674, 752; mp: 173-175°C

3-((4-aminophenyl)carbamoyl)phenyl acetate (2-1a)

[1] Spectrum in accordance with: Kesenheimer, C., A. Kalogerakis, A. Meissner and U. Groth (). *Chemistry*, **2010**, **16**(29): 8805-8821.

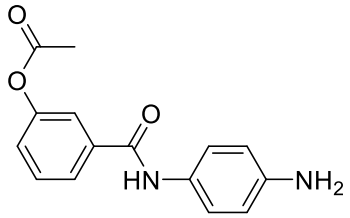

1-1 (2g, 6.66 mmol) was hydrogenated according to GP3. The product was obtained as a yellow solid (1.44 g, 5.33 mmol), yield 80%. ^{1}H NMR (400 MHz, DMSO-d_6) δ 9.94 (s, 1H), 7.85 (d, J = 7.9 Hz, 1H), 7.69 (s, 1H), 7.55 (t, J = 7.9 Hz, 1H), 7.39 (d, J = 8.7 Hz, 1H), 7.33 (d, J = 8.1 Hz, 1H), 6.57 (d, J = 8.7 Hz, 1H), 4.93 (s, 2H), 2.31 (s, 1H); ^{13}C NMR (100 MHz, DMSO-d_6) δ 169.7, 164.0, 150.9, 145.8, 137.2, 129.9, 128.4, 125.3, 125.2, 122.8, 122.6, 121.4, 114.2, 21.2, 14.5; FTIR (nujol, cm^{-1}) υ_{max} 1737, 1651, 823; mp: 231-233°C

***N*-(4-aminophenyl)-3-hydroxybenzamide (2-1)**

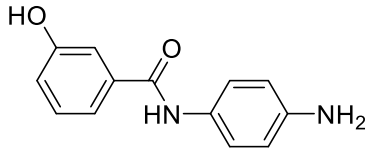

2-1a (635 mg, 2.35 mmol) was dissolved in 30 mL of ethanol and cooled to 0°C. After addition of 2M aqueous NaOH (15 mL), the solution was stirred for 1 h, glacial acetic acid was added until the pH was < 7, the solvents were evaporated and the product was obtained as a yellow solid (491 mg, 92%). ^{1}H NMR (396 MHz, DMSO-d_6) δ 9.77 (s, 1H), 9.67 (s, 1H), 7.46 – 7.18 (m, 5H), 6.93 (d, J = 7.8 Hz, 1H), 6.54 (d, J = 6.9 Hz, 2H), 4.92 (s, 1H);[2] ^{13}C NMR (100 MHz, DMSO-d_6) δ 165.2, 157.8, 145.6, 137.3, 129.8, 128.7, 122.6, 118.5, 118.4, 114.9, 114.1.[2]

3-bromo-*N*-(4-nitrophenyl)benzamide (1-2)

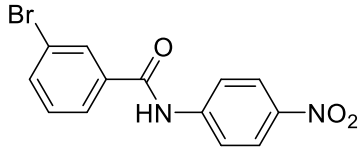

The product was prepared according to the GP2 with 3-bromobenzoic acid (8.77 g, 43.63 mmol) in dichloromethane (25 ml). p-nitroaniline (6.0 g, 43.63 mmol)

[2] Spectrum in accordance with: Tran, A. T., D. Wen, N. P. West, E. N. Baker, W. J. Britton and R. J. Payne. *Org Biomol Chem,* **2013 11**(46): 8113-8126.

and K_2CO_3 (12.0 g, 2 eq). The product was obtained as a yellow solid (13.74 g, 98%). ^{1}H NMR (400 MHz, DMSO-d_6) δ 10.84 (s, 1H), 8.24 (d, *J* = 9.3 Hz, 2H), 8.14 (s, *J* = 1.8 Hz, 1H), 8.02 (d, *J* = 9.3 Hz, 2H), 7.94 (d, *J* = 7.9 Hz, 1H), 7.81 (d, *J* = 8.9 Hz, 1H), 7.50 (t, *J* = 7.9 Hz, 1H); ^{13}C NMR (100 MHz, DMSO-d_6) δ 165.6, 147.6, 142.5, 137.7, 134.9, 131.1, 127.7, 125.2, 122.1, 120.8. HRMS calcd for $C_{13}H_{10}BrN_2O_3$ (M^++ H^+) 320.9875; found 320.9907 (10 PPM) FTIR (nujol, cm^{-1}) υ_{max} 1685, 1400, 800, 750, 596; Mp: 191-195°C

***N*-(4-aminophenyl)-3-bromobenzamide (2-2)**

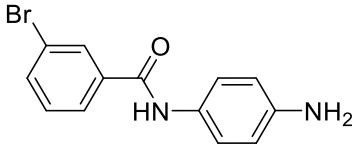

1-2 (2.5 g, 7.79 mmol) was hydrogenated in 25 ml of EtOAc with sulfur poisoned platinum on carbon (10% wt), for two days under 100 psi of H_2 at 100°C. The mixture was filtered through Celite and the solvent was evaporated under reduced pressure. The product was obtained as a grey solid (yield 99%). ^{1}H NMR (400 MHz, DMSO-d_6) δ 9.97 (s, 1H), 8.10 (s, 1H), 7.92 (d, *J* = 7.8, 0.9 Hz, 1H), 7.75 (d, 1H), 7.47 (dd, *J* = 7.9 Hz, 1H), 7.36 (d, *J* = 8.7 Hz, 2H), 6.61 – 6.43 (m, 2H), 4.95 (s, 2H). ^{13}C NMR (100 MHz, DMSO-d_6) δ 163.5, 145.9, 138.0, 134.3, 131.0, 130.5, 128.2, 127.1, 122.7, 122.1, 114.1; FTIR (nujol, cm^{-1}) υ_{max} 1643, 1262, 821; MS (ESI+) m/z 291 (^{79}Br M^+ + H^+, 100), 293 (^{81}Br M^++ H^+, 94); HRMS calcd for $C_{13}H_{12}{}^{79}BrN_2O$ (M^++ H^+) 291.0133; found 291.0133 (2.1 PPM); mp: 145-146°C

***N*-(4-nitrophenyl)benzamide (1-3)**

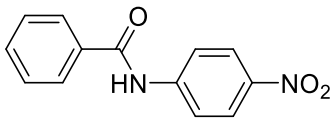

The product was prepared according to the GP2 from benzoyl chloride (1.1g, 1.21 ml, 7.6 mmol) and *p*-nitroaniline (1.0 g, 7.2 mmol). The product was obtained as ayellow solid (886 mg, 48%). ^{1}H NMR (400 MHz, DMSO-d_6) δ 10.81 (s, 1H), 8.28 (d, *J* = 9.2 Hz, 2H), 8.07 (d, *J* = 9.3 Hz, 2H), 7.98 (d, *J* = 7.0

Hz, 2H), 7.65 (t, *J* = 7.3 Hz, 1H), 7.57 (t, *J* = 7.4 Hz, 2H);[3] ^{13}C NMR (100 MHz, DMSO-d_6) δ 166.8, 146.2, 142.9, 134.8, 132.6, 129.0, 128.4, 125.3, 120.3.[3]

***N*-(4-aminophenyl)benzamide (2-3)**

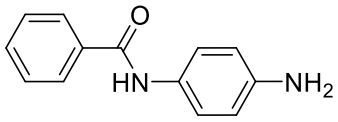

3-1 (886 mg) was hydrogenated according to the GP3. The product was obtained as a grey solid (765 mg, 99%). ^{1}H NMR (400 MHz, DMSO-d_6) δ 9.87 (s, 1H), 7.92 (d, *J* = 7.0 Hz, 2H), 7.62 – 7.44 (m, 3H), 7.38 (d, *J* = 8.7 Hz, 2H), 6.56 (d, *J* = 8.7 Hz, 2H), 4.92 (s, 2H);[4] ^{13}C NMR (100 MHz, DMSO-d_6) δ 165.2, 145.7, 135.8, 131.6, 128.8 (2C), 128.6, 127.9 (2C), 122.7 (2C), 114.2 (2C).[4]

3-fluoro-*N*-(4-nitrophenyl)benzamide (1-4)

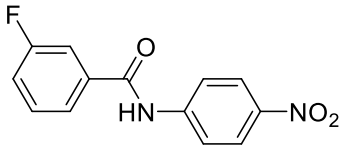

The product was prepared according to the GP2 from 3-florobenzoic acid (1.0 g, 7.14 mmol), *p*-nitroaniline (1.0 g, 7.2 mmol). The product was obtained as a yellow solid (1.37 g, 69%). ,^{1}H NMR (396 MHz, DMSO-d_6) δ 10.86 (s, 1H), 8.24 (d, *J* = 9.2 Hz, 2H), 8.01 (d, *J* = 9.3 Hz, 2H), 7.85 (d, *J* = 7.8 Hz, 1H), 7.81 (d, 1H), 7.60 (td, *J* = 8.0, 6.0 Hz, 1H), 7.46 (td, *J* = 8.4, 2.2 Hz, 1H); ^{13}C NMR (100 MHz, DMSO-d_6) δ 165.9 (s), 162.42 (d, J = 244.2 Hz), 147.89 (s), 142.4 (s), 138.1 (d, J = 6.4 Hz), 131.0 (d, J = 8.0 Hz), 125.3 (s), 124.7 (d, J = 2.3 Hz), 120.9 (s), 119.2 (d, J = 21.0 Hz), 115.3 (d, J = 22.7 Hz); FTIR (nujol, cm^{-1}) υ_{max} 1610, 1344, 1193, 752; mp: 174-175°C

***N*-(4-aminophenyl)-3-fluorobenzamide (2-4)**

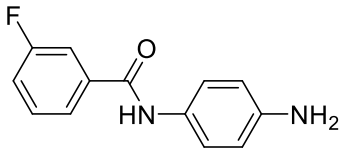

1-4 (857 mg, 3.29 mmol) was hydrogenated according to the GP3. The product was obtained as grey solid (754 mg, 99%). ^{1}H NMR (396 MHz, DMSO-d_6) δ

[3] Spectrum in accordance with: Panda, N., R. Mothkuri and D. K. Nayak. *European Journal of Organic Chemistry*, **2014**(8): 1602-1605.
[4] Spectrum in accordance with: Wang, J., X. Yin, J. Wu, D. Wu and Y. Pan. *Tetrahedron*, **2013**, **69**(48): 10463-10469.

9.93 (s, 1H), 7.78 (d, *J* = 7.8 Hz, 1H), 7.72 (d, *J* = 9.9 Hz, 1H), 7.55 (td, *J* = 8.0, 6.0 Hz, 1H), 7.45 – 7.38 (m, 1H), 7.36 (d, *J* = 8.7 Hz, 2H), 6.55 (d, *J* = 8.8 Hz, 2H), 4.95 (s, 2H); ^{13}C NMR (100 MHz, DMSO-d_6) δ 163.7 (d, J = 2.3 Hz), 162.5 (d, J = 244.1 Hz), 146.0 (s), 138.2 (d, J = 6.9 Hz), 131.0 (d, J = 8.0 Hz), 128.3 (s), 124.2 (d, J = 2.9 Hz), 122.8 (s), 118.5 (d, J = 21.1 Hz), 114.8 (d, J = 22.6 Hz), 114.2 (s); FTIR (nujol, cm^{-1}) υ_{max} 1847, 1587, 1519, 1462, 1377, 1317, 1244, 1199, 1097, 1014, 898, 815, 750, 653, 520, 478; mp: 112-114°C

4-methyl-*N*-(4-nitrophenyl)benzamide (1-5)

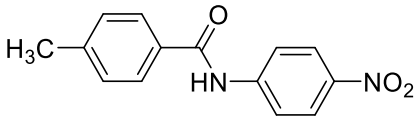

The product was prepared according to the GP2 from 4-methylbenzoic acid (2 g, 14.69 mmol) and *p*-nitroaniline (2.0 g, 14.49 mmol). The product was obtained as a yellow solid (2.52 g, 67%). ^{1}H NMR (396 MHz, DMSO-d_6) δ 10.71 (s, 1H), 8.26 (d, *J* = 9.2 Hz, 2H), 8.07 (d, *J* = 9.3 Hz, 2H), 7.90 (d, *J* = 8.2 Hz, 2H), 7.37 (d, *J* = 8.1 Hz, 2H), 2.40 (s, 3H); ^{13}C NMR (100 MHz, DMSO-d_6) δ 166.5, 146.1, 142.9, 131.8, 129.5, 128.5, 125.3, 120.3, 21.5; MS (ESI+) m/z 257 ($M^+ + H^+$); HRMS calcd for $C_{14}H_{13}N_2O_3$ ($M^+ + H^+$) 257.0926; found 257.0945 (7.4 PPM); FTIR (nujol, cm^{-1}) υ_{max} 1672, 1336, 1178, 1109, 848; Mp: 205-207°C

***N*-(4-aminophenyl)-4-methylbenzamide (2-5)**

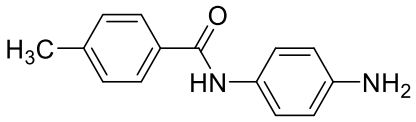

1-5 (2g, 6.66 mmol) was hydrogenated according to GP3. The product was obtained as yellow solid (1.44 g, 98%). ^{1}H NMR (400 MHz, DMSO-d_6) δ 9.77 (s, 1H), 7.83 (d, *J* = 8.1 Hz, 2H), 7.36 (d, *J* = 8.7 Hz, 2H), 7.30 (d, *J* = 8.0 Hz, 1H), 6.54 (d, *J* = 8.7 Hz, 1H), 4.91 (s, 2H), 2.37 (s, 3H); ^{13}C NMR (100 MHz, DMSO-d_6) δ 164.9, 145.6, 141.4, 132.8, 129.3, 128.6, 127.9, 122.7, 114.1, 21.5.; MS (ESI+) m/z 227 ($M^+ + H^+$); HRMS calcd for $C_{14}H_{15}N_2O$ ($M^+ + H^+$) 227.1184; found 227.1190 (2.6 PPM); FTIR (nujol, cm^{-1}) υ_{max} 1639, 1612, 1327, 833; mp: 141-144°C

4-methoxy-*N*-(4-nitrophenyl)benzamide (1-6)

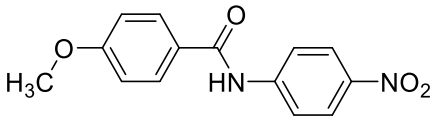

The product was prepared according to the GP2 from 4-methoxybenzoic acid (2 g, 13.15 mmol) and *p*-nitroaniline (1.81 g 13.13 mmol). Product was obtained as yellow solid (2.76 g, 77%). ^{1}H NMR (400 MHz, DMSO-d_6) δ 10.64 (s, 1H), 8.25 (d, *J* = 9.2 Hz, 1H), 8.06 (d, *J* = 9.2 Hz, 1H), 7.99 (d, *J* = 8.8 Hz, 1H), 7.09 (d, *J* = 8.9 Hz, 1H), 3.85 (s, 3H).; ^{13}C NMR (100 MHz, DMSO-d_6) δ 166.0, 162.9, 146.3, 142.7, 130.5, 126.9, 126.6, 125.3, 120.2, 114.3, 112.9, 56.0; MS (ESI+) m/z 273 (M^+ + H^+); HRMS calcd for $C_{14}H_{13}N_2O_4$ (M^++ H^+) 273.0875; found 257.0905 (11.0 PPM); FTIR (nujol, cm^{-1}) υ_{max} 1651, 1184, 848, 455; mp: 173°C

***N*-(4-aminophenyl)-4-methoxybenzamide (2-6)**

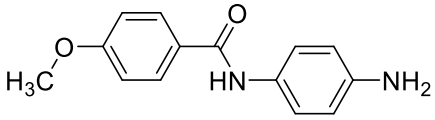

1-6 (1g, 3.67 mmol) was hydrogenated according to GP3. The product was obtained as a grey solid (870 mg, 98%)[5]. ^{1}H NMR (400 MHz, DMSO-d_6) δ 9.71 (s, 1H), 7.91 (d, *J* = 8.7 Hz, 2H), 7.35 (d, *J* = 8.7 Hz, 2H), 7.03 (d, *J* = 8.8 Hz, 2H), 6.53 (d, *J* = 8.7 Hz, 2H), 4.89 (s, 2H), 3.83 (s, 3H); ^{13}C NMR (100 MHz, DMSO-d_6) δ 164.6, 162.0, 145.5, 129.7, 128.7, 127.9, 122.8, 114.1, 113.9, 55.9.**2,4-dichloro-5-methylpyrimidine (3-1)**

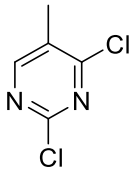

6-Methyluracyl (1 g, 7.93 mmol) was added to phosphoryl chloride (7 eq., 5 ml) and the mixture was heated at reflux for 3 h. The mixture was poured onto ice and the organic layer was extracted by chloroform (3 x 20 ml) and dried over anhydrous $MgSO_4$. The solvents were evaporated to give the dichloride as yellow crystals (0.62 g, 48%). ^{1}H NMR (400 MHz, $CDCl_3$) δ 8.35 (s, 1H), 2.39(s, 3H);[6] ^{13}C NMR (100 MHz, $CDCl_3$) δ 162.5, 160.0, 158.2, 129.1, 15.8.

2,4-dichloro-6-methylpyrimidine (3-2)

[5] Compound reported in EP2505198, 2012,

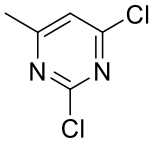

6-Methyluracyl (5 g, 39.65 mmol) was added to phosphoryl chloride (7 eq., 25 ml) and the mixture was heated at reflux for 3 h. The mixture was poured onto ice and the organic layer was extracted with chloroform (3 x 20 ml) and dried over anhydrous $MgSO_4$. The solvents were evaporated to give the dichloride as yellow crystals (3.77 g, 58%). ^{1}H NMR (400 MHz, $CDCl_3$) δ 7.19 (s, 1H), 2.55 (s, 3H)[6];^{13}C NMR (100 MHz, $CDCl_3$) δ 171.8, 162.4, 160.4, 119.5, 23.8.

(2-chloro-5-methyl-pyrimidin-4-yl)-ethylamine (4-1)

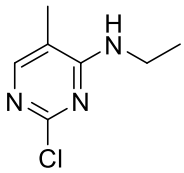

The product was prepared according to the GP1 with ethylamine hydrochloride (500 mg, 6.13 mmol) and 2,4-dichloro-5-methylpyrimidine **3-1** (1.0 g, 6.13 mmol). The product (575 mg, 56%) was obtained as white crystals. ^{1}H NMR (400 MHz, $CDCl_3$) δ 7.80 (s, 1H), 4.69 (s, 1H), 3.56 (qd, *J* = 7.2, 5.5 Hz, 2H), 2.00 (s, 3H), 1.27 (t, *J* = 7.2 Hz, 3H); ^{13}C NMR (100 MHz, $CDCl_3$) δ 162.2, 158.8, 154.6, 111.7, 36.1, 14.7, 13.0; MS (ESI+) 172 (^{35}Cl M^+ + H^+, 100), 174 (^{37}Cl M^++ H^+, 37); HRMS calcd for $C_7H_{11}N_3Cl$ (M^++ H^+) 172.0642; found 172.0638 (-2.3 PPM); FTIR (nujol, cm^{-1}) υ_{max} 1244, 1097, 665; 58-63°C

2-chloranyl-*N*-ethyl-6-methyl-pyrimidin-4-amine (4-2a)

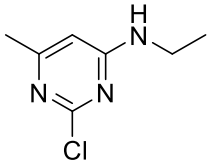

The product was prepared according to the GP1 with ethylamine hydrochloride (2.5g, 30.67mmol) and **3-2** (5.0 g, 30.67mmol). The desired isomer was obtained as yellow crystals (1.74 g, 33%). ^{1}H NMR (400 MHz, $CDCl_3$) δ 6.07 (s, 1H), 5.10 (br, 1H), 3.33 (br, 2H), 2.33 (s, 3H), 1.30 – 1.21 (m, 3H); ^{13}C NMR (100 MHz, $CDCl_3$) δ 166.7, 162.2, 160.2, 99.3, 42.4, 23.9, 12.6; MS (ESI+) m/z 172

[6] Spectrum in accordance with: Wang, H., K. Wen, L. Wang, Y. Xiang, X. Xu, Y. Shen and Z. Sun (2012). *Molecules.* **2012,** 17(4), 4533-4544.

(^{35}Cl $M^+ + H^+$, 100), 174 (^{37}Cl $M^+ + H^+$, 31); HRMS calcd for $C_7H_{11}N_3{}^{35}Cl$ ($M^+ + H^+$) 172.0642; found 172.0649 (4.1 PPM); FTIR (nujol, cm^{-1}) υ_{max} 3250, 1600, 968; mp: 74-75°C

4-chloro-*N*-ethyl-6-methylpyrimidin-2-amine (4-2b)

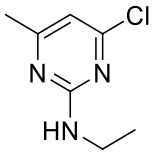

Yield 14%

^1H NMR (400 MHz, $CDCl_3$) δ 6.43 (s, 1H), 5.09 (s, 1H), 3.44 (qd, J = 7.2, 5.8 Hz, 2H), 2.30 (s, 3H), 1.21 (t, J = 7.2 Hz, 3H).

2-chloro-*N*-isopropyl-6-methylpyrimidin-4-amine (4-3a)

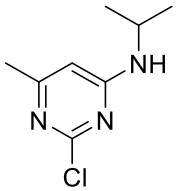

The product was prepared according to the GP1 with isopropylamine (1.09 g, 1.58 ml, 18.40 mmol) and **3-2** (3.0 g, 18.40 mmol). The desired isomer was obtained as a yellow oil (1.81 mg, 53%). ^1H NMR (400 MHz, $CDCl_3$) δ 6.05 (s, 1H), 4.99 (br, 1H), 3.92 (br, 1H), 2.31 (s, 3H), 1.24 (t, *J* = 6.3 Hz, 6H); ^{13}C NMR (100 MHz, $CDCl_3$) δ 163.2, 160.3, 43.1, 23.7, 22.5; MS (ESI+) m/z 186 (^{35}Cl $M^+ + H^+$, 100), 188 (^{37}Cl $M^+ + H^+$, 51); HRMS calcd for $C_8H_{13}N_3{}^{35}Cl$ ($M^+ + H^+$) 186.0798; found 186.0794 (-2.1 PPM); FTIR (neat, cm^{-1}) υ_{max} 3263, 1600, 968

4-chloro-*N*-isopropyl-6-methylpyrimidin-2-amine (4-3b)

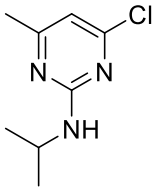

Yield 46%

^1H NMR (400 MHz, $CDCl_3$) δ 6.42 (s, 1H), 5.06 (s, 1H), 2.56 (s, 3H), 2.30 (s, 3H), 1.22 (d, *J* = 6.4 Hz, 6H).

2-chloro-*N,N*-diethyl-6-methylpyrimidin-4-amine (4-4a)

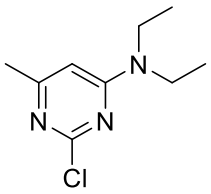

The product was prepared according to the GP1 with diethylamine (244 mg, 3.07 mmol) and **3-2** (500 mg, 3.07 mmol). The desired isomer was obtained as a yellow oil (25 mg, 4%). ^{1}H NMR (400 MHz, $CDCl_3$) δ 6.32 (s, 1H), 3.57 (q, *J* = 7.1 Hz, 4H), 2.27 (s, 3H), 1.16 (t, *J* = 7.1 Hz, 6H). ^{13}C NMR (100 MHz, $CDCl_3$) δ 168.9, 161.0, 160.7, 107.2, 41.8, 24., 13.03 (1.92); MS (ESI+) m/z 200 (^{35}Cl $M^+ + H^+$, 100), 202 (^{37}Cl $M^+ + H^+$, 55); HRMS calcd for $C_9H_{15}N_3{}^{35}Cl$ ($M^+ + H^+$) 200.0955; found 200.0965 (5.0 PPM); FTIR (neat, cm^{-1}) υ_{max} 3427, 1589, 1047, 445

4-chloro-*N,N*-diethyl-6-methylpyrimidin-2-amine (4-4b)

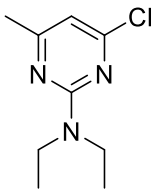

Yield 65%

^{1}H NMR (400 MHz, $CDCl_3$) δ 6.11 (s, 1H), 3.49 (br, 4H), 2.32 (s, 3H), 1.19 (t, *J* = 7.1 Hz, 6H).

ethyl (2-chloro-6-methylpyrimidin-4-yl)glycinate (4-5a)

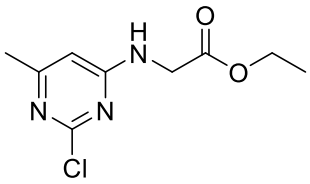

The product was prepared according to the GP1 with glycine ethyl ester hydrochloride (244 mg, 3.07 mmol) and **3-2** (500 mg, 3.07 mmol) (hexane:EtOAc 1:1). Minor 2-substituted isomer was identified by x-ray crystallography. The desired isomer was obtained as colourless crystals (338 mg, 48%). ^{1}H NMR (396 MHz, $CDCl_3$) δ 6.50 (s, 1H), 5.59 (br, 1H), 4.22 (q, *J* = 7.1 Hz, 2H), 4.18 (d, *J* = 5.5 Hz, 1H), 2.30 (s, 3H), 1.28 (t, *J* = 7.1 Hz, 3H); ^{13}C NMR (100 MHz, $CDCl_3$) δ 163.4, 160.3, 61.8, 42.9, 23.6, 14.2; HRMS calcd for $C_9H_{13}N_3O_2Cl$ ($M^+ + H^+$) 230.0696; found 230.0707(4.8 PPM); FTIR (nujol, cm^{-1}) υ_{max} 3250, 1732, 1622, 543; mp: 83-84°C

ethyl (4-chloro-6-methylpyrimidin-2-yl)glycinate (4-5b)

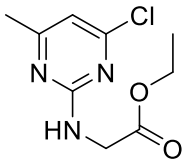

Yield 18%

^{1}H NMR (396 MHz, $CDCl_3$) δ 6.17 (s, 1H), 5.42 (s, 1H), 4.26 (q, *J* = 7.1 Hz, 2H), 4.16 (s, 2H), 2.34 (s, 3H), 1.31 (t, *J* = 7.1 Hz, 3H)

2-((2-chloro-6-methylpyrimidin-4-yl)amino)ethan-1-ol (4-6a)

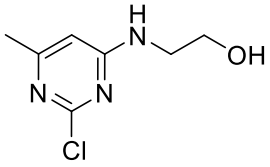

The product was prepared according to the GP1 with ethanolamine (374 mg, 6.13 mmol) and **3-2** (1.0 g, 6.13 mmol). The desired isomer was obtained as white crystals (311 mg, 27%). ^{1}H NMR (400 MHz, $CDCl_3$) δ 6.16 (s, 1H), 5.43 (br, 1H), 3.87 (dd, *J* = 9.9, 4.9 Hz, 2H), 3.58 (br, 2H), 2.36 (s, 3H); ^{13}C NMR (100 MHz, $CDCl_3$) δ 169.6, 162.5, 161.3, 109.6, 77.4, 77.1, 76.7, 44.4, 23.8; MS (ESI+) m/z 188 (^{35}Cl M^+ + H^+, 100), 190 (^{37}Cl M^++ H^+, 30); HRMS calcd for $C_7H_{10}N_3{}^{35}ClO$ (M^++ H^+) 188.0591; found 1588.0599 (4.3 PPM); FTIR (nujol, cm^{-1}) υ_{max} 3251, 1614, 1041, 765; mp: 127-128°C

2-((4-chloro-6-methylpyrimidin-2-yl)amino)ethan-1-ol (4-6b)

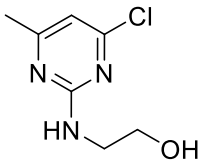

Yield 51 %

^{1}H NMR (400 MHz, $CDCl_3$) δ 6.49 (s, 1H), 5.59 (s, 1H), 3.82 (dd, *J* = 10.0, 4.8 Hz, 2H), 3.60 (dd, *J* = 10.0, 5.6 Hz, 2H), 2.32 (s, 3H).

2-chloro-*N*,6-dimethylpyrimidin-4-amine (4-7a)

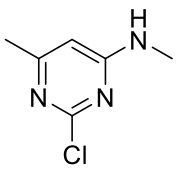

The product was prepared according to the GP1 with methanolamine (414 mg, 6.13 mmol) and **3-2** (1.0 g, 6.13 mmol). The desired isomer was obtained as

white crystals (415 mg, 43%). ^{1}H NMR (400 MHz, $CDCl_3$) δ 6.09 (s, 1H), 5.05 (br, 1H), 2.95 (d, *J* = 5.0 Hz, 3H), 2.35 (s, 3H); ^{13}C NMR (100 MHz, $CDCl_3$) δ 168.1, 165.0, 159.8, 98.4, 28.5, 23.9; MS (ESI+) m/z 158 (^{35}Cl $M^+ + H^+$, 100), 160 (^{37}Cl $M^+ + H^+$, 34); HRMS calcd for $C_6H_9N_3{}^{35}Cl$ ($M^+ + H^+$) 158.0485; found 158.0483 (-1.3 PPM); FTIR (nujol, cm^{-1}) υ_{max} 3257, 1614, 972, 835; mp: 134-135°C

4-chloro-*N*,6-dimethylpyrimidin-2-amine (4-7b)

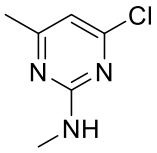

Yield 30%

^{1}H NMR (400 MHz, $CDCl_3$) δ 6.45 (s, 1H), 5.12 (br, 1H), 3.03 – 2.97 (m, 3H), 2.31 (s, 3H).

2-chloro-*N*-ethylpyrimidin-4-amine (4-8a)

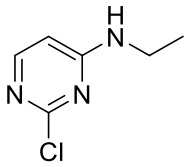

The product was prepared according to the GP1 with ethylamine hydrochloride (414 mg, 5.08 mmol) and 2,4-dichloropyrimidine (756 mg, 5.08 mmol). Product (332 mg, 63%) was obtained as white crystals. ^{1}H NMR (400 MHz, $CDCl_3$) δ 8.00 (s, 1H), 6.25 (d, J = 6.0 Hz, 1H), 5.50 (br, 1H), 3.36 (s, 2H), 1.25 (t, J = 7.2 Hz, 3H); ^{13}C NMR (100 MHz $CDCl_3$) δ 163.7, 160.2, 155.3, 105.5, 35.3, 14.5; MS (ESI+) m/z 158 (^{35}Cl $M^+ + H^+$, 100), 160 (^{37}Cl $M^+ + H^+$, 55); HRMS calcd for $C_6H_9N_3{}^{35}Cl$ ($M^+ + H^+$) 158.0485; found 158.0489 (2.5 PPM); FTIR (neat, cm^{-1}) υ_{max} 3417, 1660, 149; mp: 44-45°C

4-chloro-*N*-ethylpyrimidin-2-amine (4-8)

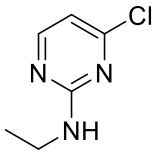

Yield 17% (89mg)

^{1}H NMR (400 MHz, $CDCl_3$) δ 8.01 (s, 1H), 6.67 (s, 1H), 3.55 (br, 2H), 2.67 (br, 1H), 1.38 – 1.14 (m, 3H).

***N*-(4-((4-(ethylamino)-6-methylpyrimidin-2-yl)amino)phenyl)benzamide (5-1)**

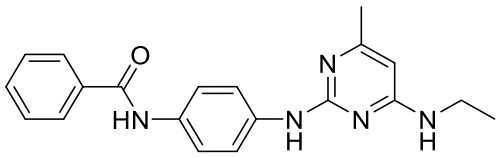

2-3 (300 mg, 1.41 mmol) and **4-2a** (243 mg, 1.41 mmol) were coupled according to the GP4. The product was obtained as grey solid (204 mg, 42%). ^{1}H NMR (400 MHz, DMSO-d_6) δ 10.38 (s, 1H), 10.15 (s, 1H), 8.91 (s, 1H), 8.11 (s, 1H), 7.93 (d, J = 7.7 Hz, 1H), 7.76 (d, J = 8.0 Hz, 3H), 7.53 (d, J = 8.0 Hz, 2H), 7.47 (t, J = 7.9 Hz, 1H), 5.97 (s, 1H), 2.22 (s, 3H), 1.13 (t, J = 7.3 Hz, 3H); ^{13}C NMR (100 MHz, DMSO-d_6) δ 165.9, 162.2, 152.5, 140.7, 135.7, 135.4, 133.9, 132.1, 128.9, 128.2, 121.5, 121.4, 106.8, 71.78, 40.7, 40.5, 40.3, 40.1, 39.8, 39.6, 39.4, 36.6, 34.2, 14.5, 13.5; MS (ESI+) m/z 348 (M^+ + H^+); HRMS calcd for $C_{20}H_{22}N_5O$ (M^++ H^+) 348.1824; found 348.1841 (4.9 PPM); FTIR (nujol, cm^{-1}) υ_{max} 1658, 1579, 1255, 835, 476; mp: 225-226°C

***N*-(4-((4-(ethylamino)-5-methylpyrimidin-2-yl)amino)phenyl)benzamide**

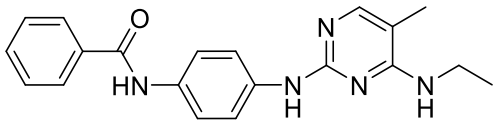

2-3 (74 mg, 350 µmol) and **4-1** (60 mg, 350 µmol) were coupled according to the GP4. The product was obtained as a colourless solid (78 mg, 64%). ^{1}H NMR (400 MHz, DMSO-d_6) δ 10.31 (s, 1H), 10.23 (s, 1H), 8.33 (s, 1H), 7.97 (d, *J* = 6.9 Hz, 2H), 7.81 (d, *J* = 5.6 Hz, 2H), 7.68 (s, 1H), 7.63 – 7.56 (m, 1H), 7.54 (d, *J* = 7.7 Hz, 4H), 3.58 – 3.36 (q, *J* = 7.0 Hz, 2H), 1.98 (s, 3H), 1.20 (t, *J* = 7.0 Hz, 3H); ^{13}C NMR (100 MHz, DMSO-d_6) δ 165.9, 162.9, 152.8, 151.9, 136.2, 135.4, 133.2, 132.1, 128.9, 128.2, 121.8, 121.4, 97.3, 36.3, 18.8, 14.4; MS (ESI+) m/z 348 (M^+ + H^+); HRMS calcd for $C_{20}H_{22}N_5O$ (M^++ H^+) 348.1824; found 348.1822 (-0.6 PPM);

***N*-(4-((4-(ethylamino)-6-methylpyrimidin-2-yl)amino)phenyl)-3-fluorobenzamide**

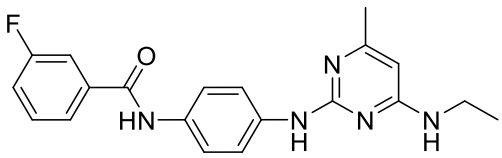

2-4 (300 mg, 1.30 mmol) and **4-2a** (223 mg, 1.30 mmol) were coupled according to the GP4. The product was obtained as a colourless solid (272 mg, 68%). ^{1}H NMR (400 MHz, DMSO-d_6) δ 10.41 (s, 1H), 10.28 (s, 1H), 9.02 (s, 1H), 7.88 – 7.75 (m, 4H), 7.68 – 7.49 (m, 3H), 7.45 (t, *J* = 7.3 Hz, 1H), 6.03 (s, 1H), 3.50 – 3.39 (m, 2H), 2.27 (s, 3H), 1.18 (t, *J* = 7.2 Hz, 3H); ^{13}C NMR (100 MHz, DMSO-d_6) δ 164.5 (d, J = 2.0 Hz), 162.5 (d, J = 244.3 Hz), , 152.8, 151.9, 137.7 (d, J = 6.7 Hz), 133.4, 131.1 (d, J = 8.0 Hz), 124.4, 121.7, 121.5, 119.0 (d, J = 20.7 Hz), 115.0 (d, J = 22.8 Hz). , 97.2, 36.2, 18.8, 14.3; MS (ESI+) m/z 366 ($M^+ + H^+$); HRMS calcd for $C_{20}H_{21}FN_5O$ ($M^+ + H^+$) 366.1730; found 366.1734 (3.6 PPM); FTIR (nujol, cm^{-1}) υ_{max} 1660, 1631, 1236, 1199, 839; mp: 259-263°C

***N*-(4-((4-(ethylamino)-5-methylpyrimidin-2-yl)amino)phenyl)-3-fluorobenzamide**

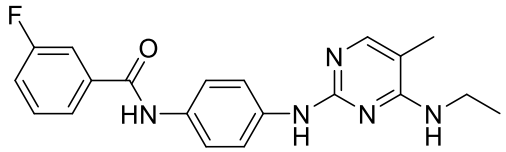

2-4 (70 mg, 304 µmol) and **4-1** (52 mg, 304 µmol) were coupled according to the GP4. The product was obtained as a colourless solid (45 mg, 41%). ^{1}H NMR (400 MHz, DMSO-d_6) δ 10.27 (s, 1H), 9.94 (s, 1H), 7.96 – 7.47 (m, 5H), 7.37 (d, J = 8.7 Hz, 2H), 6.57 (d, J = 8.8 Hz, 2H), 6.22 (s, 1H), 5.40 (s, 1H), 2.16 (s, 3H), 1.09 (t, J = 7.2 Hz, 3H); ^{13}C NMR (100 MHz, DMSO-d_6) δ 164.47, 163.0, 162.5 (d, J = 244.4 Hz), 153.0, 137.7, 135.7, 133.6, 131.1 (d, J = 8.3 Hz 124.4, 122.2, 121.6, 121.5, 118.9 (d, J = 20.7 Hz), 115.0 (d, J = 22.9 Hz), 97.2, ,36.3, 19.0, 14.4; MS (ESI+) m/z 366 ($M^+ + H^+$); HRMS calcd for $C_{20}H_{21}FN_5O$ ($M^+ + H^+$) 366.1730; found 366.1754 (6.6 PPM); FTIR (nujol, cm^{-1}) υ_{max} 13543, 1660, 1595, 1265; mp: > 230°C

3-bromo-*N*-(4-((4-(ethylamino)-5-methylpyrimidin-2-yl)amino)phenyl)benzamide

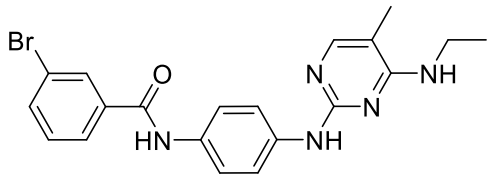

2-2 (85 mg, 291 µmol) and **4-1** (50 mg, 291 µmol) were coupled according to the GP4. The product was obtained as a grey solid (82 mg, 66%). ^{1}H NMR (400

MHz, DMSO-d_6) δ 10.41 (s, 1H), 10.25 (s, 1H), 8.40 (s, 1H), 8.16 (t, *J* = 1.7 Hz, 1H), 7.98 (d, *J* = 7.9 Hz, 1H), 7.81 (d, *J* = 8.9 Hz, 1H), 7.69 (s, 1H), 7.60 – 7.47 (m, 3H), 3.55 – 3.44 (m, 1H), 1.99 (s, 3H), 1.20 (t, *J* = 7.1 Hz, 3H); ^{13}C NMR (100 MHz, DMSO-d_6) δ 164.3, 162.3, 151.6, 137.5, 135.9, 134.8, 133.4, 131.2, 130.8, 127.4, 122.2, 121.5, 107.2, 89.0, 36.7, 14.4, 13.4; MS (ESI+) m/z 426 (^{79}Br M^+ + H^+, 100), 428 (^{81}Br M^++ H^+, 94); HRMS calcd for $C_{20}H_{21}{}^{79}BrN_5O$ (M^++ H^+) 426.0929 found 426.0922 (-1.6 PPM); FTIR (nujol, cm^{-1}) υ_{max} 1666, 1205, 829, mp: >230°C

3-bromo-*N*-(4-((2-(ethylamino)-6-methylpyrimidin-4-yl)amino)phenyl)benzamide (5-6)

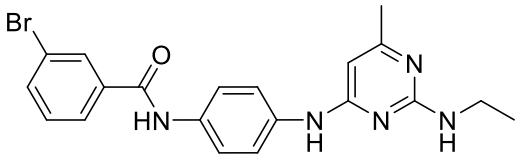

2-2 (300 mg, 1.03 mmol) and **4-2b** (177 mg, 1.03 mmol) were coupled according to the GP4. The product was obtained as a colourless solid (352 mg, 80%). ^{1}H NMR (400 MHz, DMSO-d_6) δ 10.81 (s, 1H), 10.45 (s, 1H), 8.15 (s, 1H), 7.97 (d, J = 7.9 Hz, 1H), 7.93 – 7.59 (m, 6H), 7.50 (t, J = 7.9 Hz, 1H), 6.17 (s, 1H), 2.28 (s, 3H), 1.17 (t, J = 7.1 Hz, 3H). ^{13}C NMR (100 MHz, DMSO-d_6) δ 164.4, 154.7, 137.5, 134.8, 131.2, 130.8, 127.4, 122.2, 122.0, 121.9, 121.3, 36.36, 18.98, 14.73; MS (ESI+) m/z 426 (^{79}Br M^+ + H^+, 100), 428 (^{81}Br M^++ H^+, 88); HRMS calcd for $C_{20}H_{11}{}^{79}BrN5O$ (M^++ H^+) 426.0817; found 426.0838 (4.9 PPM); FTIR (nujol, cm^{-1}) υ_{max} 3240, 1666, 842, 524; mp: 260-264°C

ethyl (2-((4-(3-bromobenzamido)phenyl)amino)-6-methylpyrimidin-4-yl)glycinate (5-7)

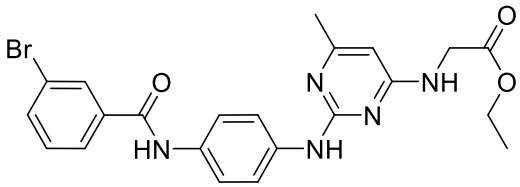

2-2 (507 mg, 1.74 mmol) and **4-5a** (400 mg, 1.74 mmol) were coupled according to the GP4. The product was obtained as a light grey solid (585 mg, 69%). ^{1}H NMR (400 MHz, DMSO-d_6) δ 10.42 (s, 1H), 10.02 (s, 1H), 9.25 (s, 1H), 8.15 (s, 1H), 7.97 (d, *J* = 7.8 Hz, 1H), 7.86 – 7.76 (m, *J* = 7.7, 4.3, 2.8 Hz, 3H), 7.52 (t,

J = 7.9 Hz, 1H), 7.48 (d, *J* = 8.9 Hz, 2H), 6.20 (s, 1H), 4.18 (s, *J* = 5.9 Hz, 2H), 4.11 (d, *J* = 7.1 Hz, 2H), 2.32 (s, 3H), 1.19 (t, *J* = 7.1 Hz, 2H); ^{13}C NMR (100 MHz, DMSO-d_6) δ 169.5, 164.3, 163.7, 137.5, 134.8, 131.2, 130.7, 127.3, 122.2, 121.9, 121.1, 97.3, 61.3, 43.0, 39.8, 39.6, 39.4, 19.1, 14.5; MS (ESI+) m/z 484 (^{79}Br M^+ + H^+, 100), 486 (^{81}Br M^++ H^+, 94); HRMS calcd for $C_{22}H_{23}{}^{81}BrN_5O_3$ (M^++ H^+) 486.0964; found 486.0970 (1.2 PPM); FTIR (nujol, cm^{-1}) υ_{max} 3331, 1726, 1668, 642; mp: > 230°C

3-bromo-*N*-(4-((4-(diethylamino)-6-methylpyrimidin-2-yl)amino)phenyl)benzamide (5-8)

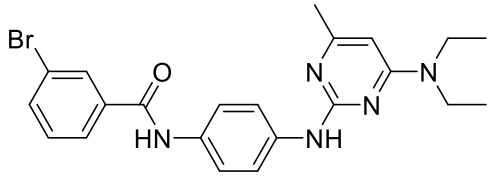

2-2 (644 mg, 2.21 mmol) was coupled with **4-4a** (442 mg, 2.21 mmol) according to the GP4. The product was obtained as a black solid (965 mg, 97%); ^{1}H NMR (396 MHz, DMSO-d_6) δ 9.97 (s, 1H), 8.10 (s, 1H), 7.92 (d, *J* = 7.8 Hz, 1H), 7.75 (d, *J* = 8.0 Hz, 1H), 7.47 (t, *J* = 7.9 Hz, 1H), 7.37 (d, *J* = 8.7 Hz, 2H), 6.59 – 6.51 (m, 3H), 5.01 (s, 2H), 3.60 – 3.47 (m, *J* = 14.2, 7.3 Hz, 4H), 2.26 (s, 3H), 1.10 (t, *J* = 7.0 Hz, 6H); ^{13}C NMR (100 MHz, DMSO-d_6) δ 170.0, 163.5, 160.8, 160.4, 145.9, 138.0, 134.3, 131.0, 130.5, 128.3, 127.1, 122.7, 122.1, 114.1, 107.6, 100.0, 41.8, 24.2, 13.3; FTIR (nujol, cm^{-1}) υ_{max} 3304, 1645, 1118, 889, 590; MS (ESI+) m/z 454 (^{79}Br M^+ + H^+, 100), 456 (^{81}Br M^++ H^+, 88); HRMS calcd for $C_{22}H_{25}{}^{81}BrN_5O$ (M^++ H^+) 456.1222; found 456.1245 (5.0 PPM); mp: 97-98°C

3-bromo-N-(4-((4-methyl-6-(methylamino)pyrimidin-2-yl)amino)phenyl)benzamide (5-9)

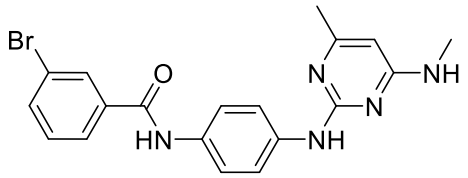

2-2 (388 mg, 1.33 mmol) and **4-7a** (210 mg, 1.33 mmol) were coupled according to the GP4. The product was obtained as a light blue solid (472 mg, 86%). ^{1}H NMR (400 MHz, DMSO-d_6) δ 10.42 (s, 1H), 10.28 (s, 1H), 8.96 (s, 1H), 8.15 (d, *J* = 1.5 Hz, 1H), 7.97 (d, *J* = 7.8 Hz, 1H), 7.80 (d, *J* = 7.9 Hz, 3H), 7.59 (d, *J* = 8.9 Hz, 2H), 7.50 (t, *J* = 7.9 Hz, 1H), 6.04 (s, 1H), 2.26 (s, *J* = 25.6 Hz, 3H).

^{13}C NMR (100 MHz, DMSO-d_6) δ 164.3, 163.6, 152.9, 137.5, 135.7, 134.8, 133.4, 131.1, 130.7, 127.3, 122.2, 121.7, 121.5, 97.2, 28.1, 18.8; MS (ESI+) m/z 412 (^{79}Br M^+ + H^+, 100), 414 (^{81}Br M^++ H^+, 74); HRMS calcd for $C_{19}H_{19}{}^{79}BrN_5O$ (M^++ H^+) 412.0773; found 412.0786 (3.2 PPM); FTIR (nujol, cm^{-1}) υ_{max} 3442, 1658, 1118, 835; mp: 302-3025°C

3-bromo-*N*-(4-((4-(isopropylamino)-6-methylpyrimidin-2-yl)amino)phenyl)benzamide (5-10)

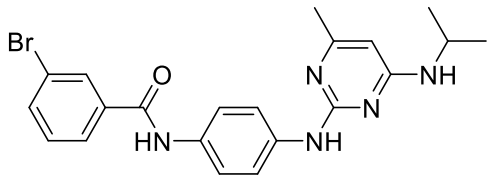

2-2 (300 mg, 1.03 mmol) and **4-3a** (191 mg, 1.03 mmol) were coupled according to the GP4. The product was obtained as black crystals (240 mg, 53%). ^{1}H NMR (400 MHz, DMSO-d_6) δ 10.40 (s, 1H), 10.04 (s, 1H), 8.75 (s, 1H), 8.15 (s, 1H), 7.97 (d, J = 7.7 Hz, 1H), 7.86 – 7.61 (m, J = 7.1, 4.9 Hz, 4H), 7.68 – 7.35 (m, J = 14.4, 8.2 Hz, 4H), 5.98 (s, 1H), 4.14 (s, 1H), 2.26 (s, 3H), 1.20 (d, J = 6.5 Hz, 6H)[7]; MS (ESI+) m/z 440 (^{79}Br M^+ + H^+, 100), 442 (^{81}Br M^++ H^+, 95); HRMS calcd for $C_{21}H_{23}{}^{79}BrN_5O$ (M^++ H^+) 440.1086; found 440.1103 (3.9 PPM); FTIR (nujol, cm^{-1}) υ_{max} 2320, 1666, 1573, 1155, 837, 480; mp: 183-185°C

3-bromo-*N*-(4-((4-((2-hydroxyethyl)amino)-6-methylpyrimidin-2-yl)amino)phenyl)benzamide (5-11)

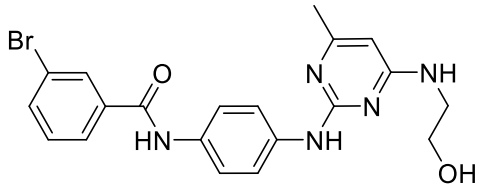

2-2 (310 mg, 1.07 mmol) and **4-6a** (200 mg, 1.07 mmol) were coupled according to the GP4. The product was obtained as a light blue solid (86 mg, 18%). ^{1}H NMR (400 MHz, DMSO-d_6) δ 10.43 (s, 1H), 10.25 (s, 1H), 9.00 (s, 1H), 8.16 (s, 1H), 7.98 (d, J = 8.0 Hz, 1H), 7.80 (d, J = 8.7 Hz, 3H), 7.57 (d, J = 8.3 Hz, 2H), 7.50 (t, J = 7.9 Hz, 1H), 6.07 (s, 1H), 4.93 (s, 1H), 3.58 (m, 2H), 3.48 (m, 2H), 2.26 (s, 3H); ^{13}C NMR (100 MHz, DMSO-d_6) δ 164.3, 163.4, 153.1, 152.3, 137.5, 135.6, 134.8, 133.6, 131.2, 130.8, 127.4, 122.6, 122.2, 121.5, 97.4, 59.5, 44.2,

[7] ^{13}C NMR data were not obtained due to the poor solubility

19.1; MS (ESI+) m/z (^{79}Br M^+ + H^+, 100), (^{81}Br M^++ H^+, 95); HRMS calcd for $C_{20}H_{21}BrN_5O_2$ (M^++ H^+) 442.0879; found 442.0864 (-3.4 PPM); > 230°C

3-bromo-*N*-(4-((4-(ethylamino)pyrimidin-2-yl)amino)phenyl)benzamide (5-12)

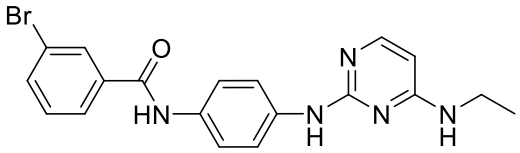

2-2 (300 mg, 1.03 mmol) and **4-8a** (162 mg, 1.03 mmol) were coupled according to the GP4. The product was obtained as a light brown solid (306 mg, 72%). ^{1}H NMR (400 MHz, DMSO-d_6) δ 12.07 (s, 1H), 10.74 (s, 1H), 10.48 (s, 1H), 9.25 (s, 1H), 8.17 (s, 1H), 7.99 (d, *J* = 7.7 Hz, 1H), 7.90 – 7.69 (m, *J* = 13.2, 8.9 Hz, 4H), 7.68 – 7.39 (m, *J* = 15.7, 11.6 Hz, 3H), 6.23 (d, *J* = 7.2 Hz, 1H), 3.46 – 3.39 (m, *J* = 6.9 Hz, 2H), 1.18 (t, *J* = 7.2 Hz, 3H); ^{13}C NMR (100 MHz, DMSO-d_6) δ 164.35, 152.43, 141.68, 137.50, 134.83, 131.20, 130.77, 127.40, 122.22, 121.49, 99.06, 74.55, 40.68, 36.22, 14.25; MS (ESI+) m/z 412 (^{79}Br M^+ + H^+, 100), 414 (^{81}Br M^++ H^+, 95); HRMS calcd for $C_{19}H_{20}{}^{79}BrN_5O$ (M^++ H^+) 412.0773; found 412.0775 (0.5 PPM); FTIR (nujol, cm^{-1}) υ_{max} 3417, 1670, 831; mp: 229-231°C.

***N*-(4-((4-(ethylamino)-6-methylpyrimidin-2-yl)amino)phenyl)-3-hydroxybenzamide (5-14)**

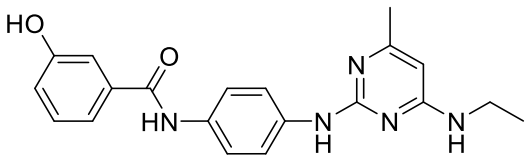

2-1 (250 mg, 1.10 mmol) and **4-2a** (187 mg, 1.10 mmol) were coupled according to the GP4. The product was obtained as a colourless solid (272 mg, 68%). ^{1}H NMR (396 MHz, DMSO-d_6) δ 10.22 (s, 2H), 9.79 (s, 1H), 8.99 (s, 1H), 7.80 (d, *J* = 8.8 Hz, 2H), 7.53 (d, *J* = 8.8 Hz, 2H), 7.38 (d, *J* = 7.8 Hz, 1H), 7.35 – 7.26 (m, *J* = 10.2, 5.5 Hz, 2H), 6.98 (d, *J* = 6.2 Hz, 1H), 6.01 (s, 1H), 2.26 (s, 3H), 1.17 (t, *J* = 7.3 Hz, 3H); ^{13}C NMR (100 MHz, DMSO-d_6) δ 165.9, 162.8, 157.9, 152.8, 151.9, 136.8, 136.2, 133.0, 129.9, 121.7, 121.3, 119.0, 118.6, 115.0, 97.2, 45.9, 36.2, 18.8, 14.3, 8.9; MS (ESI+) m/z 364 (M^+ + H^+); HRMS calcd for $C_{20}H_{23}N_5O_2$ (M^++ H^+) 364.1174; found 364.1768 (-1.6 PPM); FTIR (nujol, cm^{-1}) υ_{max} 1666, 1531, 1323, 835,478; mp: 283-285°C

***N*-(4-((4-(ethylamino)-6-methylpyrimidin-2-yl)amino)phenyl)-4-methylbenzamide (5-14)**

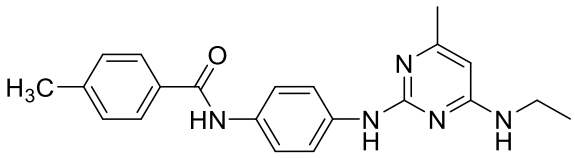

2-5 (250 mg, 1.10 mmol) and **4-2a** (187 mg, 1.10 mmol) were coupled according to the GP4. The product was obtained as a colourless solid (272 mg, 68%). ^{1}H NMR (396 MHz, DMSO-d_6) δ 10.27 (s, J = 14.1 Hz, 1H), 10.23 (s, 1H), 9.02 (s, 1H), 7.89 (d, J = 7.8 Hz, 2H), 7.81 (d, J = 8.6 Hz, 2H), 7.54 (d, J = 8.6 Hz, 2H), 7.33 (d, J = 7.9 Hz, 2H), 6.02 (s, 1H), 3.48 – 3.38 (m, 2H), 2.39 (s, 3H), 2.26 (s, 3H), 1.17 (t, J = 7.1 Hz, 3H); ^{13}C NMR (100 MHz, DMSO-d_6) δ 165.7, 162.8, 152.8, 142.0, 136.2, 133.0, 132.4, 129.4, 128.2, 121.7, 121.3, 97.2, 40.69, 36.24, 21.54, 18.84, 14.38; MS (ESI+) m/z 362 ($M^+ + H^+$); HRMS calcd for $C_{21}H_{24}N_5O$ ($M^+ + H^+$); 362.1981; found 362.1971 (-2.8 PPM); FTIR (nujol, cm^{-1}) υ_{max} 3446, 1662, 1573, 840, 744; mp: 298°C

***N*-(4-((4-(ethylamino)-6-methylpyrimidin-2-yl)amino)phenyl)-4-methoxybenzamide (5-15)**

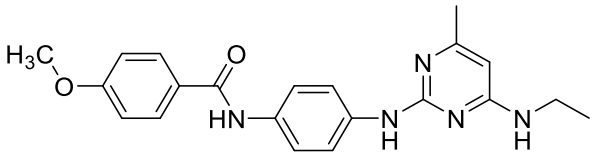

2-6 (250 mg, 1.10 mmol) and **4-2a** (187 mg, 1.10 mmol) were coupled according to the GP4. The product was obtained as a colourless solid (472 mg, 86%). ^{1}H NMR (400 MHz, DMSO-d_6) δ 10.27 (s, 1H), 10.17 (s, 1H), 9.01 (s, 1H), 8.08 – 7.91 (m, 2H), 7.80 (d, J = 8.4 Hz, 2H), 7.54 (d, J = 8.3 Hz, 2H), 7.06 (d, J = 7.7 Hz, 2H), 6.02 (s, 1H), 3.84 (s, 3H), 2.26 (s, J = 12.9 Hz, 3H), 1.17 (t, J = 7.6 Hz, 3H); 13C NMR (100 MHz, DMSO-d_6) δ 165.27, 162.89, 162.42, 152.91, 151.96, 136.35, 132.98, 130.11, 127.38, 121.71, 121.36, 114.13, 100.41, 97.21, 45.91, 36.23, 23.77, 14.39, 8.98; MS (ESI+) m/z 378 ($M^+ + H^+$); HRMS calcd for $C_{21}H_{24}N_5O_2$ ($M^+ + H^+$) 378.1930; found 378.1941 (2.9 PPM); FTIR (nujol, cm^{-1}) υ_{max} 3429, 1633, 1024, 835; mp: 285-288°C

3-bromo-*N*-(4-((4-(ethylamino)-6-methylpyrimidin-2-yl)amino)phenyl)benzamide (cpd 6)

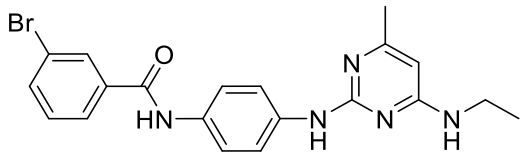

2-2 (300 mg, 1.03 mmol) and **4-2a** (176 mg, 1.03 mmol) were coupled according to the GP4. The product was obtained as a light grey solid (439 mg, 80%). ^{1}H NMR (400 MHz, DMSO-d_6) δ 10.37 (s, 1H), 10.28 (s, 1H), 8.87 (s, 1H), 8.14 (d, *J* = 1.5 Hz, 1H), 7.95 (d, *J* = 7.8 Hz, 1H), 7.83 – 7.70 (m, *J* = 15.5, 9.0 Hz, 3H), 7.55 (d, *J* = 8.9 Hz, 2H), 7.46 (t, *J* = 7.9 Hz, 1H), 5.98 (s, 1H), 3.46 – 3.30 (m, 2H), 2.23 (s, 3H), 1.15 (t, *J* = 7.2 Hz, 3H); ^{13}C NMR (100 MHz, DMSO-d_6) δ 164.3, 162.8, 152.8, 151.7, 137.5, 135.8, 134.8, 133.4, 131.1, 130.7, 127.3, 122.2, 121.6, 121.4, 97.5, 36.2, 18.8, 14.3; MS (ESI+) m/z 426 (^{79}Br M^+ + H^+, 100), 428 (^{81}Br M^++ H^+, 85); HRMS calcd for $C_{20}H_{21}{}^{81}BrN_5O$ (M^++ H^+) 412.0909; found 412.0898 (-2.6 PPM); FTIR (nujol, cm^{-1}) υ_{max} 1658, 1116, 869, 599; mp: 227-230°C

Cpd 6 commercially obtained reference spectrum

^{1}H NMR (400 MHz, DMSO-d_6) δ 10.36 (s, 1H), 9.85 (s, 1H), 8.34 (s, 1H), 8.16 (s, 1H), 7.98 (d, *J* = 7.8 Hz, 1H), 7.79 (d, *J* = 8.4 Hz, 1H), 7.74 (d, *J* = 8.8 Hz, 2H), 7.65 (d, *J* = 8.8 Hz, 2H), 7.50 (t, *J* = 7.9 Hz, 1H), 5.96 (s, 1H), 2.22 (s, 3H), 1.17 (t, *J* = 7.2 Hz, 3H).

7.2 Modelling studies

Table 7-1: The best scoring 104 compounds. 81 were commercially available and were purchased. The consensus score is the primary scoring function with Glide XP gscore being the secondary function. Consensus score counts in how many other functions ligand scored in top 20 %.

ZINC ID	Consensus	r_glide_XP_G Score	r_i_dock_score	LigSc2 Dreiding	PLP1	PLP2	Jain	PMF	PMF04	Ludi_1	Ludi_2	Ludi_3	LigScore1_Dre iding
ZINC00909887	9	-8,26	-5,547	5,45	104,48	89,5	3,13	123,82	68,3	630	504	566	3,59
ZINC13058698	9	-6,603	-4,315	5,32	67,68	68,19	4,28	10,99	5,21	479	410	383	5,34
ZINC21805942	9	-5,932	-3,901	5,81	88,15	90,01	5,93	131,67	62,76	685	541	519	4,7
ZINC03670611	9	-5,662	-5,661	5,42	101,81	96,74	6,22	130,16	62,2	698	603	606	4,91
ZINC03670621	9	-5,649	-5,648	4,67	86,89	84,16	5,07	126,65	65,73	518	447	445	3,92
ZINC03619936	9	-5,584	-5,584	5,46	97,25	92,15	7,4	140,71	64,26	747	618	613	5,01
ZINC21805789	9	-5,58	-3,549	5,15	84,37	87,12	7,5	114,34	45,98	720	616	599	4,76
ZINC21805751	9	-5,569	-5,467	6,01	92,82	88,26	2,73	138,17	61,71	751	585	626	5,02
ZINC14671532	9	-5,568	-4,865	5,58	100,99	103,05	7,1	99,44	28,54	853	687	686	5,11
ZINC21805822	9	-5,489	-3,458	5,25	93,78	90,17	2,9	130,34	55,09	497	444	447	4,58
ZINC02707532	8	-6,633	-6,609	5,66	97,24	101,86	5,76	101,33	52,69	582	538	590	5,36
ZINC20112435	8	-5,536	-5,059	5,36	87,28	81,55	3,35	120,26	64,6	436	376	381	4,18
ZINC13058696	8	-5,454	-4,97	4,95	82,63	83,61	4,49	105,18	64,54	718	603	606	5,21
ZINC01182053	8	-5,428	-5,428	6,53	113,71	105,16	4,23	107,82	39,77	572	488	548	5,9
ZINC01122902	7	-8,598	-7,266	5,12	109,7	110,44	5,74	98,5	27,05	684	579	574	4,53
ZINC06812753	7	-7,925	-6,892	5,16	104,1	92,5	5,73	52,09	11,92	845	650	661	5,7
ZINC09573292	7	-5,706	-4,815	5,35	99,55	90,78	4,28	91,52	38	664	558	606	4,15
ZINC15016433	7	-5,461	-5,375	5,69	88,45	81,36	4,49	97,01	39,99	640	531	589	4,44
ZINC04189423	6	-6,77	-5,016	4,05	98,81	99,47	5,5	95,94	31,79	605	501	584	3,63
ZINC00689376	6	-6,258	-5,675	4,53	82,35	86,03	4,94	99,39	35,88	616	503	511	3,38
ZINC20032808	6	-6,001	-6,001	5,04	95,62	91,71	4,81	112,43	38,83	585	525	634	3,63
ZINC00909904	6	-5,874	-5,874	5,15	102,59	86,58	2,71	125,49	59,74	480	399	463	2,82
ZINC04123403	6	-5,633	-5,211	6,2	98,75	92,84	3,64	68,36	17,53	691	534	547	5,59
ZINC01217310	6	-5,618	-5,618	4,72	95,31	88,54	4,31	95,46	23,98	616	548	549	3,15
ZINC23993846	6	-5,491	-4,599	5	102,29	98,38	4,76	72,51	27,9	748	571	564	4,2
ZINC04163777	5	-7,98	-7,072	5,14	67,05	62,94	1,13	87,84	55,92	461	436	502	4,49
ZINC00976030	5	-7,047	-4,334	5,42	77,47	70,59	4,58	56,11	18,2	717	562	518	5,31
ZINC13536834	5	-6,968	-6,874	5,92	85,03	71,97	2,8	61,62	16,98	620	479	480	5,77
ZINC18085882	5	-6,649	-6,484	5,88	93,17	79,71	3,44	61,17	17,76	628	529	516	5,62
ZINC03111970	5	-6,332	-5,893	4,82	77,4	77,38	4,9	60,68	23,27	639	502	520	5,29
ZINC04150548	5	-6,322	-6,32	5,07	77,19	84,82	5,36	104,19	59,38	559	495	603	4,93
ZINC18063836	5	-6,318	-5,919	4,69	94,18	89,86	3,19	97,86	36,27	469	438	494	3,41
ZINC04688053	5	-6,177	-5,93	5,47	72,56	72,8	2,61	82,26	49,18	429	381	411	5,69
ZINC04953322	5	-6,172	-3,459	5,47	78,22	71,6	4,43	58,06	22,39	665	534	484	5,27
ZINC00812876	5	-5,873	-4,542	5,66	95	96,81	4,58	90,98	28,97	573	481	480	4,82
ZINC33870265	5	-5,858	-3,613	5,02	93,05	78,3	3,03	46,59	4,73	460	393	413	4,45

ZINC ID	Consensus	r_glide_XP_G Score	r_i_dock_score	LigSc2 Dreiding	PLP1	PLP2	Jain	PMF	PMF04	Ludi_1	Ludi_2	Ludi_3	LigScore1_Dreiding
ZINC00641276	5	-5,754	-5,754	5	92,88	93	4,72	112,36	37,61	531	510	606	2,81
ZINC04763770	5	-5,661	-3,374	6,21	88,33	84,97	3,59	83,57	34,57	623	466	475	6,41
ZINC08915433	5	-5,653	-4,977	5,03	82,13	77,31	1,18	97,41	49,42	384	367	493	3,48
ZINC00779976	5	-5,621	-5,621	4,41	91,95	80,5	4,38	101,19	37,64	436	380	398	2,56
ZINC19681401	5	-5,614	-5,545	5,53	66,08	53,86	3,39	43,9	21,36	652	533	493	5,79
ZINC01425536	5	-5,59	-5,589	4,67	101,23	97,64	4,25	99,73	33,75	526	493	543	2,59
ZINC06753028	4	-7,632	-7,222	4,34	68,9	65,16	2,34	94,56	39,42	363	348	429	3,72
ZINC19880801	4	-7,396	-5,109	4,9	78,95	75,79	2,11	61,99	16,34	339	342	360	4,05
ZINC18119210	4	-7,182	-7,082	6,04	89,63	76,86	2,37	69,78	21,24	619	491	488	5,54
ZINC19323203	4	-7,156	-6,962	4,94	78,36	79,26	3,51	41,44	13,61	465	414	382	5,08
ZINC36602822	4	-6,82	-6,811	5,34	68,86	70,06	3,99	99,77	60,38	415	399	449	5,05
ZINC04092568	4	-6,602	-6,602	5,42	77,11	90,21	4,44	73,77	43,93	556	491	502	5,38
ZINC00909938	4	-6,507	-6,506	4,87	105,72	91,61	3,65	116,47	53,6	540	445	507	3,31
ZINC19323242	4	-6,336	-5,317	4,02	56,21	53,02	4,91	127,82	70,11	505	459	416	3,7
ZINC19323200	4	-6,233	-6,222	4,47	75,83	70,72	5,14	104,87	55,99	504	458	425	4,83
ZINC08384217	4	-6,172	-5,927	5,4	83,09	77,86	4,32	86,98	23,01	506	467	462	4,72
ZINC03897398	4	-6,006	-6,006	4,84	61,49	63,61	2,42	48,92	18,25	401	365	332	4,54
ZINC17014949	4	-5,899	-5,898	5,16	108,11	103,37	3,68	105,89	37,63	544	512	560	3,13
ZINC00815821	4	-5,859	-4,529	4,66	81	84,37	3,68	90,86	25,35	550	500	505	4,06
ZINC03902520	4	-5,806	-4,462	5,11	67,18	54,71	0,28	70,4	28,9	448	366	380	3,9
ZINC04387219	4	-5,719	-5,28	5,91	87,74	81,59	3,12	67,58	29,28	678	524	533	5,65
ZINC21873702	4	-5,688	-5,685	5,37	84,48	76,41	2,22	85,59	40,67	588	483	552	4,86
ZINC01218728	4	-5,429	-5,428	4,53	98,65	90,67	3,87	83,28	22,28	538	519	524	2,83
ZINC06812732	3	-7,112	-7,024	6,17	89,45	79,4	2,51	66,94	20,48	652	493	492	5,86
ZINC36046230	3	-6,564	-6,564	5,46	97,06	92,2	0,7	80,54	31,45	514	447	475	5,06
ZINC01831275	3	-6,366	-5,32	5,13	63,9	70,96	5,98	101,34	48,47	501	488	503	4,43
ZINC04688057	3	-6,178	-5,54	4,86	78,3	72,23	2,01	95,96	46,65	573	477	505	4,4
ZINC03628230	3	-6,021	-6,008	4,89	71,22	78,91	6,75	96,21	58,68	449	422	546	4,15
ZINC04262967	3	-5,944	-5,944	5,27	104,78	96,3	3,9	109,06	43,22	517	454	512	3,17
ZINC01167520	3	-5,851	-4,905	4,82	60,12	58,75	0,86	77,63	55,36	297	297	325	4,76
ZINC04073248	3	-5,83	-5,83	5,91	79,72	75,33	2,42	103,84	39,08	663	520	500	6,13
ZINC04092846	3	-5,824	-5,824	5	76,66	78	3,8	88,57	43,07	592	505	523	4,75
ZINC08915342	3	-5,757	-4,655	4,72	59,32	63,95	1,22	67,29	41,01	495	442	413	4,64
ZINC00815820	3	-5,744	-4,414	5,44	91,63	93,18	4,53	88,83	24,32	533	454	462	4,51
ZINC13551128	3	-5,664	-5,564	5,64	90,86	74,61	3,65	63,5	17,91	584	484	483	5,31
ZINC00909916	3	-5,635	-5,635	4,88	103,93	89,3	3,78	114,74	51	478	435	501	2,75
ZINC09356401	3	-5,616	-4,97	5,24	75,57	70,75	2,33	89,43	35,93	351	309	324	4,24
ZINC21353681	3	-5,558	-4,706	4,72	87,59	81,27	2,9	94,13	39,91	458	377	462	2,4
ZINC12631271	3	-5,534	-4,752	5,69	79,78	71,95	2,19	55,08	13,9	522	412	425	5,25
ZINC00909909	3	-5,518	-5,518	4,83	97,9	82,26	2,45	118,91	57,79	402	387	460	2,52
ZINC04064305	3	-5,428	-5,428	4,57	62,08	55,79	0,43	72,13	29,08	296	286	357	3,59
ZINC03897837	2	-6,807	-6,807	5,2	68,88	74,98	4,36	37,08	9,32	515	421	388	5,1

ZINC ID	Consensus	r_glide_XP_G Score	r_i_dock_score	LigSc2 Dreiding	PLP1	PLP2	Jain	PMF	PMF04	Ludi_1	Ludi_2	Ludi_3	LigScore1_Dreiding
ZINC19323209	2	-6,744	-6,55	5,09	82,54	81,09	3,44	44,46	14,17	502	469	440	5,4
ZINC18067217	2	-6,679	-5,253	5,93	89,52	84,42	3,64	85,6	41	517	434	498	5,46
ZINC00883200	2	-6,63	-5,281	4,52	55,28	60,7	5,2	53,31	13,37	568	476	479	4,33
ZINC19323149	2	-6,586	-4,243	4,25	64,06	60,39	1,62	44,85	8,19	365	367	340	4
ZINC18277048	2	-6,355	-6,139	5,06	78,01	77,87	3,55	104,7	45,81	481	422	480	3,68
ZINC09359051	2	-6,288	-6,287	5,09	101,71	93,82	3,16	102,94	40,84	438	400	462	3,4
ZINC19323246	2	-6,257	-5,238	4,27	60,47	59,45	0,53	68,39	30,11	286	292	261	4,17
ZINC16248102	2	-6,224	-5,794	4,2	51,79	51,99	0,83	56,64	33,17	298	287	327	3,04
ZINC01895963	2	-6,086	-5,112	5,53	82,45	84,41	2,17	88,05	34,3	344	320	350	5,08
ZINC00191785	2	-6,065	-6,038	5,16	70,67	77,15	3,85	105,54	64,39	471	450	561	4,2
ZINC01514638	1	-7,099	-7,099	5,25	76,63	69,64	2,22	45,31	18,79	439	368	343	4,87
ZINC08915313	1	-7,041	-6,117	5,07	65,73	67,34	0,89	81,31	41,72	441	386	448	3,88
ZINC00092051	1	-7,011	-7,011	5,13	67,44	75,58	2,55	46,19	25,19	517	442	409	4,63
ZINC08915344	1	-6,999	-6,119	4,95	63,43	63,51	0,73	83,37	40,22	336	320	391	3,76
ZINC19323322	1	-6,748	-4,813	5,32	68,44	71,8	2,73	40,2	9,1	372	339	322	5,24
ZINC04688055	1	-6,71	-6,463	5,54	68,35	71,09	2,98	89,77	49,96	540	453	412	5,8
ZINC03897836	1	-6,464	-6,464	5,4	73,42	74,68	1,06	48,76	17,57	341	306	328	5,07
ZINC04185655	1	-6,336	-6,336	5,55	77,64	83,38	2,77	49,48	19,56	520	448	472	5,56
ZINC03878474	1	-6,323	-6,323	5,41	74,4	76,73	1,2	48,84	18,87	350	322	346	5,1
ZINC21658070	1	-6,27	-6,27	5,07	67,76	70,81	2,93	75,65	40,93	469	415	604	3,85
ZINC03878475	1	-6,26	-6,26	5,21	72,87	73,15	3,16	40,4	15,8	411	387	354	5,16
ZINC04189446	1	-6,181	-4,427	4,96	88,68	88,88	3,09	105,18	37,26	482	397	406	4,06
ZINC04270578	1	-6,17	-6,17	5,1	71,12	70,05	3,07	33,47	2,7	425	354	331	4,62
ZINC01817289	1	-6,027	-5,054	2,75	44,09	48,13	1,4	70,87	28,31	204	264	283	2,07
ZINC03904856	1	-6,005	-5,223	4,36	77,59	81,63	4,67	93,44	37,79	535	459	517	3,29

7.3 Compounds curve fittings

7.3.1 Growth inhibition

5-1

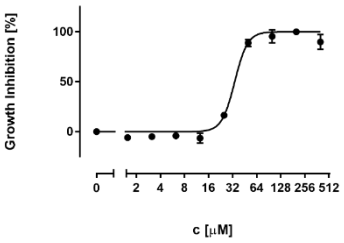

5-2

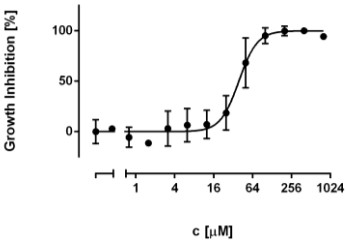

5-3

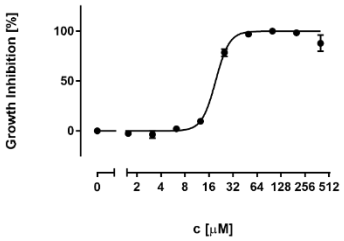

5-4

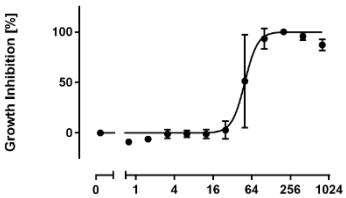

5-5

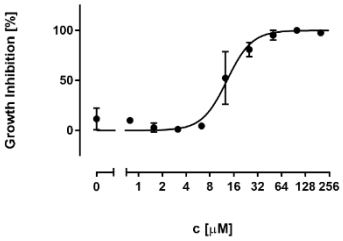

5-6

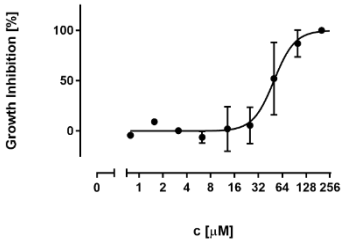

5-7

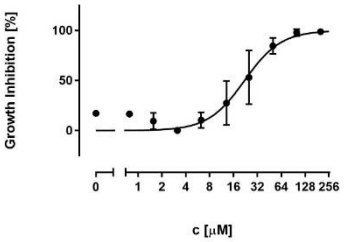

5-8

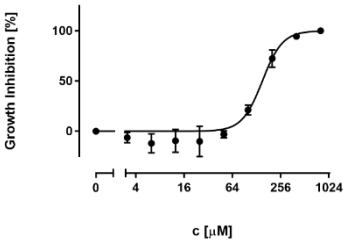

5-9

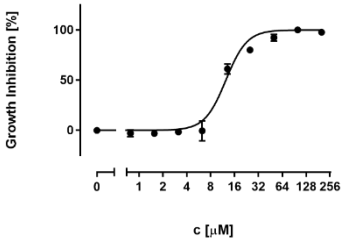

5-10

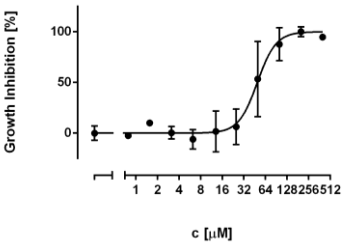

5-11

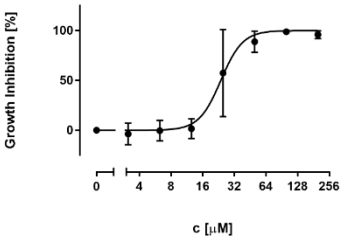

5-12

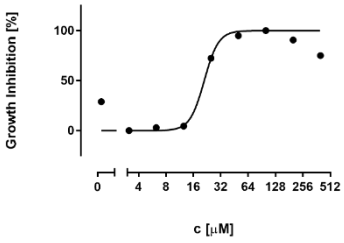

5-13

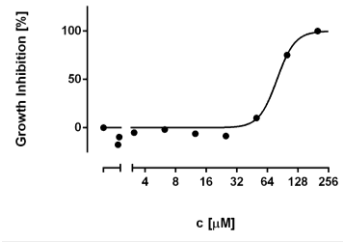

5-14

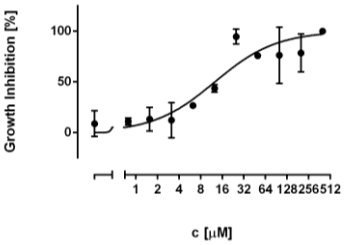

5-15

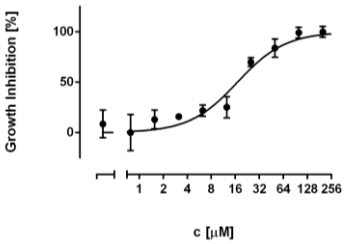

7.3.2 IMV ATP synthesis inhibition

5-1

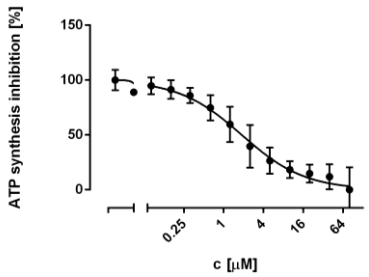

5-2

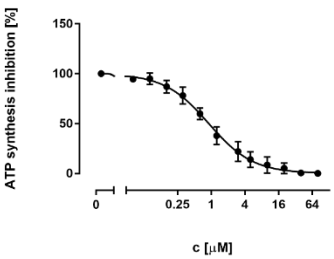

5-3

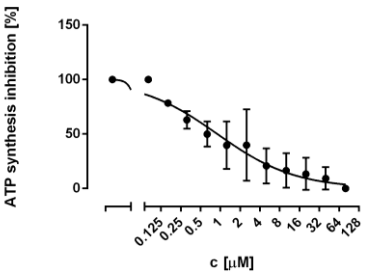

5-4

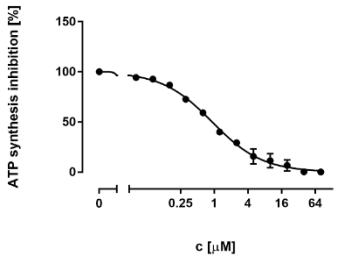

5-5

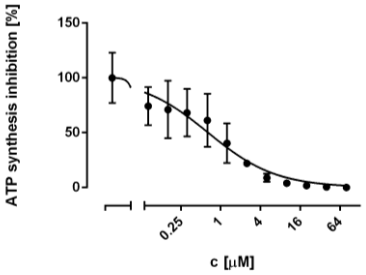

5-6

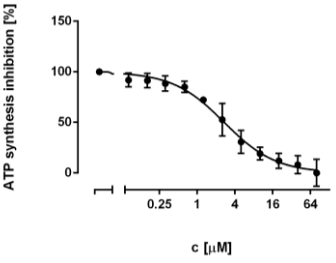

5-7

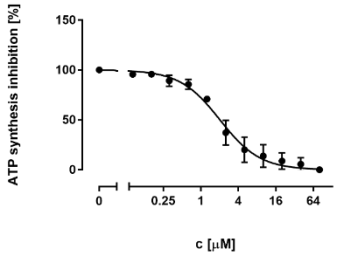

5-8

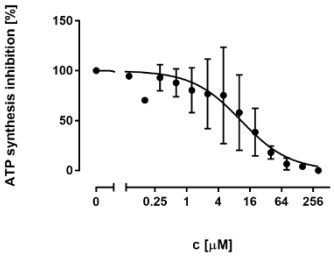

5-9

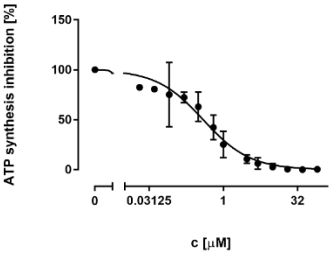

5-10

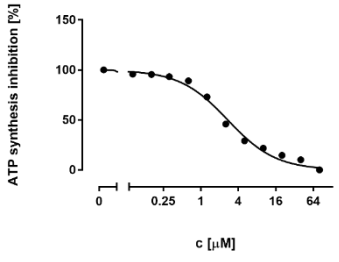

5-11

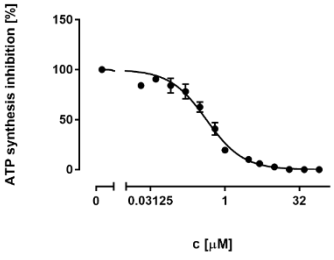

5-12

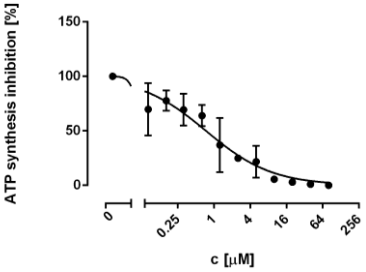

5-13

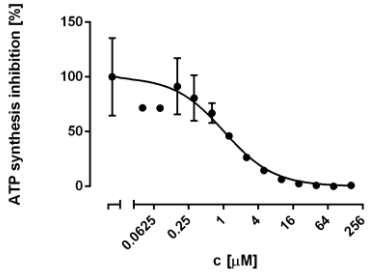

5-14

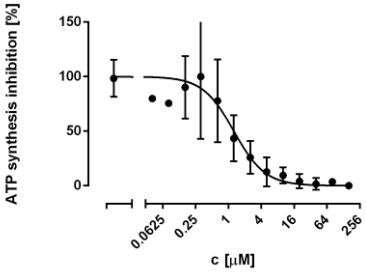

5-15

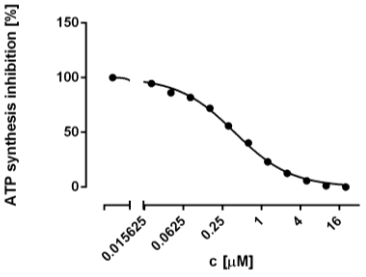

References

8. References

1. Geneva: World Health Organization, *Global tuberculosis report 2017*. 2017.

2. Nahid, P., M. Pai, and P.C. Hopewell, *Advances in the diagnosis and treatment of tuberculosis.* Proc Am Thorac Soc, 2006. **3**(1): p. 103-10.

3. Blumberg, H.M., M.K. Leonard, Jr., and R.M. Jasmer, *Update on the treatment of tuberculosis and latent tuberculosis infection.* JAMA, 2005. **293**(22): p. 2776-84.

4. Brosch, R., et al., *A new evolutionary scenario for the Mycobacterium tuberculosis complex.* Proc Natl Acad Sci U S A, 2002. **99**(6): p. 3684-9.

5. Talbot, E.A. and B.J. Raffa, *Mycobacterium tuberculosis*, in *Molecular Medical Microbiology*. 2015. p. 1637-1653.

6. Vergne, I., et al., *Cell biology of mycobacterium tuberculosis phagosome.* Annu Rev Cell Dev Biol, 2004. **20**: p. 367-94.

7. Armstrong, J.A., *Response of Cultured Macrophages to Mycobacterium Tuberculosis, with Observations on Fusion of Lysosomes with Phagosomes.* Journal of Experimental Medicine, 1971. **134**(3): p. 713-740.

8. Meena, L.S. and Rajni, *Survival mechanisms of pathogenic Mycobacterium tuberculosis H37Rv.* FEBS J, 2010. **277**(11): p. 2416-27.

9. Houben, D., et al., *ESX-1-mediated translocation to the cytosol controls virulence of mycobacteria.* Cell Microbiol, 2012. **14**(8): p. 1287-98.

10. van der Wel, N., et al., *M. tuberculosis and M. leprae translocate from the phagolysosome to the cytosol in myeloid cells.* Cell, 2007. **129**(7): p. 1287-98.

11. Roach, D.R., et al., *TNF Regulates Chemokine Induction Essential for Cell Recruitment, Granuloma Formation, and Clearance of Mycobacterial Infection.* The Journal of Immunology, 2002. **168**(9): p. 4620-4627.

12. Cooper, A.M., A. Solache, and S.A. Khader, *Interleukin-12 and tuberculosis: an old story revisited.* Curr Opin Immunol, 2007. **19**(4): p. 441-7.

13. Russell, D.G., et al., *Foamy macrophages and the progression of the human tuberculosis granuloma.* Nat Immunol, 2009. **10**(9): p. 943-8.

14. Smith, I., *Mycobacterium tuberculosis Pathogenesis and Molecular Determinants of Virulence.* Clinical Microbiology Reviews, 2003. **16**(3): p. 463-496.

15. Cardona, P.J., *A spotlight on liquefaction: evidence from clinical settings and experimental models in tuberculosis.* Clin Dev Immunol, 2011. **2011**: p. 868246.

16. Ehlers, S. and U.E. Schaible, *The granuloma in tuberculosis: dynamics of a host-pathogen collusion.* Front Immunol, 2012. **3**: p. 411.

17. Salgame, P., *MMPs in tuberculosis: granuloma creators and tissue destroyers.* J Clin Invest, 2011. **121**(5): p. 1686-8.

18. Barry, C.E., 3rd, et al., *The spectrum of latent tuberculosis: rethinking the biology and intervention strategies.* Nat Rev Microbiol, 2009. **7**(12): p. 845-55.

19. Flynn, J.L., J. Chan, and P.L. Lin, *Macrophages and control of granulomatous inflammation in tuberculosis.* Mucosal Immunol, 2011. **4**(3): p. 271-8.

20. Santucci, N., et al., *A clinical correlate of the dysregulated immunoendocrine response in human tuberculosis.* Neuroimmunomodulation, 2010. **17**(3): p. 184-7.

21. Lee, E. and R.S. Holzman, *Evolution and current use of the tuberculin test.* Clin Infect Dis, 2002. **34**(3): p. 365-70.

22. Long, E.R. and F.B. Seibert, *The chemical composition of the active principle of tuberculin. I. A non-protein medium suitable for the production of tuberculin in large quantity. Amer.* Am. Rev. Tuberc, 1926. **13**: p. 393-397.

23. Heaf, F., *The Multiple-Puncture Tuberculin Test.* The Lancet, 1951. **258**(6674): p. 151-153.

24. Kunst, H., *Diagnosis of latent tuberculosis infection: the potential role of new technologies.* Respir Med, 2006. **100**(12): p. 2098-106.

25. Pai, M., L.W. Riley, and J.M. Colford, *Interferon-γ assays in the immunodiagnosis of tuberculosis: a systematic review.* The Lancet Infectious Diseases, 2004. **4**(12): p. 761-776.

26. WHO Guidelines Approved by the Guidelines Review Committee, *Guidelines on the management of latent tuberculosis infection.* Geneva: World Health Organization, 2015.

27. Bamrah, S., et al., *Treatment for LTBI in contacts of MDR-TB patients, Federated States of Micronesia, 2009-2012.* Int J Tuberc Lung Dis, 2014. **18**(8): p. 912-8.

28. van Crevel, R., T.H.M. Ottenhoff, and J.W.M. van der Meer, *Innate Immunity to Mycobacterium tuberculosis.* Clinical Microbiology Reviews, 2002. **15**(2): p. 294-309.

29. Control, C.f.D. and Prevention, *Plan to combat extensively drug-resistant tuberculosis: recommendations of the Federal Tuberculosis Task Force.* MMWR. Recommendations and reports: Morbidity and mortality weekly report. Recommendations and reports/Centers for Disease Control, 2009. **58**(RR-3): p. 1.

30. Cohen, R., et al., *The Validity of Classic Symptoms and Chest Radiographic Configuration in Predicting Pulmonary Tuberculosis.* Chest, 1996. **109**(2): p. 420-423.

31. Steingart, K.R., A. Ramsay, and M. Pai, *Optimizing sputum smear microscopy for the diagnosis of pulmonary tuberculosis.* Expert Rev Anti Infect Ther, 2007. **5**(3): p. 327-31.

32. Steingart, K.R., et al., *Sputum processing methods to improve the sensitivity of smear microscopy for tuberculosis: a systematic review.* The Lancet Infectious Diseases, 2006. **6**(10): p. 664-674.

33. Urbanczik, R., *Present position of microscopy and of culture in diagnostic mycobacteriology.* Zentralblatt für Bakteriologie, Mikrobiologie und Hygiene. Series A: Medical Microbiology, Infectious Diseases, Virology, Parasitology, 1985. **260**(1): p. 81-87.

34. Steingart, K.R., et al., *Fluorescence versus conventional sputum smear microscopy for tuberculosis: a systematic review.* The Lancet Infectious Diseases, 2006. **6**(9): p. 570-581.

35. Cruciani, M., et al., *Meta-Analysis of BACTEC MGIT 960 and BACTEC 460 TB, with or without Solid Media, for Detection of Mycobacteria.* Journal of Clinical Microbiology, 2004. **42**(5): p. 2321-2325.

36. Helb, D., et al., *Rapid detection of Mycobacterium tuberculosis and rifampin resistance by use of on-demand, near-patient technology.* J Clin Microbiol, 2010. **48**(1): p. 229-37.

37. Small, P.M. and M. Pai, *Tuberculosis diagnosis--time for a game change.* N Engl J Med, 2010. **363**(11): p. 1070-1.

38. Golden, M.P. and H.R. Vikram, *Extrapulmonary tuberculosis: an overview.* American family physician, 2005. **72**(9).

39. Ramírez-Lapausa, M., A. Menéndez-Saldaña, and A. Noguerado-Asensio, *Extrapulmonary tuberculosis: an overview.* Rev Esp Sanid Penit, 2015. **17**: p. 3-11.

40. Shafer, R.W., et al., *Extrapulmonary tuberculosis in patients with human immunodeficiency virus infection.* Medicine, 1991. **70**(6): p. 384-397.

41. Sharma, S.K., A. Mohan, and A. Sharma, *Miliary tuberculosis: A new look at an old foe.* Journal of Clinical Tuberculosis and Other Mycobacterial Diseases, 2016. **3**: p. 13-27.

42. Sharma, S.K., et al., *Miliary tuberculosis: new insights into an old disease.* The Lancet Infectious Diseases, 2005. **5**(7): p. 415-430.

43. Peto, H.M., et al., *Epidemiology of extrapulmonary tuberculosis in the United States, 1993-2006.* Clin Infect Dis, 2009. **49**(9): p. 1350-7.

44. Prevots, D.R., et al., *Nontuberculous mycobacterial lung disease prevalence at four integrated health care delivery systems.* Am J Respir Crit Care Med, 2010. **182**(7): p. 970-6.

45. Phillips, M.S. and C.F. von Reyn, *Nosocomial infections due to nontuberculous mycobacteria.* Clin Infect Dis, 2001. **33**(8): p. 1363-74.

46. Peters, M., et al., *Isolation of atypical mycobacteria from tap water in hospitals and homes: Is this a possible source of disseminated MAC infection in AIDS patients?* Journal of Infection, 1995. **31**(1): p. 39-44.

47. Winthrop, K.L., et al., *Pulmonary nontuberculous mycobacterial disease prevalence and clinical features: an emerging public health disease.* Am J Respir Crit Care Med, 2010. **182**(7): p. 977-82.

48. Wallace, R.J., Jr., B.A. Brown, and D.E. Griffith, *Nosocomial outbreaks/pseudo-outbreaks caused by nontuberculous mycobacteria.* Annu Rev Microbiol, 1998. **52**: p. 453-90.

49. Kennedy, T.P. and D.J. Weber, *Nontuberculous mycobacteria. An underappreciated cause of geriatric lung disease.* Am J Respir Crit Care Med, 1994. **149**(6): p. 1654-8.

50. Lai, C.C., et al., *Increasing incidence of nontuberculous mycobacteria, Taiwan, 2000-2008.* Emerg Infect Dis, 2010. **16**(2): p. 294-6.

51. Bryant, J.M., et al., *Emergence and spread of a human-transmissible multidrug-resistant nontuberculous mycobacterium.* Science, 2016. **354**(6313): p. 751-757.

52. Thomson, R.M. and W.W. Yew, *When and how to treat pulmonary non-tuberculous mycobacterial diseases.* Respirology, 2009. **14**(1): p. 12-26.

53. Edginton, M., C. Sekatane, and S. Goldstein, *PatientsÕ beliefs: do they affect tuberculosis control? A study in a rural district of South Africa.* The International Journal of Tuberculosis and Lung Disease, 2002. **6**(12): p. 1075-1082.

54. Munro, S.A., et al., *Patient adherence to tuberculosis treatment: a systematic review of qualitative research.* PLoS Med, 2007. **4**(7): p. e238.

55. Liam, C., et al., *Attitudes and knowledge of newly diagnosed tuberculosis patients regarding the disease, and factors affecting treatment compliance.* The International Journal of Tuberculosis and Lung Disease, 1999. **3**(4): p. 300-309.

56. Greene, J.A., *An Ethnography of Nonadherence: Culture, Poverty, and Tuberculosis in Urban Bolivia.* Culture, Medicine and Psychiatry, 2004. **28**(3): p. 401-425.

57. Bayer, R., D. Wilkinson, and R. Bayer, *Directly observed therapy for tuberculosis: history of an idea.* The Lancet, 1995. **345**(8964): p. 1545-1548.

58. Noyes, J. and J. Popay, *Directly observed therapy and tuberculosis: how can a systematic review of qualitative research contribute to improving services? A qualitative meta-synthesis.* J Adv Nurs, 2007. **57**(3): p. 227-43.

59. Khan, M.A., et al., *Tuberculosis patient adherence to direct observation: results of a social study in Pakistan.* Health Policy Plan, 2005. **20**(6): p. 354-65.

60. Volmink, J. and P. Garner, *Directly observed therapy for treating tuberculosis.* Cochrane Database Syst Rev, 2007(4): p. CD003343.

61. Selwyn , P.A., et al., *A Prospective Study of the Risk of Tuberculosis among Intravenous Drug Users with Human Immunodeficiency Virus Infection.* New England Journal of Medicine, 1989. **320**(9): p. 545-550.

62. Nathan, C., *Taming tuberculosis: a challenge for science and society.* Cell Host Microbe, 2009. **5**(3): p. 220-4.

63. Crofton, J. and D. Mitchison, *Streptomycin resistance in pulmonary tuberculosis.* British medical journal, 1948. **2**(4588): p. 1009.

64. Lehmann, J., *On the effect of isomers of PAS (para-aminosalicylic acid) and related substances on the tuberculostatic effect of PAS.* Experientia, 1949. **5**(9): p. 365-367.

65. Edlin, B.R., et al., *An outbreak of multidrug-resistant tuberculosis among hospitalized patients with the acquired immunodeficiency syndrome.* N Engl J Med, 1992. **326**(23): p. 1514-21.

66. Espinal, M.A., *The global situation of MDR-TB.* Tuberculosis, 2003. **83**(1-3): p. 44-51.

67. Cox, H.S., et al., *Multidrug-resistant tuberculosis treatment outcomes in Karakalpakstan, Uzbekistan: treatment complexity and XDR-TB among treatment failures.* PLoS One, 2007. **2**(11): p. e1126.

68. Dye, C. and B.G. Williams, *Criteria for the control of drug-resistant tuberculosis.* Proc Natl Acad Sci U S A, 2000. **97**(14): p. 8180-5.

69. Jassal, M. and W.R. Bishai, *Extensively drug-resistant tuberculosis.* The Lancet Infectious Diseases, 2009. **9**(1): p. 19-30.

70. Luca, S. and T. Mihaescu, *History of BCG Vaccine*. 2013, Amaltea Medical, Editura Magister.

71. Fine, P.E.M., *Variation in protection by BCG: implications of and for heterologous immunity.* The Lancet, 1995. **346**(8986): p. 1339-1345.

72. Brewer, T.F., *Preventing tuberculosis with bacillus Calmette-Guerin vaccine: a meta-analysis of the literature.* Clin Infect Dis, 2000. **31 Suppl 3**: p. S64-7.

73. Romanus, V., et al., *Atypical mycobacteria in extrapulmonary disease among children. Incidence in Sweden from 1969 to 1990, related to changing BCG-vaccination coverage.* Tubercle and Lung Disease, 1995. **76**(4): p. 300-310.

74. Trnka, L., D. Daňková, and E. Švandová, *Six years' experience with the discontinuation of BCG vaccination.* Tubercle and Lung Disease, 1994. **75**(5): p. 348-352.

75. Trunz, B.B., P.E.M. Fine, and C. Dye, *Effect of BCG vaccination on childhood tuberculous meningitis and miliary tuberculosis worldwide: a meta-analysis and assessment of cost-effectiveness.* The Lancet, 2006. **367**(9517): p. 1173-1180.

76. Hesseling, A.C., et al., *The risk of disseminated Bacille Calmette-Guerin (BCG) disease in HIV-infected children.* Vaccine, 2007. **25**(1): p. 14-8.

77. Nakajima, H., *Tuberculosis: a global emergency.* World Health, 1993. **46**(4): p. 3.

78. Ginsberg, A.M., et al., *TB vaccines in clinical development.* Tuberculosis (Edinb), 2016. **99 Suppl 1**: p. S16-20.

79. Ahsan, M.J., *Recent advances in the development of vaccines for tuberculosis.* Ther Adv Vaccines, 2015. **3**(3): p. 66-75.

80. Ottenhoff, T.H. and S.H. Kaufmann, *Vaccines against tuberculosis: where are we and where do we need to go?* PLoS Pathog, 2012. **8**(5): p. e1002607.

81. Karonga Prevention Trial Group, *Randomised controlled trial of single BCG, repeated BCG, or combined BCG and killed Mycobacterium leprae vaccine for prevention of leprosy and tuberculosis in Malawi. Karonga Prevention Trial Group.* Lancet, 1996. **348**(9019): p. 17-24.

82. Blanchard, T.J., et al., *Modified vaccinia virus Ankara undergoes limited replication in human cells and lacks several immunomodulatory proteins: implications for use as a human vaccine.* J Gen Virol, 1998. **79 (Pt 5)**: p. 1159-67.

83. D'Souza, S., et al., *Mapping of Murine Th1 Helper T-Cell Epitopes of Mycolyl Transferases Ag85A, Ag85B, and Ag85C from Mycobacterium tuberculosis.* Infection and Immunity, 2003. **71**(1): p. 483-493.

84. McShane, H., et al., *Enhanced immunogenicity of CD4(+) t-cell responses and protective efficacy of a DNA-modified vaccinia virus Ankara prime-boost vaccination regimen for murine tuberculosis.* Infect Immun, 2001. **69**(2): p. 681-6.

85. Ndiaye, B.P., et al., *Safety, immunogenicity, and efficacy of the candidate tuberculosis vaccine MVA85A in healthy adults infected with HIV-1: a randomised, placebo-controlled, phase 2 trial.* The Lancet Respiratory Medicine, 2015. **3**(3): p. 190-200.

86. Nemes, E., et al., *Safety and Immunogenicity of Newborn MVA85A Vaccination and Selective, Delayed Bacille Calmette-Guerin (BCG) for Infants of HIV Infected Mothers: A Phase 2 Randomized Controlled Trial.* Clin Infect Dis, 2017.

87. Smaill, F. and Z. Xing, *Human type 5 adenovirus-based tuberculosis vaccine: is the respiratory route of delivery the future?* Expert Rev Vaccines, 2014. **13**(8): p. 927-30.

88. Radosevic, K., et al., *Protective immune responses to a recombinant adenovirus type 35 tuberculosis vaccine in two mouse strains: CD4 and CD8 T-cell epitope mapping and role of gamma interferon.* Infect Immun, 2007. **75**(8): p. 4105-15.

89. Florido, M., et al., *Epitope-specific CD4+, but not CD8+, T-cell responses induced by recombinant influenza A viruses protect against Mycobacterium tuberculosis infection.* Eur J Immunol, 2015. **45**(3): p. 780-93.

90. Olafsdottir, T.A., et al., *IC31, a two-component novel adjuvant mixed with a conjugate vaccine enhances protective immunity against pneumococcal disease in neonatal mice.* Scand J Immunol, 2009. **69**(3): p. 194-202.

91. Luabeya, A.K., et al., *First-in-human trial of the post-exposure tuberculosis vaccine H56:IC31 in Mycobacterium tuberculosis infected and non-infected healthy adults.* Vaccine, 2015. **33**(33): p. 4130-40.

92. Scriba, T.J., et al., *Vaccination Against Tuberculosis With Whole-Cell Mycobacterial Vaccines.* J Infect Dis, 2016. **214**(5): p. 659-64.

93. Walker, K.B., et al., *The second Geneva Consensus: Recommendations for novel live TB vaccines.* Vaccine, 2010. **28**(11): p. 2259-70.

94. Nieuwenhuizen, N.E., et al., *The Recombinant Bacille Calmette-Guerin Vaccine VPM1002: Ready for Clinical Efficacy Testing.* Front Immunol, 2017. **8**: p. 1147.

95. Loxton, A.G., et al., *Safety and Immunogenicity of the Recombinant Mycobacterium bovis BCG Vaccine VPM1002 in HIV-Unexposed Newborn Infants in South Africa.* Clin Vaccine Immunol, 2017. **24**(2).

96. Aguilo, N., et al., *MTBVAC vaccine is safe, immunogenic and confers protective efficacy against Mycobacterium tuberculosis in newborn mice.* Tuberculosis (Edinb), 2016. **96**: p. 71-4.

97. Stucki, D., et al., *Mycobacterium tuberculosis lineage 4 comprises globally distributed and geographically restricted sublineages.* Nat Genet, 2016. **48**(12): p. 1535-1543.

98. Spertini, F., et al., *Safety of human immunisation with a live-attenuated Mycobacterium tuberculosis vaccine: a randomised, double-blind, controlled phase I trial.* The Lancet Respiratory Medicine, 2015. **3**(12): p. 953-962.

99. Nell, A.S., et al., *Safety, tolerability, and immunogenicity of the novel antituberculous vaccine RUTI: randomized, placebo-controlled phase II clinical trial in patients with latent tuberculosis infection.* PLoS One, 2014. **9**(2): p. e89612.

100. Yang, X.Y., et al., *Mycobacterium vaccae as adjuvant therapy to anti-tuberculosis chemotherapy in never-treated tuberculosis patients: a meta-analysis.* PLoS One, 2011. **6**(9): p. e23826.

101. Groschel, M.I., et al., *Therapeutic vaccines for tuberculosis--a systematic review.* Vaccine, 2014. **32**(26): p. 3162-8.

102. Koul, A., et al., *The challenge of new drug discovery for tuberculosis.* Nature, 2011. **469**(7331): p. 483-90.

103. Vilcheze, C. and W.R. Jacobs, Jr., *The mechanism of isoniazid killing: clarity through the scope of genetics.* Annu Rev Microbiol, 2007. **61**: p. 35-50.

104. Mitchison, D.A., *Role of individual drugs in the chemotherapy of tuberculosis.* The international journal of tuberculosis and lung disease, 2000. **4**(9): p. 796-806.

105. Winder, F.G. and P.B. Collins, *Inhibition by isoniazid of synthesis of mycolic acids in Mycobacterium tuberculosis.* J Gen Microbiol, 1970. **63**(1): p. 41-8.

106. Dessen, A., et al., *Crystal structure and function of the isoniazid target of Mycobacterium tuberculosis.* Science, 1995. **267**(5204): p. 1638-1641.

107. Banerjee, A., et al., *inhA, a gene encoding a target for isoniazid and ethionamide in Mycobacterium tuberculosis.* Science, 1994. **263**(5144): p. 227-230.

108. Johnsson, K. and P.G. Schultz, *Mechanistic Studies of the Oxidation of Isoniazid by the Catalase Peroxidase from Mycobacterium tuberculosis.* Journal of the American Chemical Society, 1994. **116**(16): p. 7425-7426.

109. Timmins, G.S. and V. Deretic, *Mechanisms of action of isoniazid.* Mol Microbiol, 2006. **62**(5): p. 1220-7.

110. Goldman, A.L. and S.S. Braman, *Isoniazid: A Review with Emphasis on Adverse Effects.* Chest, 1972. **62**(1): p. 71-77.

111. LoBue, P.A. and K.S. Moser, *Use of isoniazid for latent tuberculosis infection in a public health clinic.* Am J Respir Crit Care Med, 2003. **168**(4): p. 443-7.

112. Thomas, J.P., et al., *A new synthetic compound with antituberculous activity in mice: ethambutol (dextro-2,2'-(ethylenediimino)-di-l-butanol).* Am Rev Respir Dis, 1961. **83**: p. 891-3.

113. Belanger, A.E., et al., *The embAB genes of Mycobacterium avium encode an arabinosyl transferase involved in cell wall arabinan biosynthesis that is the target for the antimycobacterial drug ethambutol.* Proceedings of the National Academy of Sciences, 1996. **93**(21): p. 11919-11924.

114. Tsai, R.K. and Y.H. Lee, *Reversibility of ethambutol optic neuropathy.* J Ocul Pharmacol Ther, 1997. **13**(5): p. 473-7.

115. Kahana, L.M., *Toxic ocular effects of ethambutol.* Cmaj, 1987. **137**(3): p. 213-6.

116. Sensi, P., *History of the Development of Rifampin.* Clinical Infectious Diseases, 1983. **5**(Supplement_3): p. S402-S406.

117. Floss, H.G. and T.W. Yu, *Rifamycin-mode of action, resistance, and biosynthesis.* Chem Rev, 2005. **105**(2): p. 621-32.

118. Telenti, A., et al., *Detection of rifampicin-resistance mutations in Mycobacterium tuberculosis.* Lancet, 1993. **341**(8846): p. 647-50.

119. Grosset, J. and S. Leventis, *Adverse Effects of Rifampin.* Reviews of Infectious Diseases, 1983. **5**(Supplement_3): p. S440-S446.

120. Cole, S.T., *Microbiology. Pyrazinamide--old TB drug finds new target.* Science, 2011. **333**(6049): p. 1583-4.

121. Hirano, K., et al., *Mutation in pncA is a major mechanism of pyrazinamide resistance in Mycobacterium tuberculosis.* Tubercle and Lung Disease, 1998. **78**(2): p. 117-122.

122. Shi, W., et al., *Pyrazinamide inhibits trans-translation in Mycobacterium tuberculosis.* Science, 2011. **333**(6049): p. 1630-2.

123. Zhang, Y., et al., *Mode of action of pyrazinamide: disruption of Mycobacterium tuberculosis membrane transport and energetics by pyrazinoic acid.* J Antimicrob Chemother, 2003. **52**(5): p. 790-5.

124. Gopal, P., et al., *Pyrazinamide Resistance Is Caused by Two Distinct Mechanisms: Prevention of Coenzyme A Depletion and Loss of Virulence Factor Synthesis.* ACS Infect Dis, 2016. **2**(9): p. 616-626.

125. Gopal, P., et al., *Pyrazinoic Acid Inhibits Mycobacterial Coenzyme A Biosynthesis by Binding to Aspartate Decarboxylase PanD.* ACS Infect Dis, 2017. **3**(11): p. 807-819.

126. Yee, M., P. Gopal, and T. Dick, *Missense Mutations in the Unfoldase ClpC1 of the Caseinolytic Protease Complex Are Associated with Pyrazinamide Resistance in Mycobacterium tuberculosis.* Antimicrob Agents Chemother, 2017. **61**(2).

127. Schaberg, T., K. Rebhan, and H. Lode, *Risk factors for side-effects of isoniazid, rifampin and pyrazinamide in patients hospitalized for pulmonary tuberculosis.* European Respiratory Journal, 1996. **9**(10): p. 2026-2030.

128. Control, C.f.D. and Prevention, *Fatal and severe hepatitis associated with rifampin and pyrazinamide for the treatment of latent tuberculosis infection--New York and Georgia, 2000.* MMWR. Morbidity and mortality weekly report, 2001. **50**(15): p. 289.

129. Matsumoto, M., et al., *OPC-67683, a nitro-dihydro-imidazooxazole derivative with promising action against tuberculosis in vitro and in mice.* PLoS Med, 2006. **3**(11): p. e466.

130. Gler, M.T., et al., *Delamanid for multidrug-resistant pulmonary tuberculosis.* N Engl J Med, 2012. **366**(23): p. 2151-60.

131. Stover, C.K., et al., *A small-molecule nitroimidazopyran drug candidate for the treatment of tuberculosis.* Nature, 2000. **405**(6789): p. 962-6.

132. Manjunatha, U., H.I.M. Boshoff, and C.E. Barry, *The mechanism of action of PA-824: Novel insights from transcriptional profiling.* Commun Integr Biol, 2009. **2**(3): p. 215-8.

133. Singh, R., et al., *PA-824 kills nonreplicating Mycobacterium tuberculosis by intracellular NO release.* Science, 2008. **322**(5906): p. 1392-5.

134. Tasneen, R., et al., *Sterilizing activity of novel TMC207- and PA-824-containing regimens in a murine model of tuberculosis.* Antimicrob Agents Chemother, 2011. **55**(12): p. 5485-92.

135. Diacon, A.H., et al., *Bactericidal activity of pyrazinamide and clofazimine alone and in combinations with pretomanid and bedaquiline.* Am J Respir Crit Care Med, 2015. **191**(8): p. 943-53.

136. Diacon, A.H., et al., *Phase II dose-ranging trial of the early bactericidal activity of PA-824.* Antimicrob Agents Chemother, 2012. **56**(6): p. 3027-31.

137. Dawson, R., et al., *Efficiency and safety of the combination of moxifloxacin, pretomanid (PA-824), and pyrazinamide during the first 8 weeks of antituberculosis treatment: a phase 2b, open-label, partly randomised trial in patients with drug-susceptible or drug-resistant pulmonary tuberculosis.* The Lancet, 2015. **385**(9979): p. 1738-1747.

138. Boshoff, H.I. and C.E. Barry, 3rd, *Tuberculosis - metabolism and respiration in the absence of growth.* Nat Rev Microbiol, 2005. **3**(1): p. 70-80.

139. Voskuil, M.I., et al., *Inhibition of respiration by nitric oxide induces a Mycobacterium tuberculosis dormancy program.* J Exp Med, 2003. **198**(5): p. 705-13.

140. Boshoff, H.I., et al., *The transcriptional responses of Mycobacterium tuberculosis to inhibitors of metabolism: novel insights into drug mechanisms of action.* J Biol Chem, 2004. **279**(38): p. 40174-84.

141. The, J. S. ,et al., *Type II NADH:Menaquinone Oxidoreductase of Mycobacterium tuberculosis.* Infectious Disorders - Drug Targets, 2007. **7**(2): p. 169-181.

142. Yano, T., et al., *Mycobacterium tuberculosis type II NADH-menaquinone oxidoreductase catalyzes electron transfer through a two-site ping-pong mechanism and has two quinone-binding sites.* Biochemistry, 2014. **53**(7): p. 1179-90.

143. Weinstein, E.A., et al., *Inhibitors of type II NADH:menaquinone oxidoreductase represent a class of antitubercular drugs.* Proceedings of the National Academy of Sciences, 2005. **102**(12): p. 4548-4553.

144. Kang, S., et al., *Lead optimization of a novel series of imidazo[1,2-a]pyridine amides leading to a clinical candidate (Q203) as a multi- and extensively-drug-resistant anti-tuberculosis agent.* J Med Chem, 2014. **57**(12): p. 5293-305.

145. Pethe, K., et al., *Discovery of Q203, a potent clinical candidate for the treatment of tuberculosis.* Nat Med, 2013. **19**(9): p. 1157-60.

146. Tran, S.L. and G.M. Cook, *The F1Fo-ATP synthase of Mycobacterium smegmatis is essential for growth.* J Bacteriol, 2005. **187**(14): p. 5023-8.

147. Biukovic, G., et al., *Variations of subunit {varepsilon} of the Mycobacterium tuberculosis F1Fo ATP synthase and a novel model for mechanism of action of the tuberculosis drug TMC207.* Antimicrob Agents Chemother, 2013. **57**(1): p. 168-76.

148. Lu, P., H. Lill, and D. Bald, *ATP synthase in mycobacteria: special features and implications for a function as drug target.* Biochim Biophys Acta, 2014. **1837**(7): p. 1208-18.

149. Priya, R., et al., *Solution structure of subunit gamma (gamma(1-204)) of the Mycobacterium tuberculosis F-ATP synthase and the unique loop of gamma(165-178), representing a novel TB drug target.* J Bioenerg Biomembr, 2013. **45**(1-2): p. 121-9.

150. Matteelli, A., et al., *TMC207: the first compound of a new class of potent anti-tuberculosis drugs.* Future Microbiol, 2010. **5**(6): p. 849-58.

151. Koul, A., et al., *Diarylquinolines target subunit c of mycobacterial ATP synthase.* Nat Chem Biol, 2007. **3**(6): p. 323-4.

152. Fox, G.J. and D. Menzies, *A Review of the Evidence for Using Bedaquiline (TMC207) to Treat Multi-Drug Resistant Tuberculosis.* Infect Dis Ther, 2013. **2**(2): p. 123-44.

153. de Jonge, M.R., et al., *A computational model of the inhibition of Mycobacterium tuberculosis ATPase by a new drug candidate R207910.* Proteins, 2007. **67**(4): p. 971-80.

154. Dautant, A., J. Velours, and M.F. Giraud, *Crystal structure of the Mg.ADP-inhibited state of the yeast F1c10-ATP synthase.* J Biol Chem, 2010. **285**(38): p. 29502-10.

155. Robinson, G.C., et al., *The structure of F(1)-ATPase from Saccharomyces cerevisiae inhibited by its regulatory protein IF(1).* Open Biol, 2013. **3**(2): p. 120164.

156. Gledhill, J.R., et al., *How the regulatory protein, IF(1), inhibits F(1)-ATPase from bovine mitochondria.* Proc Natl Acad Sci U S A, 2007. **104**(40): p. 15671-6.

157. Cingolani, G. and T.M. Duncan, *Structure of the ATP synthase catalytic complex (F(1)) from Escherichia coli in an autoinhibited conformation.* Nat Struct Mol Biol, 2011. **18**(6): p. 701-7.

158. Laskowski, R.A., et al., *PROCHECK: a program to check the stereochemical quality of protein structures.* Journal of Applied Crystallography, 1993. **26**(2): p. 283-291.

159. Irwin, J.J., et al., *ZINC: a free tool to discover chemistry for biology.* J Chem Inf Model, 2012. **52**(7): p. 1757-68.

160. Lipinski, C.A., et al., *Experimental and computational approaches to estimate solubility and permeability in drug discovery and development settings1PII of original article: S0169-409X(96)00423-1. The article was originally published in Advanced Drug Delivery Reviews 23 (1997) 3–25.1.* Advanced Drug Delivery Reviews, 2001. **46**(1-3): p. 3-26.

161. Veber, D.F., et al., *Molecular Properties That Influence the Oral Bioavailability of Drug Candidates.* Journal of Medicinal Chemistry, 2002. **45**(12): p. 2615-2623.

162. Harikishore, A., et al., *Small molecule Plasmodium FKBP35 inhibitor as a potential antimalaria agent.* Sci Rep, 2013. **3**: p. 2501.

163. Kaserer, T., et al., *Pharmacophore Models and Pharmacophore-Based Virtual Screening: Concepts and Applications Exemplified on Hydroxysteroid Dehydrogenases.* Molecules, 2015. **20**(12): p. 22799-832.

164. Yang, S.Y., *Pharmacophore modeling and applications in drug discovery: challenges and recent advances.* Drug Discov Today, 2010. **15**(11-12): p. 444-50.

165. Voet, A., et al., *Pharmacophore modeling: advances, limitations, and current utility in drug discovery.* Journal of Receptor, Ligand and Channel Research, 2014.

166. Friesner, R.A., et al., *Extra precision glide: docking and scoring incorporating a model of hydrophobic enclosure for protein-ligand complexes.* J Med Chem, 2006. **49**(21): p. 6177-96.

167. Hotra, A., et al., *Deletion of a unique loop in the mycobacterial F-ATP synthase gamma subunit sheds light on its inhibitory role in ATP hydrolysis-driven H(+) pumping.* FEBS J, 2016. **283**(10): p. 1947-61.

168. *CellTiter-Glo® Luminescent Cell Viability Assay Technical Bulletin.*

169. Sherrard, L.J., M.M. Tunney, and J.S. Elborn, *Antimicrobial resistance in the respiratory microbiota of people with cystic fibrosis.* The Lancet, 2014. **384**(9944): p. 703-713.

170. Andries, K., et al., *A diarylquinoline drug active on the ATP synthase of Mycobacterium tuberculosis.* Science, 2005. **307**(5707): p. 223-7.

171. Drlica, K. and X. Zhao, *Mutant selection window hypothesis updated.* Clin Infect Dis, 2007. **44**(5): p. 681-8.

172. Koul, A., et al., *Diarylquinolines are bactericidal for dormant mycobacteria as a result of disturbed ATP homeostasis.* J Biol Chem, 2008. **283**(37): p. 25273-80.

173. Haagsma, A.C., et al., *ATP synthase in slow- and fast-growing mycobacteria is active in ATP synthesis and blocked in ATP hydrolysis direction.* FEMS Microbiol Lett, 2010. **313**(1): p. 68-74.

174. Rao, S.P., et al., *The protonmotive force is required for maintaining ATP homeostasis and viability of hypoxic, nonreplicating Mycobacterium tuberculosis.* Proc Natl Acad Sci U S A, 2008. **105**(33): p. 11945-50.

175. Vilcheze, C., et al., *Altered NADH/NAD+ ratio mediates coresistance to isoniazid and ethionamide in mycobacteria.* Antimicrob Agents Chemother, 2005. **49**(2): p. 708-20.

176. Gledhill, J.R., et al., *Mechanism of inhibition of bovine F1-ATPase by resveratrol and related polyphenols.* Proc Natl Acad Sci U S A, 2007. **104**(34): p. 13632-7.

177. Gledhill, J.R. and J.E. Walker, *Inhibition sites in F1-ATPase from bovine heart mitochondria.* Biochem J, 2005. **386**(Pt 3): p. 591-8.

178. Preiss, L., et al., *Structure of the mycobacterial ATP synthase Fo rotor ring in complex with the anti-TB drug bedaquiline.* Sci Adv, 2015. **1**(4): p. e1500106.

179. Hards, K., et al., *Bactericidal mode of action of bedaquiline.* J Antimicrob Chemother, 2015. **70**(7): p. 2028-37.

180. Haughton, M.A. and R.A. Capaldi, *Asymmetry ofEscherichia coliF1-ATPase as a Function of the Interaction of α-β Subunit Pairs with the γ and ϵ Subunits.* Journal of Biological Chemistry, 1995. **270**(35): p. 20568-20574.

181. Sebald, W., W. Machleidt, and E. Wachter, *N,N'-dicyclohexylcarbodiimide binds specifically to a single glutamyl residue of the proteolipid subunit of the mitochondrial adenosinetriphosphatases from Neurospora crassa and Saccharomyces cerevisiae.* Proc Natl Acad Sci U S A, 1980. **77**(2): p. 785-9.

182. Orriss, G.L., et al., *Bovine F1-ATPase covalently inhibited with 4-chloro-7-nitrobenzofurazan: the structure provides further support for a rotary catalytic mechanism.* Structure, 1998. **6**(7): p. 831-837.

183. Abrahams, J.P., et al., *The structure of bovine F1-ATPase complexed with the peptide antibiotic efrapeptin.* Proceedings of the National Academy of Sciences, 1996. **93**(18): p. 9420-9424.

184. Stover, C.K., et al., *New use of BCG for recombinant vaccines.* Nature, 1991. **351**(6326): p. 456-60.

185. Zharova, T.V. and A.D. Vinogradov, *ATPase/synthase activity of Paracoccus denitrificans Fo.F1 as related to the respiratory control phenomenon.* Biochim Biophys Acta, 2014. **1837**(8): p. 1322-9.

186. Klingenberg, M., *Reversibility of Energy Transformations in the Respiratory Chain.* Angewandte Chemie International Edition in English, 1964. **3**(1): p. 54-61.

187. LaNoue, K.F., F.M.H. Jeffries, and G.K. Radda, *Kinetic control of mitochondrial ATP synthesis.* Biochemistry, 2002. **25**(23): p. 7667-7675.

188. Boger, D.L. and H. Zarrinmayeh, *Regiocontrolled nucleophilic addition to selectively activated p-quinone diimines: alternative preparation of a key intermediate employed in the preparation of the CC-1065 left-hand subunit.* The Journal of Organic Chemistry, 1990. **55**(4): p. 1379-1390.

189. Tran, A.T., et al., *Inhibition studies on Mycobacterium tuberculosis N-acetylglucosamine-1-phosphate uridyltransferase (GlmU).* Org Biomol Chem, 2013. **11**(46): p. 8113-26.

190. Richey, R.N. and H. Yu, *Development of an Efficient Palladium-Catalyzed Intramolecular Carbometalation Reaction for the Synthesis of a Dibenzoxapine Containing Tetra-substituted Exocyclic Alkene†.* Organic Process Research & Development, 2009. **13**(2): p. 315-320.

191. Tasler, S., et al., *N-substituted 2'-(aminoaryl)benzothiazoles as kinase inhibitors: hit identification and scaffold hopping.* Bioorg Med Chem Lett, 2009. **19**(5): p. 1349-56.

192. Odell, L.R., et al., *Pyrimidine-Based Inhibitors of Dynamin I GTPase Activity: Competitive Inhibition at the Pleckstrin Homology Domain.* J Med Chem, 2017. **60**(1): p. 349-361.

193. McCluskey, A., et al., *Synthesis, molecular modeling and biological activity of methyl and thiomethyl substituted pyrimidines as corticotropin releasing hormone type 1 antagonistsElectronic supplementary information (ESI) available: detailed description of pharmacophore development using CATALYST.*. Organic & Biomolecular Chemistry, 2003. **1**(19): p. 3353.

194. Butts, C.P., et al., *Interproton distance determinations by NOE--surprising accuracy and precision in a rigid organic molecule.* Org Biomol Chem, 2011. **9**(1): p. 177-84.

195. Gershon, H., et al., *Pyrimidines.8. chlorination of 6-methyluracil with phosphorus oxychloride in the presence of trialkyamines.* Journal of Heterocyclic Chemistry, 1987. **24**(1): p. 205-209.

196. Thalji, R.K., et al., *Discovery of 1-(1,3,5-triazin-2-yl)piperidine-4-carboxamides as inhibitors of soluble epoxide hydrolase.* Bioorg Med Chem Lett, 2013. **23**(12): p. 3584-8.

197. Savjani, K.T., A.K. Gajjar, and J.K. Savjani, *Drug solubility: importance and enhancement techniques.* ISRN Pharm, 2012. **2012**: p. 195727.

198. Saal, C. and A.C. Petereit, *Optimizing solubility: kinetic versus thermodynamic solubility temptations and risks.* Eur J Pharm Sci, 2012. **47**(3): p. 589-95.

199. Shoichet, B.K., *Interpreting steep dose-response curves in early inhibitor discovery.* J Med Chem, 2006. **49**(25): p. 7274-7.

200. Ragunathan, P., et al., *The uniqueness of subunit alpha of mycobacterial F-ATP synthases: An evolutionary variant for niche adaptation.* J Biol Chem, 2017. **292**(27): p. 11262-11279.

201. Kundu, S., et al., *Bedaquiline Targets the epsilon Subunit of Mycobacterial F-ATP Synthase.* Antimicrob Agents Chemother, 2016. **60**(11): p. 6977-6979.

Author's publications related to the PhD project:

Hotra, A., et al., *Deletion of a unique loop in the mycobacterial F-ATP synthase gamma subunit sheds light on its inhibitory role in ATP hydrolysis-driven H(+) pumping.* FEBS J, 2016. **283**(10): p. 1947-61.

Poster presentations and conference attendance:

Tuberculosis Drug Discovery and Development, Gordon Conference,
Lucca, Italy, Jun 2017

2nd Symposium on Medicinal Chemistry for Global Health,
Madrid, Spain, Jun 2017

International Conference on Organic Synthesis (ICOS21)
Bombay, India, Dec 2016

Pure and Applied Chemistry International Conference 2016
Bangkok, Thailand, Feb 2016